AIP Advances

Near-field radiative thermal transport: From theory to experiment

Cite as: AIP Advances **5**, 053503 (2015); https://doi.org/10.1063/1.4919048
Submitted: 10 February 2015 • Accepted: 31 March 2015 • Published Online: 21 April 2015

Bai Song, Anthony Fiorino, Edgar Meyhofer, et al.

ARTICLES YOU MAY BE INTERESTED IN

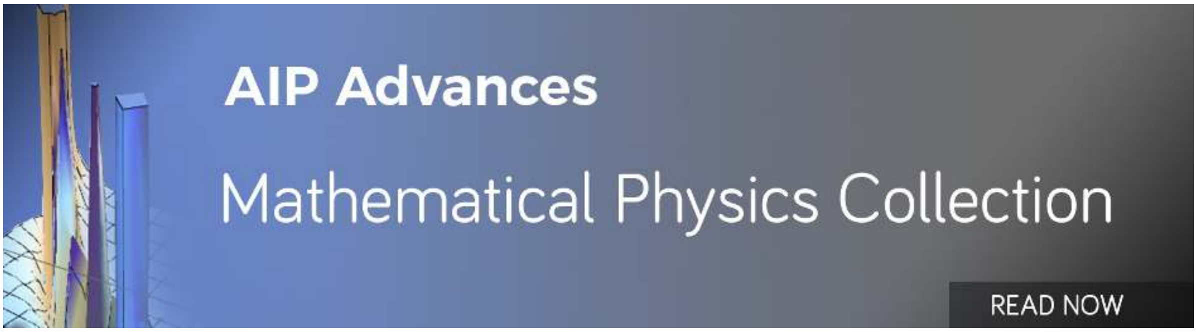

AIP Advances **5**, 053503 (2015); https://doi.org/10.1063/1.4919048 **5**, 053503

AIP ADVANCES **5**, 053503 (2015)

Near-field radiative thermal transport: From theory to experiment

Bai Song,[1,a] Anthony Fiorino,[1] Edgar Meyhofer,[1,b] and Pramod Reddy[1,2,c]
[1]*Department of Mechanical Engineering, University of Michigan, Ann Arbor, Michigan 48109, USA*
[2]*Department of Materials Science and Engineering, University of Michigan, Ann Arbor, Michigan 48109, USA*

(Received 10 February 2015; accepted 31 March 2015; published online 21 April 2015)

Radiative thermal transport via the fluctuating electromagnetic near-field has recently attracted increasing attention due to its fundamental importance and its impact on a range of applications from data storage to thermal management and energy conversion. After a brief historical account of radiative thermal transport, we summarize the basics of fluctuational electrodynamics, a theoretical framework for the study of radiative heat transfer in terms of thermally excited propagating and evanescent electromagnetic waves. Various approaches to modeling near-field thermal transport are briefly discussed, together with key results and proposals for manipulation and utilization of radiative heat flow. Subsequently, we review the experimental advances in the characterization of both near-field heat flow and energy density. We conclude with remarks on the opportunities and challenges for future explorations of radiative heat transfer at the nanoscale. [http://dx.doi.org/10.1063/1.4919048]

I. INTRODUCTION

Thermal radiation is universal to all objects at non-zero absolute temperatures as electromagnetic radiative emissions necessarily accompany thermally driven random motions of electric charges. Historically, rudimentary yet at times intensive inquiries into the nature of radiant heat transfer between macroscopic bodies and its governing laws spanned hundreds of years.[1] These efforts were greatly boosted by William Hershel's discovery of the infrared in 1800[2–4] and ultimately culminated in Max Planck's law of blackbody radiation at the turn of the 20th century.[5–7] Quantum physics largely originated from the efforts of Planck and his contemporaries to better understand experimental results on blackbody radiation,[8–10] and in return helped in the establishment of a more general and advanced theory of thermal radiation. The quantum mechanical derivation of various fluctuation-dissipation theorems (FDT),[11–14] and more importantly the formulation of Sergei M. Rytov's fluctuational electrodynamics around the early 1950s,[15,16] allowed for the first time direct and detailed mathematical descriptions that related thermal radiation to its origin in the random fluctuations of charges, which represented a significant step beyond discussions of equilibrium distribution of radiation from unspecified sources.

Further, the need for better insulation at cryogenic temperatures[17] and the rapid development of technologies at the micrometer scale created an emerging need to understand thermal radiation in systems with length scales comparable to or smaller than the peak radiation wavelength. In this regime, two effects become important:[18–27] First, the interference of electromagnetic waves causes discernible differences in radiative heat transfer. Second, the evanescent contributions to heat transfer become dominant (Fig. 1(a), 1(b)). The near-field outside an object is a natural

---

[a] Electronic mail: baisong@umich.edu
[b] Electronic mail: meyhofer@umich.edu
[c] Author to whom correspondence should be addressed. Electronic mail: pramodr@umich.edu

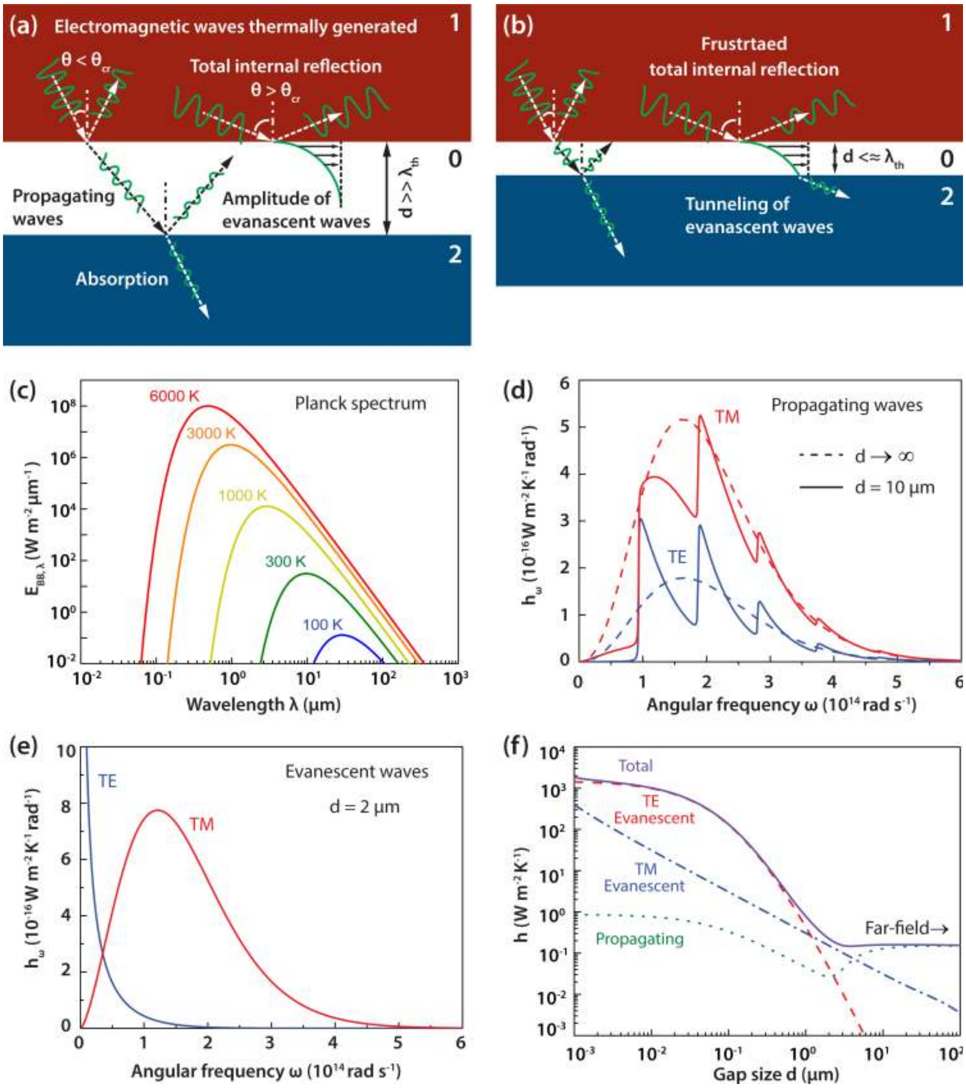

FIG. 1. Fundamentals of thermal radiation and radiative heat transfer in the far- and near-field. (a) Schematic for far-field radiation between two parallel semi-infinite bodies denoted as "1" and "2", separated by a large vacuum gap denoted by "0". (b) Radiative heat transfer across a vacuum gap comparable to or smaller than the peak thermal wavelength. (c) Blackbody spectral emissive power given by Planck's law. (d) Spectral heat transfer coefficient due to propagating waves calculated for two Cr semi-bodies. (e) Spectral heat transfer coefficient due to evanescent waves. (f) Heat transfer coefficients showing contributions by different modes and polarizations. (d)-(f) are our calculation results using the same Cr dielectric function and other relevant parameters as found in Polder and van Hove.[90]

extension of the electromagnetic field inside, as demanded by the continuity of field amplitudes across an interface.[28] For evanescent waves, the amplitude of the fields decays exponentially with increasing distance from the interface, however, when the spatial separation between surfaces is small (i.e. they are in the near-field of each other) there is a dramatic increase in energy density and flow due to evanescent contributions.[18–27] The description of near-field radiation requires ideas and concepts that go beyond those required for far-field radiation. In terms of applications, near-field radiative heat transfer (NFRHT) is expected to be key to developing novel technologies such as thermal lithography,[18] coherent thermal sources,[29–36] scanning thermal microscopy,[37–39] heat-assisted magnetic recording, [40–42] advanced thermal management and thermal logic devices,[43–65] as well as thermophotovoltaic[66–78] and other[79–82] energy conversion devices.

In this article we begin by providing some historical context (Sec. II). In Sec. III, we briefly summarize the basics of the analytical framework necessary for quantifying NFRHT and describe recent work in theoretical and numerical investigations of NFRHT. In Sec. IV we describe the experimental efforts in probing NFRHT and provide a detailed discussion of various experimental configurations and approaches, including measurements of NFRHT between two parallel plane surfaces, between a scanning probe tip and a plane surface, as well as between a sphere and a plane. Further, we also describe thermal near-field spectroscopy techniques, which give important insights into the local energy density. We conclude in Sec. V with a brief discussion of the opportunities and challenges in future exploration of radiative heat transfer.

II. A BRIEF HISTORY OF RADIATIVE HEAT TRANSFER

A. Planck's law of blackbody radiation

Planck's law of blackbody thermal radiation describes the spectral energy density of electromagnetic radiation $u_{BB,\lambda}(T)$ in a cavity in thermal equilibrium and was first presented by Planck[5] at the German Physical Society meeting in October 1900 as

$$u_{BB,\lambda}(T) = \frac{C_1 \lambda^{-5}}{e^{\frac{C_2}{\lambda T}} - 1}, \tag{1}$$

where λ is the free space wavelength, T is the absolute temperature, while C_1 and C_2 denote empirical fitting constants. A large enclosed opaque cavity that features a tiny hole is an excellent practical realization of an all-absorbing blackbody, as light entering the hole is either reflected indefinitely or absorbed in the cavity and is unlikely to re-emerge. Consequently, discussions of blackbody radiation frequently refer to the idea of a cavity. Planck derived the relation given in Eq. (1) using his deterministic concept of oscillator entropy, but also considered it "eine glücklich erratene Interpolationsformel", that is, a lucky guessed interpolation. It seamlessly bridges Wien's formula effective at short wavelengths and that of Lord Rayleigh valid only at long wavelengths, and is in excellent agreement with experimental data across the spectrum. Soon afterwards, as a determined effort to go beyond his inspired first guess and reveal more fundamental physics, Planck reluctantly turned to Boltzmann's probabilistic picture of entropy.[10] Only about two months later, in December 1900 and again to the German Physical Society, Planck[6] presented his new derivation and expression:

$$u_{BB,\nu}(T) = \frac{8\pi h_P \nu^3}{c^3} \frac{1}{e^{\frac{h_P \nu}{k_B T}} - 1}, \tag{2}$$

where ν is the frequency, and the empirical fitting constants have been superseded by what are now known as three of the most important fundamental physical constants, i.e., the free space speed of light c, the Boltzmann constant k_B and most importantly the constant h_P, which was explicitly introduced for the first time by Planck, with a proposed value of "6.55×10^{-27} erg · sec". Despite the many and more advanced derivations and interpretations that came about thereafter, Planck's law in the form of Eq. (2) has since withstood the test of time. And more profoundly, this seminal work has been widely credited as having initiated the quantum era.[8–10]

Planck's law is of fundamental importance to the study of radiative heat transport between many bodies in addition to thermal radiation from isolated objects. It depicts a broadband emission spectrum, which implies temporal incoherence. Also, the spatial coherence of thermal radiation has traditionally been considered poor due to its origin in the random currents distributed throughout the volume of an object. Variations of Eq. (2) that express the spectral energy density in terms of wavelength λ or wavenumber η are also used. Apart from the energy density, the closely-related spectral emissive power has been frequently discussed. With respect to the wavelength, the hemispherical spectral emissive power (energy emitted into a half-space per unit time per unit area per unit wavelength at a given wavelength) of a blackbody $E_{BB,\lambda}$ is related to the spectral energy density via $E_{BB,\lambda} = c u_{BB,\lambda}/4$,[9,83] where $u_{BB,\lambda}$ is the wavelength representation of Eq. (2). As illustrated in Fig. 1(c), the Planck spectrum features a maximum spectral emissive power at a temperature-dependent wavelength. One can derive from $E_{BB,\lambda}$ that for any given temperature T, the peak wavelength is given by $\lambda_{BB,\max} \approx 2900/T$ (μm). This relationship is historically called the Wien's displacement law[83] and at room temperature (∼300 K), the peak wavelength is about 10 μm. Further, Planck's law naturally leads to the Stefan-Boltzmann law[83] which states that the total emissive power of a blackbody E_{BB} is proportional to T^4, with a proportionality constant σ given by $\sigma = 2\pi^5 k_B^4/15c^2h^3 \approx 5.67 \times 10^{-8}\,\mathrm{Wm^{-2}K^{-4}}$. In deriving this equation one simply integrate $E_{BB,\lambda}$ over all wavelengths and show that the total emissive power of a blackbody is indeed $E_{BB} = \sigma T^4$. For a real object the spectral emissive power is usually written as $E_\lambda = e_\lambda E_{BB,\lambda}$ where e_λ is its emissivity at a wavelength of λ and $e_\lambda \in [0,1]$. Consequently, the Stefan-Boltzmann law was considered to represent the maximum emissive power (frequently referred to as the blackbody limit) that is possible for any object, at temperature T. Also, note that only the object's temperature and material properties are involved, and no dependence on any spatial separation is present. As outlined above the Wien's displacement law and Stefan-Boltzmann law are direct consequences of Planck's law, and together they provide the foundation for far-field radiative heat transfer theories.[83,84]

Nevertheless, Planck's law is not without limitations. As pointed out by Planck himself in his book on the Theory of Heat Radiation,[7] the spectrum as given by Eq. (2) and consequently the Wien's displacement law and Stefan-Boltzmann law, are only valid when all relevant spatial length scales are much larger than the peak wavelengths. The effect of this underlying assumption on thermal radiation seems to have been noted first by Bijl[85] in the context of small cavities at cryogenic temperatures. Specifically, it was highlighted that at very low temperatures, where the characteristic wavelength of thermal radiation becomes comparable to the size of the cavity, classical far-field radiative heat transfer theories would fail to adequately describe heat transfer via radiation. The failure of radiative heat transfer theories at smaller length scales attracted very little attention for many decades, possibly due to lack of theoretical and technical relevance. Indeed, this situation remained true for a good portion of the 20th century, until around the 1950s.

B. Radiation between closely spaced bodies

One may speculate that the desire and necessity to go beyond Planck's law and to inquire into various size effects in thermal radiation became increasingly tangible on two fronts. Theoretically, progress in the study of proximity forces, especially the closely related Casimir effect (1948),[86] could have inspired similar research on thermal radiation. More importantly, the general framework of fluctuational electrodynamics capable of consistently describing both Casimir effect and thermal radiation was proposed by Rytov[15,16] in 1953, combining Maxwell's equations with the fluctuation-dissipation theorem governing electromagnetic fields. In fact, Rytov even solved an example problem of radiative heat transfer between two closely-spaced parallel plane surfaces, with one being an arbitrary dissipative medium and the other being a mirror of good electrical conductivity. He suggested that the "energy flow density into the mirror" could increase "without limit" as the spatial separation between the two planes vanishes, due to contribution from the "quasi-stationary field, localized in the layer close to the radiating surface".[15] This result represents a dramatic deviation from the constant heat flow independent of the separation as predicted by Planck's (Stefan-Boltzmann) law. However, to the authors' knowledge, no sequel to this remarkable episode was to be found until the beginning of the 1960s, when the practical need for managing radiative thermal transport across distances comparable to or smaller than the characteristic wavelength appeared.

In 1961, at the AFOSR/ADL Conference on Aerodynamically Heated Structures, A. G. Emslie[17] presented his analysis of radiative heat transfer in the multifoil radiation shields for thermal protection of cryogenic fuels in space. He estimated that at a temperature of 20 K the peak of the Planck radiation distribution corresponds to a wavelength of $\lambda_{BB,\max} = 0.15$ mm, which is of the same order of magnitude as the separation of the foils. The radiation transfer rate between metal foils with constant complex refraction index was predicted to increase with decreasing separation and attains a maximum of over 10 times the large-distance value at a separation of $0.2\lambda_{BB,\max}$ due to constructive interference of propagating waves. For even smaller gaps, however, the heat transfer rate was predicted to reduce to smaller values. Being aware of the evanescent waves, Emslie also noted that "radiation tunneling" could contribute to heat transfer across small gaps, causing further deterioration of the insulation performance of the shields. However, he did not quantitatively estimate the effect of such contribution as he felt that "an exact quantitative analysis of the magnitude of the energy transfer between two metals by the tunneling process is quite difficult to carry out".

A few years later investigations on radiative thermal transport across small gaps started gaining real momentum, with significant progress made in both theory and experiment. In 1967, Cravalho, Tien and Caren,[87] citing Emslie,[17] considered wave interference and radiation tunneling between two plane dielectrics of constant real refractive index at cryogenic temperatures. They were able to treat both effects in a unified approach and predicted an increase in heat flow with decreasing gap size as high as an order of magnitude. However, the assumption of lossless and non-dispersive dielectrics renders the work marginally relevant. It should be noted that a similar paper was published by Olivei in 1968, in which the concept of critical angle played a key role.[88] Later in 1970, Boehm and Tien[89] discussed the case of two metals separated by a transparent dielectrics with constant real refractive index, showing that the radiative heat transfer across small gaps is enhanced by many orders of magnitude, at cryogenic temperatures as well as room temperature. In order to account for nonlocal effects in metals, their use of the anomalous skin effect theory for prediction of the optical properties is noteworthy. Despite yielding many qualitatively sound conclusions, their approach was considered unsatisfactory.

It was not until January 1971 when Polder and Van Hove presented their widely recognized theory of radiative heat transfer between closely spaced bodies.[90] The approach was based on Rytov's fluctuational electrodynamics, but instead of using fluctuating electromagnetic fields in Maxwell's equations as the source terms, they considered the thermally driven fluctuating currents. As a result, the solution was simplified.[90] They focused specifically on the case of two parallel semi-infinite bodies separated by a vacuum gap, where the two bodies are identical with isotropic, nonmagnetic but otherwise arbitrarily dispersive and absorptive properties (Fig. 1(b)). Specifically, radiative heat transfer between two chromium (Cr) half spaces was studied. Contributions to heat transfer across the vacuum gap from both the propagating and evanescent electromagnetic waves, as well as both the transverse electric (TE, or s-mode) and transverse magnetic (TM, or p-mode) polarizations were consistently considered, with each individual combination (say propagating TE or TM modes) naturally separated from the others (Figs. 1(d)-1(f)). A comparison of the spectrum of radiated power in a small vacuum gap with that in an infinitely large gap clearly demonstrated the effect of constructive and destructive wave interferences (Fig. 1(d)). More importantly, contribution from evanescent TM modes was shown to be dominant for small gaps (Fig. 1(e)). And compared to the constant heat transfer rate given by Planck's law, several orders of magnitude enhancement in heat transfer between two Cr surfaces across nanometer gaps was predicted at room temperature (Fig. 1(f)). Besides, the temperature dependence of various modes contributing to heat flow was analyzed. Note that the general expressions obtained from this work are semi-analytical, in the sense that they are not in a closed-form and involved integrals that require numerical integration.

A few more theoretical papers were published in the following years.[14,91–95] Similar to previous studies these works also focused on the one-dimensional (1D) configuration of two parallel planes separated by a gap (mostly vacuum) due to both the computational ease as well as scope for a clear demonstration of the underlying physics. Of particular interest is a paper published in 1980 by Levin, Polevoi and Rytov[94] in which, expressions for the heat flux were given in terms of generalized surface impedance tensors, in principle covering anisotropic media with spatial dispersions. Again, a dramatic increase in heat transfer was predicted for small gaps. Please see Hargreaves[94] and Levin *et al.*[92] for detailed comments on these early studies.

Accompanying the early theoretical endeavors around the 1970s were a few carefully designed experiments.[96–101] Utilizing the parallel-plane configuration, all of which demonstrated a definitive dependence of radiative heat transfer on the spatial separations between emitting and receiving bodies from cryogenic to room temperatures, observing mostly few-fold enhancement of heat transfer at small gaps within the micrometer range. A detailed discussion is given in Sec. IV.

Relatively few publications are found through the 1980s and 1990s concerning near-field thermal radiation. However, inspired and powered by the ever advancing micro- and nano-technologies, the dawn of this century has witnessed a rekindled interest, featuring exciting diversity in theoretical and numerical studies as well as unprecedented precision in experimental investigations, which comprise the topics of Secs. III and IV, respectively.

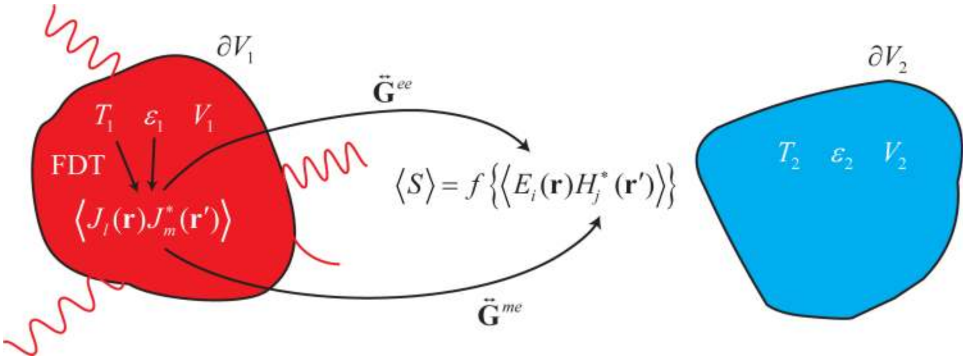

FIG. 2. Schematic of radiative heat transfer in a two-body system in vacuum. The bodies have uniform temperatures T_1 and T_2 throughout their volumes V_1 and V_2. The material properties are described by the frequency dependent complex dielectric functions ε_1 and ε_2. Electromagnetic fields $\mathbf{E}$ and $\mathbf{H}$ are generated by the random currents $\mathbf{J}$ in the bodies due to their non-vanishing correlations given by the FDT. The field correlations are related to the current correlations via the corresponding Green's dyads, and a linear combination of them yields the Poynting vector, which gives the heat current of interest.

III. ANALYTICAL AND NUMERICAL METHODS

Central to most modern studies of thermal radiation is the intuitive picture of thermally driven fluctuating electromagnetic currents and fields. According to the fluctuation-dissipation theorem (FDT) of Callen and Welton,[11] the correlation between random temperature-driven electrical currents is directly related to the dielectric properties of a medium. When the macroscopic Maxwell's equations are solved with the random currents as sources (modeled using the FDT), the thermally excited energy flux (energy flow per unit time per unit area) is obtained from the ensemble-averaged Poynting vector. This basic framework for computing NFRHT is called the fluctuational electrodynamics (FE) formalism.[15,16] Since heat transfer occurs between bodies at different temperatures, a key assumption of FE is that the current fluctuations are solely characterized by the FDT at the corresponding local thermodynamic temperature, and are independent of the incident radiation from the other objects. Several widely available books and reviews[19–27,102–106] describe the theoretical approaches and numerical methods based on FE that are used to study NFRHT, therefore here we provide only a concise summary. However, before we begin, it should be noted that theoretical considerations other than the FE formalism have also been proposed.[107–109]

A. Green function formalism

As an analytical method, the Green function (GF) formalism has distinct advantages and limitations. Expectedly, it has been used almost exclusively for highly symmetric configurations involving infinite planes, dipoles, spheres and cylinders. Whenever applicable, it yields semi-analytical or even closed-from exact solutions, where the contributions from different electromagnetic modes are naturally separated. Further, the GF formalism is amenable to parametric analysis and optimization can be readily applied, allowing opportunities for gaining physical insights. A brief outline of this method is given below, following the existing rich publications.

1. Governing equations and problem solving procedure

Let us consider a system comprising of only two separated bodies, as illustrated in Fig. 2. Assuming a time convention of $e^{-i\omega t}$, the frequency domain macroscopic Maxwell's equations[110,111] with random currents as the source[90] of thermal radiation can be written as

$$\nabla\times\mathbf{E}(\mathbf{r},\omega) = i\omega\mathbf{B}(\mathbf{r},\omega)\,, \tag{3.1}$$

$$\nabla\times\mathbf{H}(\mathbf{r},\omega) = -i\omega\mathbf{D}(\mathbf{r},\omega)+\mathbf{J}(\mathbf{r},\omega)\,. \tag{3.2}$$

Here, $\mathbf{E}$ and $\mathbf{B}$ are the complex electric and magnetic field vectors, $\mathbf{r}$ is the position vector and ω is the angular frequency, $\mathbf{D}$ and $\mathbf{H}$ are the electric displacement and magnetic induction, respectively, and are related to $\mathbf{E}$ and $\mathbf{H}$ via constitutive relations. For example, in isotropic media $\mathbf{D} = \varepsilon_0\varepsilon\mathbf{E}$ and $\mathbf{B} = \mu_0\mu\mathbf{H}$, where ε_0 and μ_0 are the vacuum permittivity and permeability, $\varepsilon(\omega) = \varepsilon'(\omega) + i\varepsilon''(\omega)$ is the frequency-dependent complex dielectric function (relative permittivity) and $\mu(\omega) = \mu'(\omega) + i\mu''(\omega)$ is the relative permeability. All the fields above and below are functions of ω unless otherwise stated. Note that we do not explicitly incorporate any random magnetic current term in the curl equation for the electric field. For more general expressions please see Refs. 105, 112, and 113. We also assume non-magnetic materials with $\mu = 1$. Equation (3) leads to the following vector Helmholtz equations governing the electromagnetic waves:

$$\nabla \times \nabla \times \mathbf{E}(\mathbf{r},\omega) - \varepsilon(\omega)\left(\frac{\omega}{c}\right)^2 \mathbf{E}(\mathbf{r},\omega) = i\omega\mu_0\mathbf{J}(\mathbf{r},\omega), \tag{4.1}$$

$$\nabla \times \nabla \times \mathbf{H}(\mathbf{r},\omega) - \varepsilon(\omega)\left(\frac{\omega}{c}\right)^2 \mathbf{H}(\mathbf{r},\omega) = \nabla \times \mathbf{J}(\mathbf{r},\omega). \tag{4.2}$$

In practice only one of the two equations needs solved given the relation $\nabla \times \mathbf{E}(\mathbf{r},\omega) = i\omega\mu_0\mathbf{H}(\mathbf{r},\omega)$.

The free electric currents $\mathbf{J}$ are associated with fluctuating charges in the medium of interest and satisfy the statistical correlation function below given by the fluctuation-dissipation theorem:[11]

$$\left\langle J_l(\mathbf{r},\omega)\, J_m^*(\mathbf{r}',\omega)\right\rangle = \frac{4}{\pi}\varepsilon_0\varepsilon''(\omega)\omega\Theta_0(\omega,T)\,\delta_{lm}\delta(\mathbf{r}-\mathbf{r}'), \tag{5}$$

where

$$\Theta_0(\omega,T) = \hbar\omega\left(\frac{1}{2} + \frac{1}{e^{\hbar\omega/k_BT} - 1}\right) \tag{6}$$

is the mean energy of a harmonic oscillator including the zero point contribution; $\hbar = h_P/2\pi$ is the reduced Planck constant; T is the absolute temperature and the superscript * denotes the complex conjugate. The Kronecker delta δ_{lm} indicates no cross coupling between currents in orthogonal directions represented by the subscripts l and m, while the Dirac delta $\delta(\mathbf{r}-\mathbf{r}')$ reflects the assumption of locality, excluding spatial dispersions in the media. Note that a factor of 4 is included in Eq. (5) so only positive frequencies are considered subsequently.[22,24,25,106] Other variations of Eq. (5) with differences only in the constant have also been used in existing literatures.[20,21,105]

When combined with the proper boundary conditions of a given problem, Eqs. (3)-(6) allow for calculation of the spectral radiative heat flux as the ensemble-averaged Poynting vector $\langle\mathbf{S}(\mathbf{r},\omega)\rangle = \mathrm{Re}\langle\mathbf{E}\times\mathbf{H}^*\rangle/2$. It can be expressed in terms of the known $\left\langle J_l(\mathbf{r},\omega)\, J_m^*(\mathbf{r}',\omega)\right\rangle$ by using the dyadic Green functions (also referred to as Green dyads)[114] $\overset{\leftrightarrow}{\mathbf{G}}{}^{ee}(\mathbf{r},\mathbf{r}',\omega)$ and $\overset{\leftrightarrow}{\mathbf{G}}{}^{he}(\mathbf{r},\mathbf{r}',\omega)$ via the relations[20]

$$\mathbf{E}(\mathbf{r},\omega) = i\omega\mu_0\int_V d\mathbf{r}'\overset{\leftrightarrow}{\mathbf{G}}{}^{ee}(\mathbf{r},\mathbf{r}',\omega)\cdot\mathbf{J}(\mathbf{r}',\omega), \tag{7.1}$$

$$\mathbf{H}(\mathbf{r},\omega) = \int_V d\mathbf{r}'\overset{\leftrightarrow}{\mathbf{G}}{}^{me}(\mathbf{r},\mathbf{r}',\omega)\cdot\mathbf{J}(\mathbf{r}',\omega). \tag{7.2}$$

Key to this approach is then finding analytically the dyadic Green functions which satisfy the wave equations below with Dirac delta sources for a given configuration:

$$\nabla\times\nabla\times\overset{\leftrightarrow}{\mathbf{G}}{}^{ee}(\mathbf{r},\mathbf{r}',\omega) - \varepsilon(\omega)\left(\frac{\omega}{c}\right)^2\overset{\leftrightarrow}{\mathbf{G}}{}^{ee}(\mathbf{r},\mathbf{r}',\omega) = \overset{\leftrightarrow}{\mathbf{I}}\delta(\mathbf{r}-\mathbf{r}'), \tag{8.1}$$

$$\nabla\times\nabla\times\overset{\leftrightarrow}{\mathbf{G}}{}^{me}(\mathbf{r},\mathbf{r}',\omega) - \varepsilon(\omega)\left(\frac{\omega}{c}\right)^2\overset{\leftrightarrow}{\mathbf{G}}{}^{me}(\mathbf{r},\mathbf{r}',\omega) = \nabla\times\left[\overset{\leftrightarrow}{\mathbf{I}}\delta(\mathbf{r}-\mathbf{r}')\right], \tag{8.2}$$

where $\overset{\leftrightarrow}{\mathbf{I}}$ is the identity dyad. Similar to Eq. (4), only one of the two equations needs solved. Note that the Green dyads for many of the aforementioned simple geometries have long been obtained in the electromagnetism community and can be readily used.[114,115] Below we give the expression of the field correlations in terms of the current correlations and the Green dyads as[20]

$$\left\langle E_i\left(\mathbf{r},\omega\right) H_j^*\left(\mathbf{r}',\omega\right)\right\rangle = i\omega\mu_0\left\langle \int_V d\mathbf{r}' G_{il}^{ee}\left(\mathbf{r},\mathbf{r}',\omega\right) G_{jm}^{me*}\left(\mathbf{r},\mathbf{r}'',\omega\right) \int_V d\mathbf{r}'' J_l\left(\mathbf{r}',\omega\right) J_m^*\left(\mathbf{r}'',\omega\right)\right\rangle, \qquad (9)$$

where the subscripts i and j denote spatial directions. Using Eq. (5) and the Delta functions therein, Eq. (9) can be further written as[20]

$$\left\langle E_i\left(\mathbf{r},\omega\right) H_j^*\left(\mathbf{r}',\omega\right)\right\rangle = i\frac{4\varepsilon''(\omega)\omega^2}{\pi c^2}\Theta_0\left(\omega,T\right) \int_V d\mathbf{r}' G_{il}^{ee}\left(\mathbf{r},\mathbf{r}',\omega\right) G_{jl}^{me*}\left(\mathbf{r},\mathbf{r}',\omega\right). \qquad (10)$$

Here the equality $\varepsilon_0\mu_0 c^2 = 1$ has been used. Since the spectral heat flux $\langle \mathbf{S}\left(\mathbf{r},\omega\right)\rangle$ is a linear combination of these field correlations, the radiative heat flux can be readily obtained. An integral of $\langle \mathbf{S}\left(\mathbf{r},\omega\right)\rangle$ with respect to the angular frequency yields the total heat flux $\langle \mathbf{S}\left(\mathbf{r}\right)\rangle$; and integration of the normal component of $\langle \mathbf{S}\left(\mathbf{r}\right)\rangle$ over the entire surface of the object of interest gives the net heat current (energy flow per unit time).

2. *Thermal radiation in parallel-plane systems*

Based on the concepts and the general procedure outlined above, thermal emission of isolated bodies as well as radiative thermal transport between different objects can be described. We now present as an example the solution of radiative heat transfer between two parallel semi-infinite bodies separated by a vacuum gap (Fig. 1(a), 1(b)), making use of the well-known Green function for this geometry.[20,115] Due to its simplicity, the parallel-plane configuration became one of the first NFRHT problems analytically solved. The study of such parallel configurations has since allowed numerous physical insights to be obtained. Written in a Landauer-type expression, the total heat flux across a vacuum gap d is given by

$$q(T_1,T_2,d) = \int_0^\infty \frac{d\omega}{4\pi^2}\left[\Theta(\omega,T_1) - \Theta(\omega,T_2)\right] \int_0^\infty dk k\left[\tau_s(\omega,k) + \tau_p(\omega,k)\right], \qquad (11)$$

where $\Theta(\omega,T) \equiv h\omega/[\exp(h\omega/k_B T) - 1]$ is the mean energy of a harmonic oscillator less the zero point contribution; T_i are the absolute temperatures, with subscripts 1 and 2 denoting the emitter and receiver, respectively; the vacuum gap is denoted with subscript 0; k is the wave vector component parallel to the planar surfaces, and τ_s and τ_p are the transmission probabilities for the TE and TM modes, respectively. These probabilities can be expressed in terms of the Fresnel coefficients of the interfaces as follows,[116]

$$\tau_{\alpha=s,p}^{12}(\omega,k) = \begin{cases} \dfrac{(1-\left|r_\alpha^{01}\right|^2)(1-\left|r_\alpha^{02}\right|^2)}{\left|D_\alpha\right|^2}, & \text{if } k < \omega/c, \text{ propagating waves} \\ \dfrac{4\,\mathrm{Im}\left(r_\alpha^{01}\right)\mathrm{Im}\left(r_\alpha^{02}\right)e^{-2\mathrm{Im}(\zeta_2)d}}{\left|D_\alpha\right|^2}, & \text{if } k > \omega/c, \text{ evanascent waves} \end{cases} \qquad (12)$$

In Eq. (12), r_α^{ij} are the Fresnel reflection coefficients at the interfaces between vacuum and the two half spaces, and are given by $r_s^{ij} = \left(\zeta_i - \zeta_j\right)/\left(\zeta_i + \zeta_j\right)$ and $r_p^{ij} = \left(\varepsilon_j\zeta_i - \varepsilon_i\zeta_j\right)/\left(\varepsilon_j\zeta_i + \varepsilon_i\zeta_j\right)$, where $\zeta_i = \sqrt{\varepsilon_i\left(\omega\right)\omega^2/c^2 - k^2}$ is the transverse component (perpendicular to the planes) of the wave vector in layer i and $\varepsilon_i(\omega)$ is the corresponding frequency-dependent complex dielectric function. $D_\alpha = 1 - r_\alpha^{01} r_\alpha^{02} e^{2i\zeta_2 d}$ is the Fabre-Pérot-like denominator.

As useful as Eqs. (11) and (12) are, they have been derived only to calculate radiative heat flux between half spaces (or thick objects in practice) and are not adequate to describe systems featuring thin films and layers which are of significant technical importance. When the emitter and/or receiver are not semi-infinite, but instead are multilayer systems (including thin films) with internal interfaces and finite thicknesses, a direct calculation of the radiative heat flux proves difficult as many emission sources (the layers) and/or multiple reflections at interfaces have to be properly accounted for. Alternatively, one can focus instead only on the field inside the vacuum gap and obtain formally the same expression as given in Eq. (11), only that Eq. (12) is now replaced with the one below:[105,117]

$$\tau^{12}_{\alpha=s,p}(\omega,k)=\begin{cases}\dfrac{(1-|R^1_\alpha|^2)(1-|R^2_\alpha|^2)}{|D_\alpha|^2}, & \text{if } k<\omega/c, \text{ propagating waves}\\ \dfrac{4\,\mathrm{Im}\left(R^1_\alpha\right)\mathrm{Im}\left(R^2_\alpha\right)e^{-2\mathrm{Im}(\zeta_2)d}}{|D_\alpha|^2}, & \text{if } k>\omega/c, \text{ evanascent waves}\end{cases} \tag{13}$$

where the Fresnel coefficients r^{ij}_α are replaced by R^i_α, which are the total reflection coefficients of the multilayer systems as seen from inside the vacuum gap, and can be calculated using textbook[111] procedures from all the interface Fresnel coefficients. In the case of half spaces R^i_α reduce to the vacuum interface Fresnel coefficients, thus reproducing Eq. (12).

In order to present results in a form that enables direct comparisons with experiments performed under a small temperature differential, the linear thermal conductance (heat current per unit temperature difference) or heat transfer coefficient (thermal conductance per unit area, h) at a mean temperature T can be obtained from:

$$h(T,d)\equiv\lim_{(T_1-T_2)\to 0}\left|\frac{q(T_1,T_2,d)}{T_1-T_2}\right|=\int_0^\infty\frac{d\omega}{4\pi^2}\frac{\partial\Theta(\omega,T)}{\partial T}\int_0^\infty dk\,k\left[\tau_s(\omega,k)+\tau_p(\omega,k)\right]\equiv\int_0^\infty d\omega h_\omega(T,d), \tag{14}$$

where the spectral heat transfer coefficient h_ω is also introduced.

The planar configuration as solved above using the GF formalism has proven suitable for analyzing a wide variety of media.[45,46,90,94,95,105,112,113,116–169] Equations (11)-(14) can even be readily used for structured and composite materials with their dielectric responses modeled using the effective medium theories (EMT).[19] These are covered in greater detail in Sec. III C. Apart from computing NFRHT between parallel planes, the GF formalism has also been used for a range of other basic configurations including dipole-plane, dipole-dipole, sphere-sphere, sphere-plane and cylinder-cylinder.[18,127,170–180]

In addition to the radiative heat flux and thermal conductance, a few other physical quantities essential for the description of the thermal near-field have been discussed. These include the electromagnetic energy density and the closely-related local density of states (LDOS), the spatial and temporal coherence lengths of thermal radiation, as well as the energy flow path and the penetration depth.[29–36,181–191] All of them can be characterized using the electromagnetic dyadic Green functions, and show strong distance-dependence due to the dominant contributions from evanescent waves in the vicinity of surfaces. Further, some thermodynamic analyses of near-field radiative transport have been performed.[192–195] Expressions of entropy density and entropy flux accompanying near-field thermal radiation were proposed; and implications to the thermodynamic limit of energy conversion efficiencies in the near-field were discussed. We do not discuss these ideas in great detail here as they would take us too far from the focus of this review. However, select results will be briefly introduced in Secs. III C and IV C.

B. Numerical methods

Although the GF formalism is very useful for studying simple geometries and for obtaining insight into the relevant physical mechanisms it cannot be fruitfully used for exploring NFRHT in complicated geometries. The increasing need to go beyond basic geometries, due to rapid developments in the fabrication of nanoscale devices, has led to the establishment of several numerical approaches. To this end, approximation schemes such as the so-called Derjaguin approximation method were initially used to approximate simple curved surfaces with a set of planes, closely mirroring a similar approach that was developed for studying near-field forces.[196] Although accurate in certain cases, its general validity is questionable and hence should be used with caution.[180,197] For geometries with well-defined periodicities, the semi-analytical method of rigorous coupled-wave analysis has at times been used.[26,198]

Most importantly, in light of the above discussions on fluctuational electrodynamics and the GF formalism, it can be seen that the process of radiative heat transfer between various bodies reduces to a consideration of electromagnetic wave scattering problems. Consequently, it is to be expected that existing electromagnetic methodologies could in principle be adapted for NFRHT calculations.[199] Indeed, benefiting from decades of progress in computational classical electrodynamics, the past few years have seen the establishment of quite a few numerical formalisms, many of which are capable of calculating radiative heat transfer between bodies of arbitrary shapes and materials across a range of physically meaningful separations. These formalisms include the scattering matrix approach,[102,103,106,197,200–207] the fluctuating surface current formulation,[104,106,208,209] the finite difference time domain approach,[106,209–213] the Wiener chaos expansion method[214,215] and the thermal discrete-dipole approximation.[216] Although concerned with the same physical problem, these methods differ in how the analysis is conceptually and mathematically formulated. Since significant trade-offs are associated with each of these techniques in terms of the generality, simplicity and efficiency it is not clear if any one technique is superior to others in all circumstances.[199] Therefore, without delving into too many mathematical details, we summarize the ideas underpinning each method, together with the key features and representative results.

1. *Derjaguin approximation*

In order to handle problems that were not amenable to direct calculations early researchers devised relatively simple procedures to obtain approximate solutions for complex geometries using known solutions for simpler configurations. One such procedure is the Derjaguin approximation (DA) scheme,[217,218] which allows calculation of the radiative thermal conductance between simple curved surfaces via solutions of a corresponding parallel-plane system. Examples of problems that were analyzed using this approach include NFRHT between spheres[180] and between a sphere and a plane,[217,218] both of which are challenging to analyze using the Green function formalism especially at small gap sizes due to slow numerical convergence. The basic idea of the DA approach can be described by considering how it is used for understanding NFRHT between a sphere and a plane. In this problem the curved surface is approximated by a set of annuli all parallel to the planar system with different gap sizes, and the sphere-plane thermal conductance is calculated as the sum of contributions between individual annulus and the planar surface. Specifically, the sphere-plane conductance is given by

$$G(T,d) = \int_0^R 2\pi r\, h(T,\overline{d}(r))\, dr, \tag{15}$$

where R is the radius of the sphere, h is the linear heat transfer coefficient between the planar multilayer systems given by Eq. (14), and $\overline{d}(r) = d + R - \sqrt{R^2 - r^2}$ is the local distance between the plane and the annulus with a radius of r (Fig. 21(b)).

It has been suggested[180] that to get the correct near-field thermal conductance using this approximation, the far-field contribution has to be accounted for systematically via distance-dependent view factors considered when needed. Although limited in its capacity the DA approach provides the simplest recipe for approximately obtaining the near-field thermal conductance in complicated geometries.

2. *Scattering matrix approach*

The scattering matrix formalism is arguably the most general method available for calculating both Casimir force and radiative heat transfer between many bodies of arbitrary shapes, materials, temperatures and separations (Fig. 3(a)).[102,103,106,197,201–207] As demonstrated by Krüger and coworkers,[103] the thermal radiation of an isolated body as well as radiative heat currents between bodies at different temperatures can be written in compact, basis-independent trace formulas that depend on both the scattering operators ($\hat{\mathbf{T}}$) of individual objects and the operator form ($\hat{\mathbf{G}}_0$) of the free space Green function.[114] The $\hat{\mathbf{T}}$ operator of an object completely characterizes its scattering behavior, encoding in it both the geometric and physical properties of the object. It can be derived by use of the Lippmann-Schwinger equation, and is related to the corresponding dyadic Green function by $\hat{\mathbf{G}} = \hat{\mathbf{G}}_0 + \hat{\mathbf{G}}_0\hat{\mathbf{T}}\hat{\mathbf{G}}_0$.[103,202] One notable feature of the scattering approach is how it naturally tracks the radiation from each body and its scatterings by the other object, i.e. it is possible to identify

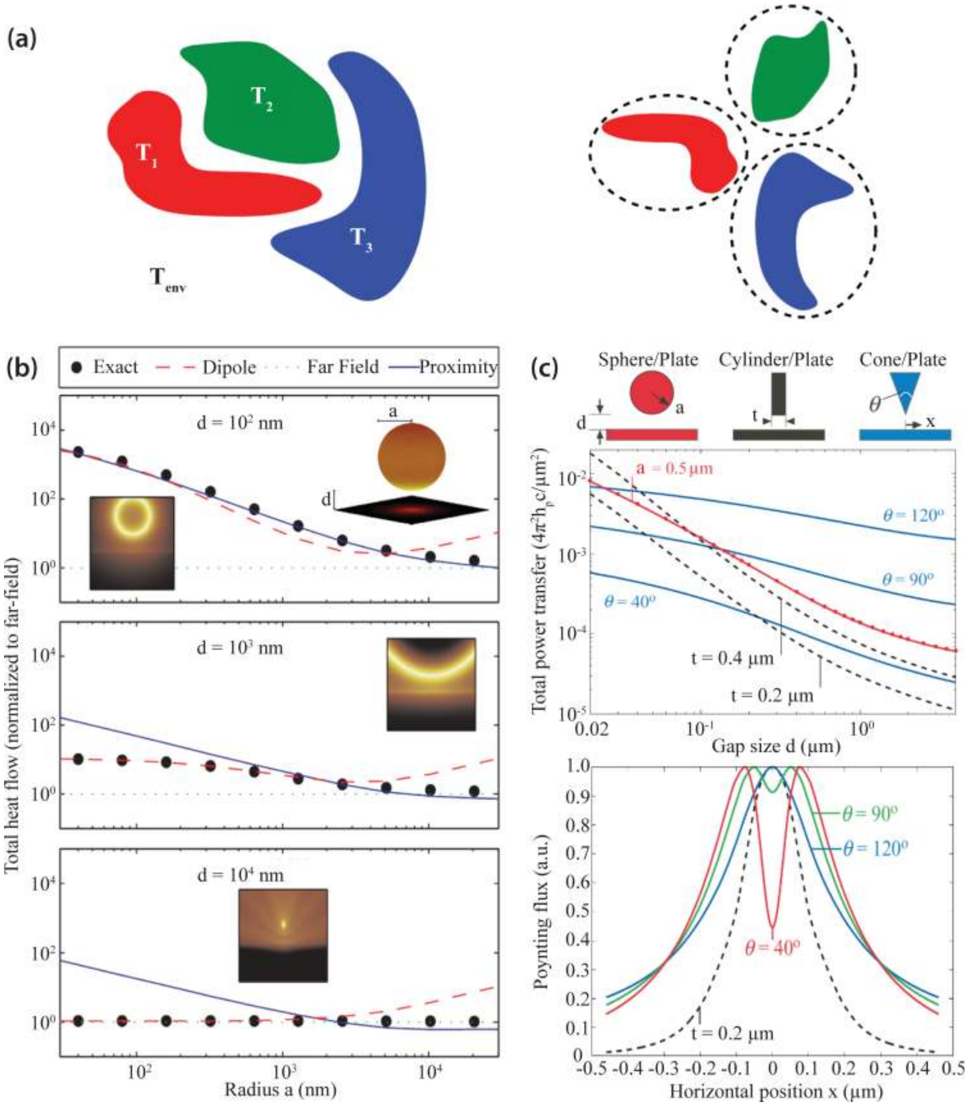

FIG. 3. Scattering matrix formalism as a general method for computing NFRHT. (a) Schematic of many-body systems to which the scattering approach can be applied.[103] The system on the right permits a partial wave expansion in appropriate coordinate systems while the left one requires a more general basis. Temperature of the environment is explicitly labeled as it affects the radiative heat transfer. (b) Comparison of the numerically exact solution for NFRHT between a sphere and a plane with approximation schemes for various sphere diameters and gap sizes.[197] (c) Upper panel: Solutions of NFRHT between silica plates and doped silicon objects of various shapes using a hybrid scattering approach.[205] Lower panel: Spatial distribution of heat transfer on the plate for cone/plate configuration, for which a local minimum is observed right under the cone tip.[205]

how much of the heat flow into one object is contributed by another object of interest.[103] Further, the spatial distribution of the heat flux on the bodies can also be resolved.[205] Moreover, radiation from the environment, which is absent in the GF formalism, can be explicitly included by defining a characteristic temperature,[102,103,203,204] and were shown to affect the radiative heat transfer between two bodies via propagating waves.[102]

Written in an abstract operator form, the radiation from a single body is given by[103]

$$Q\,(T) = \frac{2}{\pi}\int_0^\infty d\omega\Theta(\omega,T)\mathrm{Tr}\left\{\mathrm{Im}[\hat{\mathbf{G}}_0]\mathrm{Im}[\hat{\mathbf{T}}] - \mathrm{Im}[\hat{\mathbf{G}}_0]\mathrm{Im}[\hat{\mathbf{T}}]\mathrm{Im}[\hat{\mathbf{G}}_0]\mathrm{Im}[\hat{\mathbf{T}}^*]\right\}, \qquad (16)$$

where Tr denotes the trace operation. It follows immediately from Eq. (16) that thermal radiation from an object is always positive (positivity of thermal radiation). In a two-body system with the environment neglected as usual, the radiative heat current from the first body to the second, $Q_1^2(T)$, is given by[103]

$$Q_1^2(T_1) = \frac{2}{\pi}\int_0^\infty d\omega\Theta(\omega,T_1)\mathrm{Tr}\left\{\left[\mathrm{Im}[\hat{\mathbf{T}}_2] - \hat{\mathbf{T}}_2^*\mathrm{Im}[\hat{\mathbf{G}}_0]\hat{\mathbf{T}}_2\right]\frac{1}{1-\hat{\mathbf{G}}_0\hat{\mathbf{T}}_1\hat{\mathbf{G}}_0\hat{\mathbf{T}}_2}\right.$$
$$\left.\times\hat{\mathbf{G}}_0\left[\mathrm{Im}[\hat{\mathbf{T}}_1] - \hat{\mathbf{T}}_1^*\mathrm{Im}[\hat{\mathbf{G}}_0]\hat{\mathbf{T}}_1^*\right]\hat{\mathbf{G}}_0^*\frac{1}{1-\hat{\mathbf{T}}_2^*\hat{\mathbf{G}}_0^*\hat{\mathbf{T}}_1^*\hat{\mathbf{G}}_0^*}\right\}. \tag{17}$$

When the two bodies are at the same temperature, one expects the net heat flow $Q_{12} = Q_1^2(T) - Q_2^1(T)$ to be 0. This symmetry (reciprocity) of heat transfer can be formally proved using Eq. (17) and naturally yields the expression of $Q_2^1(T_2)$. It can further be demonstrated that Eq. (17) satisfies the second law of thermodynamics, i.e., that heat is always transferred from a hotter to a colder body.[103]

In order to actually compute with Eq. (16), or Eq. (17), one needs the **T**-matrices, which are the matrix representations of the scattering operators. To this end, one can either choose the partial-wave bases (also called spectral bases) appropriate for the individual objects, or one could calculate the **T**-matrix of each object in other bases using a suitable numerical technique. It should be noted that this calculation only needs to be done once for a given object. Application of the partial-wave expansion approach requires the objects to be properly arranged so each individual can be separated by some high-symmetry shapes (see Fig. 3), for example, with planes and spheres if a plane wave basis or a spherical basis is desired. Specifically, the system on the left side of Fig. 3(a) cannot use partial wave expansion while the system on the right side can.[103] When applicable, a spectral basis in general results in faster numerical convergence. And for systems with high symmetry, such as the parallel-plane or the sphere-sphere configuration, the scattering matrix approach can lead to semi-analytical formulas like the ones obtained using the Green function formalism, which also offers a way to check the validity of the scattering matrix approach.

Apart from these general features and results, we note that the numerically exact solution of NFRHT between a sphere and an infinite plane was first performed using the scattering matrix approach (Fig. 3(b)).[197] Also, radiative heat transfer between a finite-sized cone and a semi-infinite plane was studied using the scattering matrix formalism (Fig. 3(c)),[205] with scattering of the cone treated with the boundary element method (BEM) while the scattering matrix of the plate analytically given. Being the first time a sharp object was studied, it was found that, counterintuitively, the spatial distribution of heat transfer rate exhibits a local minimum (a dip) below the tip of the cone (Fig. 3(c)) where the two objects are closest. As an explanation, it was suggested that as the cone tip becomes sharper, its radiation pattern approaches that of a point dipole with the axis normal to the plate, which has zero Poynting flux at the center.[205]

3. Fluctuating surface current formulation

The fluctuating surface current (FSC) formulation of thermal radiation was introduced by Rodriguez and colleagues[104,208,209] based on the surface-integral-equation (SIE) method of classical electromagnetics.[219] Similar to the scattering matrix approach, it is capable of dealing with systems composed of arbitrary bodies (both systems shown in Fig. 3(a)), including bodies enclosed by other objects. Further, it also results in compact trace formulas for key quantities like emission from an isolated body or radiative heat flux between objects. These trace formulas subsequently allow straightforward demonstration of the positivity and reciprocity properties of thermal radiation. Also, the contribution from the environment to radiative heat transfer can be included.[104]

Although both the scattering approach and the FSC formalism can be expressed in terms of various matrices, their physical meanings usually differ.[106] The key difference between these two formulations lies in how the wave generation and scattering process is conceptually pictured. The scattering matrix approach in general is concerned with a set of incoming and outgoing partial waves related by the scattering matrices, with unknown fields distributed through the volume of the bodies. In comparison, the FSC approach is formulated in terms of unknown electric and magnetic currents existing on the surfaces of the objects. These currents are arbitrary, fictitious vector fields that do not have to satisfy any wave equation, leading to great flexibility in the choice of basis. However, the overall effect of these currents is such that they effectively replace the sources inside the scatterers. The validity of the FSC is found in the well-known equivalence principle of classical electromagnetics.[220]

With suitable spectral bases, the FSC trace formulation also results in semi-analytical results for basic geometric configurations as obtained from the GF approach. However, one is not limited to a few spectral bases.[104] Since the currents exist only on the surfaces, it is possible to use BEM which features a surface rather than volume discretization scheme, potentially reducing the number of unknowns to be solved for. This renders the FSC approach particularly appealing for more complex systems. In practice, the so-called RWG (Rao-Wilton-Glisson) basis[221] has been favored with vector-valued polynomial functions defined locally on a mesh of triangular pads. Such a basis allows improved numerical accuracy with increasingly finer meshing. Unlike the well-known finite element and the finite difference methods, BEM usually results in dense matrices which require intensive matrix operations dominating time consumption for large systems. This makes BEM a good choice for systems of moderate complexity, but not as good for very large systems where a huge amount of computer memory is needed, dramatically decreasing the speed of dense-matrix solvers. Still, it can achieve relatively faster convergence using established algorithms like adaptive mesh refinements.[104] We note that interested readers can explore the free, open-source software implementation of BEM offered by Homer Reid.[222]

The FSC formulation, has been employed recently to analyze NFRHT in a range of novel configurations involving bodies of various shapes and finite sizes. These include two cylinders of various relative orientations (Fig. 4(a)),[104] a cone over a circular plate (Fig. 4(b)),[104] two cones (Fig. 4(b)),[104] two rings (Fig. 4(c)),[208] two circular plates,[208] and a sphere or a cylinder over a perforated plate (Fig. 4(d)).[209] For the case of a cone and a plate, the former result (Fig. 3(c)) regarding the spatial distribution of heat transfer from the scattering matrix approach was confirmed.[205] While for the cylinder versus perforated plate system it was found that, contrary to most systems showing monotonic increase of heat transfer with decreasing separation between bodies, there exists a local maximum heat transfer rate at certain separations with both smaller and larger gaps showing lower rates (Fig. 4(d)).[209] The FSC results were compared and confirmed with the finite difference time domain method, which is discussed next (Fig. 4(d)).[209] Finally, we note that the FSC approach also allows for the surface roughness to be investigated.[223]

4. Finite difference time domain method

In classical electromagnetism, the finite element time domain method (FDTD)[224] is widely employed to obtain the broadband frequency response of a system in a single simulation by computing the Fourier transform of the time response of a system to an impulse excitation. Examples of computed quantities include the absorption, reflection or transmission spectra from structures of interest, making it particularly suitable for designing photonic crystals (Fig. 5(a)) potentially useful in photovoltaic and thermophotovoltaic devices.[210,211] The FDTD method solves the time domain Maxwell's equations by discretizing space and time, and explicitly simulating the evolution of fields. When dealing with thermal emissions, one can either start with the Maxwell's equations, or consider the polarization response $\mathbf{P}(t)$ of a system to a local electric field $\mathbf{E}(t)$ and a random force term $\mathbf{K}(t)$ through a Langevin-type equation of motion,[106,210]

$$\frac{d^2\mathbf{P}}{dt^2} + \gamma\frac{d\mathbf{P}}{dt} + \omega_0^2\mathbf{P} = \sigma_e\mathbf{E} + \mathbf{K}(t), \tag{18}$$

where $\mathbf{P}$ is also connected to $\mathbf{E}$ by the constitutive relation $\mathbf{D} = \varepsilon_0\varepsilon\mathbf{E} = \varepsilon_0\mathbf{E} + \mathbf{P}$; γ represents dissipation in the system; ω_0 and σ_e are respectively the resonance frequency and strength. Vital to either case is the implementation of the random source term, which although is well-defined in frequency domain by the FDT, is not so obvious to construct in the time domain. To this end, various models have been proposed.[106,210,212,213] For example, an approximation to the source term in Eq. (18) is obtained by invoking the FDT, which states that the frequency domain correlation $\langle K_l(\mathbf{r},\omega)\,K_m^*(\mathbf{r}',\omega)\rangle$ for $\mathbf{K}$ is proportional to $\Theta(\omega,T)$. The time correlation function of $\mathbf{K}$ can be obtained via Fourier transform of the frequency domain correlation, however, a direct Fourier

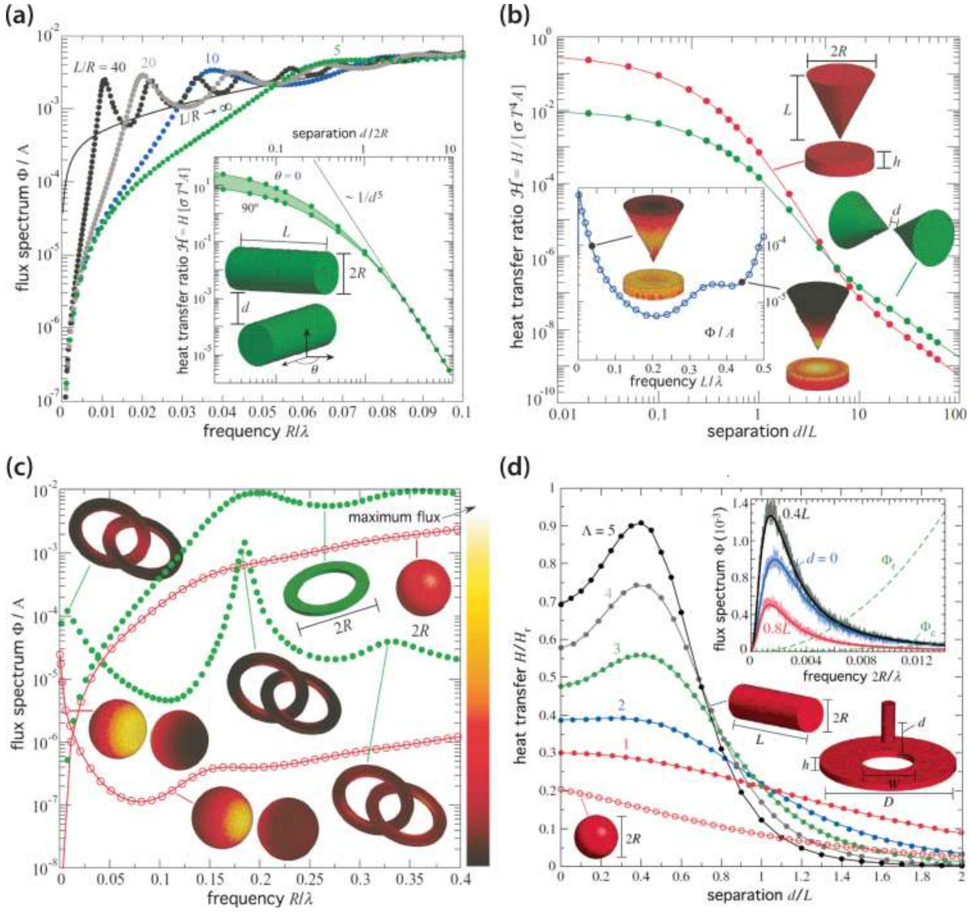

FIG. 4. Selected computational results obtained using the FSC formalism. (a) Normalized radiation spectra for cylinders of different aspect ratios. Inset: Radiative heat transfer between two identical cylinders as a function of their angular alignment.[104] (b) NFRHT between a cone and a plane as well as between two cones as a function of separation. Inset: Radiation spectrum for the cone-plane case with spatial patterns resolved for two different wavelengths.[104] (c) Radiation spectra of isolated and interacting spheres/rings with spatial patterns resolved for several wavelengths.[208] (d) Normalized heat transfer between a ring and a sphere or a set of cylinders with different aspect ratios. A local maximum is observed for cylinders with higher aspect ratios. Inset: Similar results obtained using the finite difference time domain method.[209]

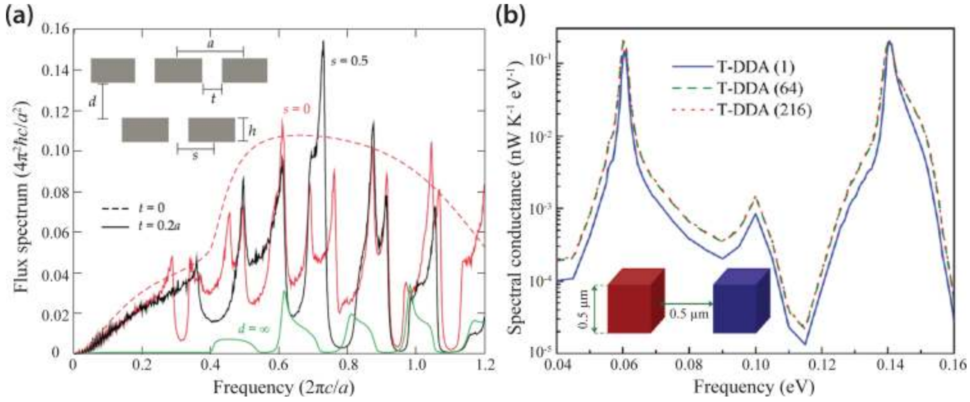

FIG. 5. Selected results obtained using the FDTD and TDDA methods. (a) Flux spectra between photonic crystals of different dimensions obtained with FDTD.[211] These results demonstrate tunable emission peaks instead of broadband spectra. (b) Spectral conductance between two identical nanocubes computed using TDDA.[216]

transform would involve temporal convolution. Consequently, one Fourier-transforms instead the spectrum for $\mathbf{K}'(\mathbf{r},\omega) = \sqrt{\mathbf{K}(\mathbf{r},\omega)}/\Theta(\omega,T)$ which is white. For FDTD implementations working directly with the Maxwell's equations, sources based on fast Fourier transform[212] and the so-called Ricker wavelet[213] have also been independently used. In addition to the source terms, the dielectric properties of materials which are usually measured and modeled as a function of frequency should also be Fourier-transformed to obtain the corresponding susceptibilities in the time domain. Further, in this technique it is necessary to pay careful attention to correctly modelling the boundary conditions.

Being statistical in nature, results from the FDTD method usually look "noisy" and multiple runs need to be performed to obtain meaningful results with acceptable errors.[106,209,211] In spite of the fact that FDTD is a volumetric method it usually requires much less memory in comparison to BEM, due to the sparse nature of the matrices involved. Further, FDTD may be conceptually the most simple and intuitive method for treating arbitrary geometries and materials.

5. Wiener chaos expansion approach

Maxwell's equations with random thermal current sources are stochastic partial differential equations (SPDE), hence in principle they can be solved via popular approaches like the Monte Carlo method as well. Alternatively, one can exploit the Wiener chaos expansion (WCE, also referred to as the Hermite polynomial chaos expansion) method. Separating the deterministic effects from the probabilistic in the solutions of an SPDE, the WCE and other polynomial expansions have a long history of being used in physics and engineering, including discussion of the Navier-Stokes equations.[225] As to the area of thermal radiation, the WCE method provides in essence a way of modeling the current source terms.

Following the notations of Wen,[214] one first assumes that the random current is a separable function of space and time such that

$$J_l(\mathbf{r},t) = dW(\mathbf{r})\,V(t) \tag{19}$$

where $V(t)$ is a deterministic function of time describing the time variation of the current sources, and $dW(\mathbf{r})$ is the derivative of white noise and represents the spatial randomness. And for steady state thermal radiation, $V(t)$ is a constant given by the FDT, capturing the strength of the fluctuation. The key idea in the WCE method lies in the expansion of $dW(\mathbf{r})$ into the linear combination of a set of deterministic, orthonormal current eigenmodes. Subsequently, the effect of $dW(\mathbf{r})$ is obtained as a sum of contributions from these basic current modes. The chief issue then is in identifying the current modes appropriate for a given system.[214,215]

Based on the brief discussions above, it is obvious that the WCE can be combined with the FDTD method. However, it is also natural to use WCE in conjunction with the finite difference frequency domain method.[214,215] The validity of the WCE method in treating thermal radiation problems has been verified using the infinite parallel-plane configuration.[214] Further, it has also been used, instead of the effective medium theory, to compute the emission/absorption properties of hyperbolic metamaterials in the form of metal-wire array.[215]

6. Thermal discrete dipole approximation

The thermal discrete-dipole approximation (TDDA) was proposed[216] based on the well-known discrete-dipole approximation (DDA)[226] in classical electromagnetism, which aims to solve scattering problems by discretizing material bodies into volumes small enough to be considered as electric point dipoles. Established via the same general procedure, TDDA differs from DDA in having the thermal fluctuation of dipoles being the source, instead of incident fields associated with external illumination. A detailed derivation starting from the stochastic Maxwell's equations was given by Edalatpour and coworkers.[216] Briefly, in this analysis the authors start by separating the electric field into the incident and scattered fields, with the incident field interpreted as the thermally generated field propagating in absence of the scatterers. The various criteria of convergence as well as the oscillatory behavior of the solutions with respect to increasing number of dipoles were also discussed.

Similar to DDA, TDDA is expected to be applicable for arbitrary geometries. In order to verify its validity, NFRHT between two spheres was computed and compared to analytical solutions from the Green function formalism. The method was also subsequently used to calculate the NFRHT between two cubes each with a side length of 500 nm (Fig. 5(b)).[216]

C. Results from computational studies

Computational investigations of the electromagnetic near-field have provided deep insights into the novel phenomena that are expected to arise in NFRHT and have highlighted the possibility of coherent, narrowband thermal emissions at emissive powers which are orders-of-magnitude higher than the blackbody radiation limit. These studies have also suggested a range of possibilities where NFRHT can be employed to rectify, amplify and modulate radiative heat flow, and to develop and facilitate a broad range of applications such as energy conversion,[66–82] coherent thermal sources,[29–36] thermal management and data storage,[40–65] lithography,[18] and thermal microscopy.[37–39] Below, we provide a summary of the key computational results and proposals, with a few experimental findings briefly introduced as needed.

1. Heat transfer enhancement and reduction

A large number of computational studies[20–22] have explored the strong gap-size dependence of thermal conductance between semi-infinite parallel plates in the near-field. This is particularly interesting as it is in strong contrast to the gap-independent heat transport predicted by Stefan-Boltzmann law for far-field radiative heat transfer. And this interesting fact about NFRHT was widely noted right from the inception of the field and has since remained one of the most explored characteristics of NFRHT—especially given its great engineering relevance. Recent studies on NFRHT between parallel semi-infinite plates have been concerned with the mechanisms, materials and structures necessary to enhance radiative heat flow beyond what can be readily achieved using metals, which were the focus of early studies.[90]

One of the important advancements[154] was the recognition that NFRHT between polar dielectrics can be significantly higher in magnitude than that between metals (Fig. 6(a)). This is primarily due to a large contribution from surface phonon polaritons (SPhPs), which are coupled surface modes of electromagnetic waves (photons) and lattice vibrations (phonons). Unlike the evanescent waves generated due to frustrated total internal reflections (Fig. 1(a), 1(b)), these resonant surface modes decay exponentially on both sides of the interface. Since the excitation energies of SPhPs of several dielectrics such as silicon dioxide (SiO_2) and silicon carbide (SiC) are comparable to $k_B T$ (25 meV) at room temperature, all these modes are populated and contribute to NFRHT.[154] It is to be noted that although metals support surface plasmon polaritons (SPPs) which are coupled modes between photons and the collective excitations of free electrons (plasmons), the heat flow in the near-field has no significant enhancements due to these modes as their excitation energies are much larger than $k_B T$ at room temperature. In comparison, doped semiconductors such as Si[156–158] feature higher heat flow than metals as they support SPPs at lower energies. In addition to semiconductors like Si, graphene has received a lot of interest[45,72,76,131–134] in computational studies of NFRHT due to the ability to tune its electronic and optical properties in addition to its excellent mechanical and thermal properties. Further, graphene is noteworthy in its ability to support SPPs over a large frequency range, from terahertz to near-infrared (Fig. 6(b)).[132]

Another extensively explored configuration is semi-infinite planar bodies featuring either nanostructured surfaces or heterostructuring (Fig. 6(c)).[117,120,121,123,124,126] These include 1D gratings[211] and periodic layered photonic crystals,[117,120] 2D patterns featuring arrays of holes,[121] nanotubes[122] and nanowires,[129] as well as metamaterials with chirality.[125] It has been suggested that the creations of surface Bloch modes and additional electric and magnetic resonant modes result in a further increase in NFRHT as they open new channels for heat transfer. Magnetic contribution to heat transfer was demonstrated computationally in a composite of potassium bromide matrix and SiC nanospheres (Fig. 6(d)). Further, thin polar dielectric films and coatings can potentially enhance heat transfer beyond their bulk counterparts due to hybridization of the SPhPs on the front and back surfaces

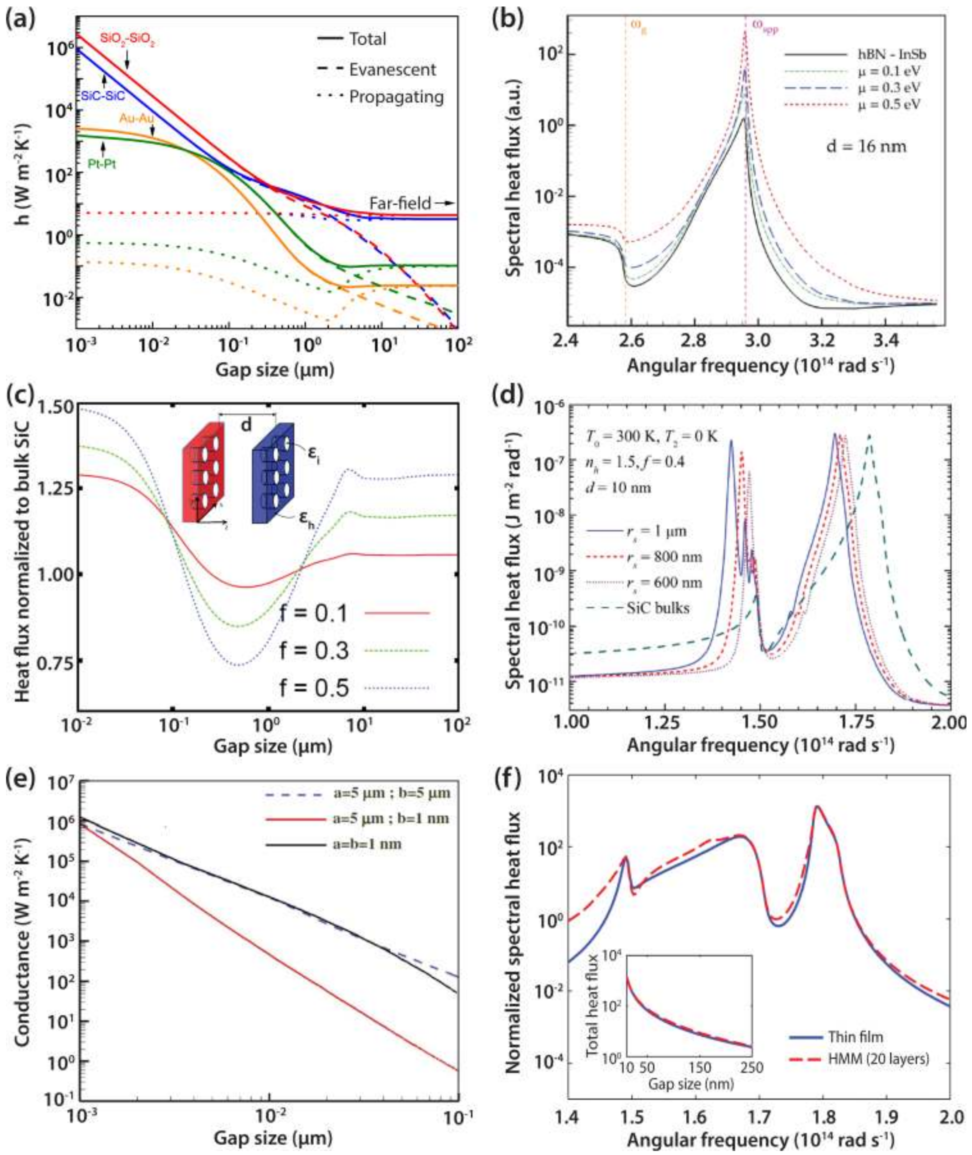

FIG. 6. Schemes to enhance NFRHT. (a) Comparison of heat transfer coefficients between two bulk metals (Au and Pt) and two polar dielectrics (SiC and SiO_2) supporting SPhPs in the mid-infrared. (b) Spectral heat flux between hBN and InSb planes with and without graphene sheets of various chemical potentials.[72] Graphene supports tunable low energy SPPs. (c) Heat flux between perforated SiC half spaces normalized to that of bulk SiC for different filling factors f.[121] (d) Spectral heat flux between two metamaterial (SiC nanospheres in KBr host) planes separated by 10 nm.[126] The excitation of magnetic modes offers an extra channel for NFRHT. (e) Total radiative heat transfer coefficient between SiC films of thicknesses a and b.[165] Performance of thin films can exceed that of bulk materials due to hybridization of SPhPs on their front and back surfaces. (f) Spectral heat flux between two planar hyperbolic metamaterials with 10 units each consisting of 50 nm-thick SiC and 150 nm-thick SiO_2, and that between two 50 nm-thick SiC films coated on SiO_2.[142] The results are very similar.

(Fig. 6(e)).[162–166,168] Finally we note that although the potential of nanostructured hyperbolic metamaterials to greatly enhance heat transfer has been widely discussed,[125,136–141,143] a recent paper pointed out that a thin film with optimized thickness can achieve this as well (Fig. 6(f)).[142]

Apart from computationally probing NFRHT in novel structures and materials, fundamental limits to the magnitude of radiative heat flow have also been obtained, and the maximum heat flow per channel was established[18] to be $3\pi k_B^2 T^2/\hbar$—the quantum of thermal conductance. Further, studies have also focused on parametric optimizations of material dielectric functions aiming to maximize heat currents in the near-field.[144–147,149,150] For example, it was shown that for gaps above

1 nm, materials with dielectric functions in the form of $\varepsilon = -1 + i\alpha$, where $\alpha \ll 1$ yield the maximum heat flow. Note that configurations with spectrally matched emitters and receivers are desired to accomplish such maximization.[144]

Finally, we note that NFRHT could also be used to suppress heat transfer to values below the far-field limit at suitably chosen gap sizes due to interference effects, a phenomenon which was observed by early researchers[90] in their computational studies of NFRHT between metals. Besides, parametric studies were also performed to suppress radiative heat transfer in order to improve thermal insulation.[148] It is important to emphasize, however, that neither the suppression of heat transfer via near-field nor the predicted enhancement of thermal conductance—by several orders of magnitude—has been experimentally confirmed directly in the plane-plane configuration (Fig. 1(b)) at room temperature. This lack of experimental confirmation is primarily due to major instrumentation challenges as described in Sec. IV.

2. Spatial and temporal coherence

Thermal radiation is usually considered to be spatially incoherent, with a coherence length comparable to or smaller than half the wavelength of interest because the emissions are caused by the random fluctuation of charges. As a measure of the spatial correlation of the thermally generated electromagnetic field, the spectrally-resolved spatial coherence length can be characterized using the cross-spectral density tensor $\overset{\leftrightarrow}{\mathbf{E}}(\mathbf{r},\mathbf{r}',\omega)$, whose components are given by $E_{ij}(\mathbf{r},\mathbf{r}',\omega) = \left\langle E_i(\mathbf{r},\omega)\, E_j^*(\mathbf{r}',\omega)\right\rangle$.[29] Mathematical expressions of this tensor for specific systems in terms of the Green dyads can be derived following the discussions and equations in Sec. III A. Indeed, it was numerically shown for tungsten (W, commonly used in incandescent lamps) that the correlation length at a wavelength $\lambda = 500$ nm can be as small as $\sim 0.06\lambda$.[29] However, recent computational inquiries[29–36] into the thermal near-field has shown the possibility of having large partial spatial coherence in thermal emissions. Actually, for materials supporting SPPs and SPhPs, it has been shown (Fig. 7(a)) that the correlation lengths at the respective frequencies can reach many times the resonant wavelength.[29] It is suggested that in the vicinity of the surfaces, the delocalized surface modes (SPPs and SPhPs) which can propagate along the surfaces for tens of wavelength, could pass their spatial coherence to the near-field.[29] At a distance of $z = 0.05\lambda$ away from a plane material surface, both gold (Au) and silver (Ag) exhibit large correlation length at $\lambda = 620$ nm as they support SPPs of this wavelength, as compared to the short correlation for W which do not (Fig. 7(a), upper). For polar dielectrics supporting SPhPs such as SiC, the dominant effect of SPhPs on the spatial coherence is confirmed by comparing the correlation lengths on and off resonance (Fig. 7(a), lower). Apart from revealing spatial coherent thermal emissions in the near-field, Greffet *et al.*[30] have even designed and experimentally tested a highly directional (as compared to Lambertian emission[83]) thermal source working in the far-field in the form of a SiC grating (Fig. 7(b)). The origin of this coherent emission is considered to lie in the diffraction of SPhPs by the grating into the far-field.

The temporal coherence properties of the thermal near-field are indicated by the spectral energy density or density of states,[20] with a broad spectrum implying poor temporal coherence and a narrow one representing better coherence. Similar to the spatial coherence, they have been widely discussed. It is now a well-established fact that in the presence of surface resonant modes like SPhPs, thermal radiation very close to the surface and heat transfer across extremely small gaps can be confined to a very narrow frequency window(s), approaching monochromatic emission (Fig. 7(c)) for nanoscale distances.[20] This characteristic is of key importance to the development of novel thermophotovoltaic devices where the emission peak can be properly matched to the bandgap of the photovoltaic cells—reducing waste heat and increasing device energy conversion efficiency.

3. Gap-dependent penetration depth

A question that received attention recently is regarding the effect of thin films on NFRHT. For example, Francouer *et al.* studied[164] the effect of film thickness on NFRHT and computationally showed considerable enhancement in NFRHT due to contributions from SPhPs. Specifically, they studied NFRHT in two scenarios: 1) between two bulk SiC surfaces and 2) between a 10 nm thick

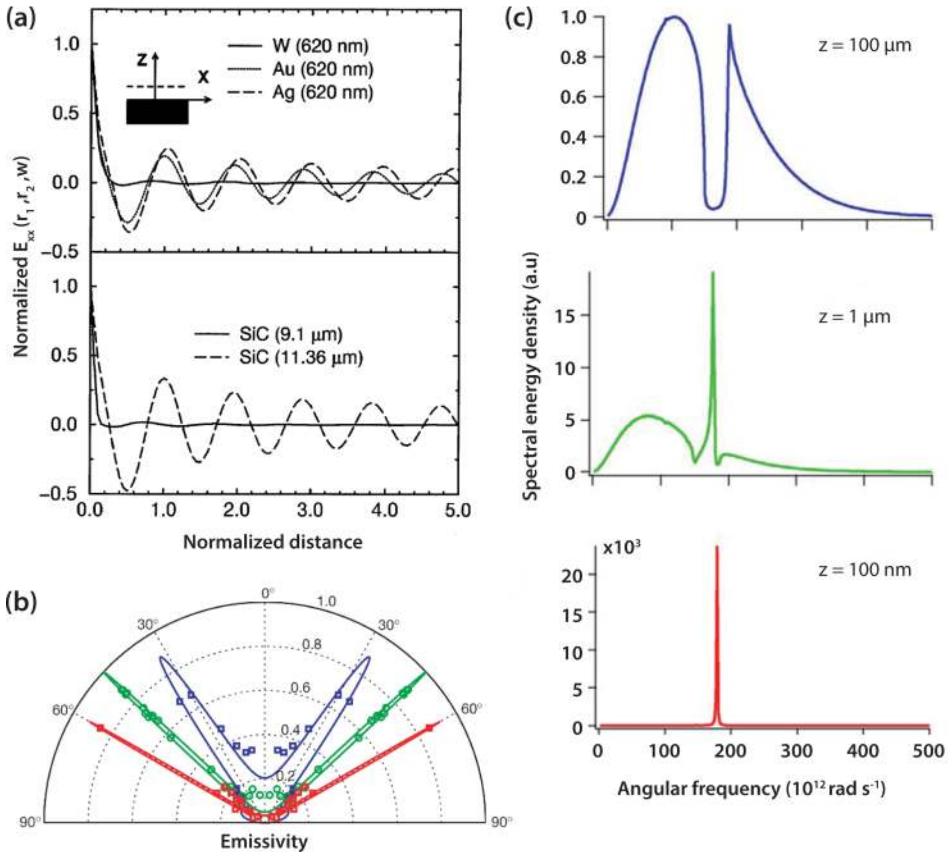

FIG. 7. Coherence properties of thermal radiation. (a) Diagonal element of the electric field cross-spectral density tensor calculated for $z = 0.05\lambda$ above metallic surfaces (upper) and polar dielectric surfaces (lower).[29] (b) Directional emissivity of a SiC grating for $\lambda = 11.04$ (blue), 11.36 (red), and 11.86 μm (green).[30] The SPhP mode on SiC is coupled into highly directional far-field emission. (c) Spectral energy density calculated above a SiC half space for different distances from the surface.[20]

SiC emitter and a bulk SiC receiver. They showed that the total radiative flux is 2.2 times larger in the latter scenario due to coupling of SPhPs in the film. Further, Fu *et al.* studied the effect of film thickness on NFRHT by computationally studying NFRHT between a bulk SiC substrate and an aluminum (Al) metal surface coated with SiO_2 films of different thicknesses (10 nm, 100 nm, 1 μm, 10 μm and infinite thickness). They concluded that the NFRHT enhancement by the thinner films is significantly smaller than that of thicker films at large gap sizes but becomes almost identical to the thicker film at very small gap sizes (~10 nm). They argued that at small gaps NFRHT is dominated by the SPhPs and hence even a film as thin as 10 nm can act like a bulk film. Moreover, Basu *et al.* computationally studied[184] the penetration depth of evanescent waves between two semi-infinite SiC surfaces and doped Si surfaces. From their studies they concluded that extremely small skin depths can exist and argued that the skin depth is proportional to the spatial separation between the surfaces. More recently, Song *et al.* experimentally and computationally studied[223] the effect of both film thickness and gap size on NFRHT and demonstrated that NFRHT between a thin SiO_2 film and a thick SiO_2 substrate becomes identical to that between two thick SiO_2 surfaces when the gap size becomes smaller than the film thickness. They explained these results in terms of the mode shapes of cavity surface phonon polaritons and how the transmission properties of these modes are affected upon varying the gap size. More details of the experiments and the analysis is presented in Sec. IV D.

4. *Modulation of heat flow*

Proposals to modulate radiative heat flow have been made based on various mechanisms.[43–51] One theoretically trivial idea is modulation of the gap size. Beyond that, the first and most

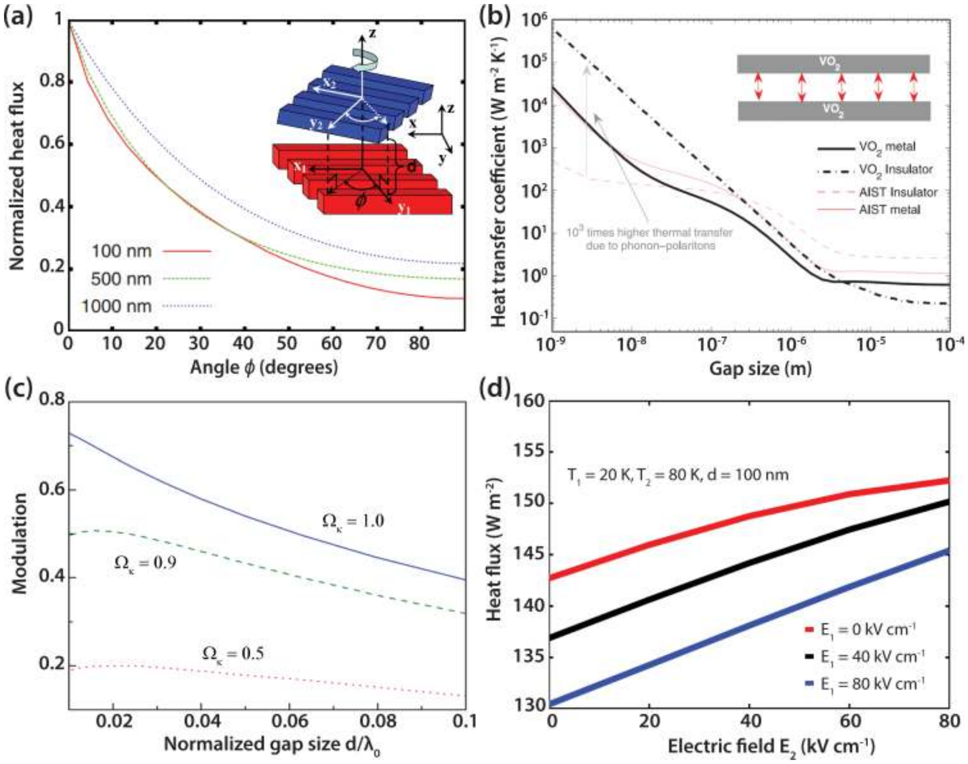

FIG. 8. Modulation of radiative heat flow. (a) Normalized heat flux calculated for two Au gratings as a function of their angular alignment.[135] (b) Heat transfer coefficient versus gap size predicted for parallel VO_2-VO_2 plates (black) and AIST-AIST plates (red) in the metallic (solid) and insulating (dashed) phases.[43] (c) Relative difference of heat transfer coefficients between chiral metamaterials of different resonance strengths Ω_κ.[46] Chiral metamaterials with optically tunable chirality are proposed as potential candidates for ultrafast tuning of NFRHT. (d) Predicted heat flux between ferroelectric planes separated by 100 nm in the presence of varying electric fields.[48]

straightforward scheme exploits the dependence of NFRHT on the geometric asymmetry of the surfaces or objects. For example, since NFRHT between two gratings (Fig. 8(a))[135] or two cylinders (Fig. 4(a), inset)[104,208] depends on their angular alignment, NFRHT can be controlled by changing the relative orientation. Further, translational alignment can also be used to affect the NFRHT between two-grating configurations without changing the gap size. It was also shown that NFRHT between anisotropic nanoparticles can be modulated by controlling their orientations.[51] Another computational approach leverages phase change materials,[43,44] as a change of phase inevitably leads to dramatic change in material dielectric properties (Fig. 8(b)). These include a material called AIST (an alloy of silver, indium, antimony, and tellurium, already commercially used for memory cells)[44] and materials which experience metal-insulator transitions (MIT, for example VO_2).[43] Phase change of AIST can be easily achieved by applying external electric field, while MIT occurs when a critical temperature (T_C) is crossed. We note that MIT of VO_2 (T_C = 340 K) leads to a much more significant increase of heat flow due to contribution from the SPhPs supported in its insulating (dielectric) phase. Further, computations suggest[125] that NFRHT in chiral materials (Fig. 8(c)) with magnetoelectric coupling can potentially be tuned by ultrafast optical pulses. It has also been suggested that NFRHT between ferroelectric materials can be tuned[48] with external electric field (Fig. 8(d)). At last, we note that very few of these proposals have actually been experimentally realized.

5. Thermal diodes

Rectification of heat flow refers to the situation where the magnitude of heat current depends on the direction of applied thermal bias.[227,228] A device that rectifies heat flow is often referred to as a

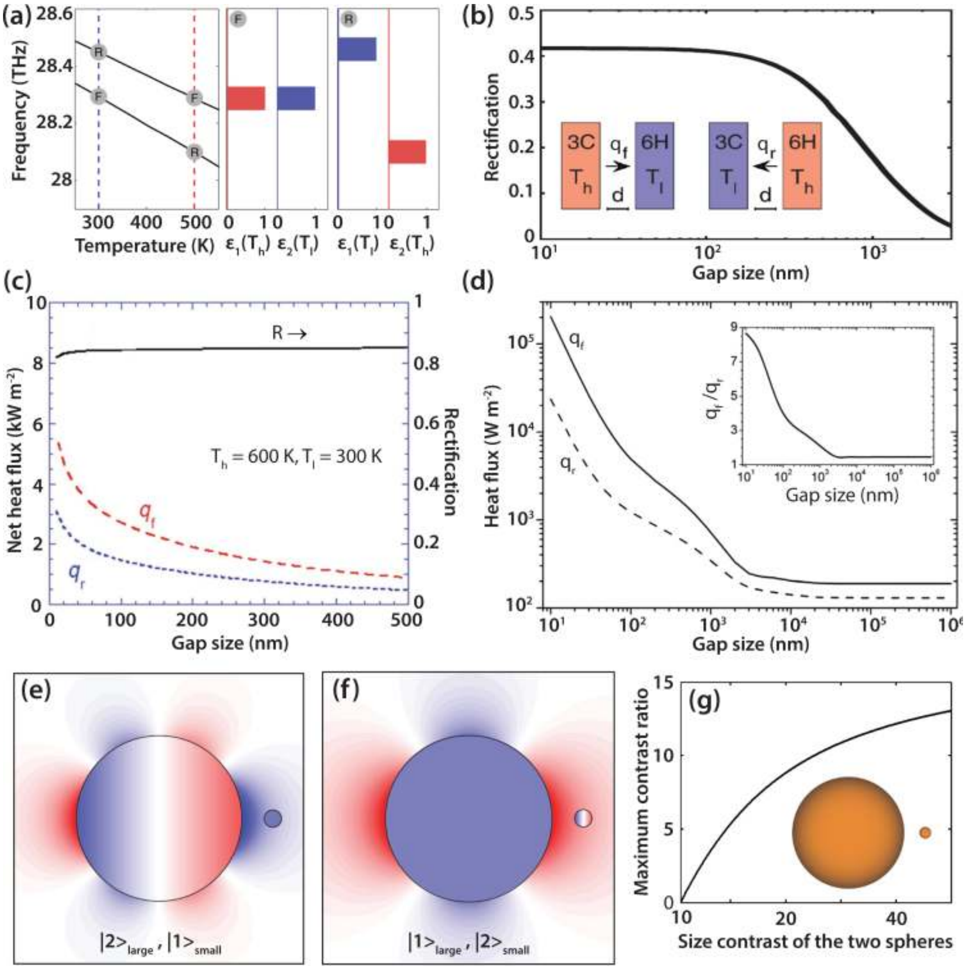

FIG. 9. Thermal diodes. (a) Schematic of radiative thermal rectification due to temperature dependent material dielectric functions.[52] In the forward (F) scenario, dielectric functions are nearly equal and heat flux is enhanced. In the reverse (R) scenario, dielectric functions differ and heat flux is attenuated. (b) Predicted rectification between 3C-SiC and 6H-SiC versus gap size.[52] (c) Rectification calculated between intrinsic Si and Au.[57] (d) Predicted rectification between two MIT materials: VO_2 and LCMSO.[56] (e)-(f) Illustration of geometry-induced rectification between a relatively large and small nanosphere.[58] (g) Rectification versus the ratio between sphere diameters.[58]

thermal diode in analogy to an electrical diode. The defining characteristic of a thermal diode is the degree of asymmetry in the forward (Q_f) and reverse (Q_r) heat currents when an identical temperature differential is applied in two different directions, where forward typically corresponds to the direction that results in a larger Q_f than Q_r. Slightly different definitions of the rectification capacity have been used by different research groups in the past. Below, we follow the commonly used definition of thermal rectification ratio $R_{fr} = (Q_f - Q_r)/Q_r$.[229] Although thermal diodes based on heat conduction and convection have long been proposed and studied, radiative thermal diodes were only proposed in recent years, exploring both near-field[52–54,56–58,60] and far-field thermal radiation.[55,59,61]

The first proposal and many subsequent ones are based on the temperature dependence of material dielectric functions, which causes spectral mismatch between the peak wavelengths of the emitter and the receiver.[52,53,57] Specifically, Otey *et al*.[52] investigated rectification between 3C-SiC and 6H-SiC half spaces (Fig. 9(a), 9(b)), considering the temperature dependence of the SPhPs supported by SiC. A maximum rectification of $R_{fr} = 0.41$ was obtained for gaps from ~10 nm to ~200 nm, with the high and low temperatures being $T_h = 600$ K and $T_l = 300$ K, respectively.[52] Recent computational studies of NFRHT between a lightly (10^{18} cm^{-3}) doped-Si film and a heavily (10^{21} cm^{-3}) doped-Si half space have demonstrated that for small gaps (1 nm to 50 nm), rectification ratios greater than 0.5

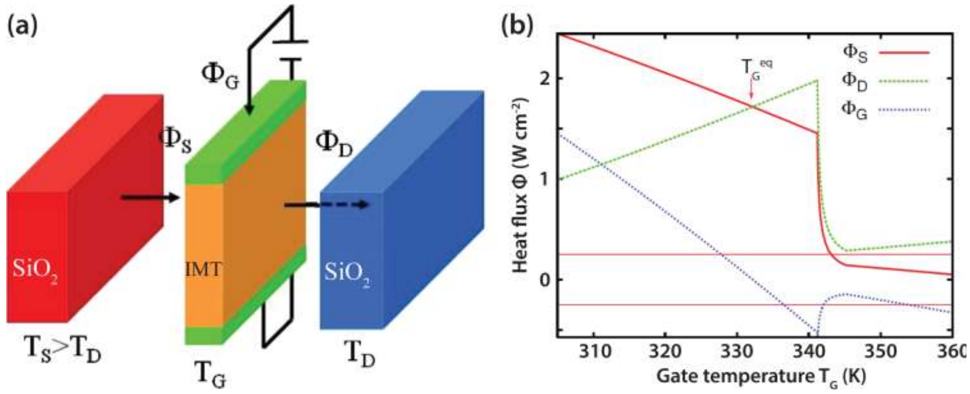

FIG. 10. Concept of a radiation-based thermal transistor.[63] (a) Schematic of a radiative thermal transistor. (b) Heat fluxes Φ_S, Φ_G, and Φ_D to the source, gate and drain, respectively as a function of gate temperature. Changing the flux to the gate allows for thermal switching, modulation, or amplification to be performed.

can be achieved.[53] In this study, the thin film was chosen to take advantage of hybridization of SPPs on the front and back surfaces. In another study by Wang and Zhang,[57] NFRHT between intrinsic Si and doped-Si and between intrinsic Si and SiO_2 (T_h = 1000 K and T_l = 300 K) was studied and rectification ratios of 9.9 and 2.7, respectively, were reported when the gap size was 5 nm. In the same work NFRHT was studied between intrinsic Si and Au and a smaller rectification R_{fr} = 0.8 was obtained (Fig. 9(c)), albeit for a much larger gap size range (10 nm - 500 nm) with T_h = 600 K and T_l = 300 K.

Apart from near-field thermal diodes, far-field rectification schemes have also been proposed.[55,59,61] One such scheme is based on two 1D periodic layered structures each featuring one Fabre-Perot cavity which function as selective emitters with sharp emission peaks.[61] The temperature dependence of the dielectric properties of the Au mirror layers and the highly-doped Si mirror layers is key to the obtained thermal rectification. Specifically, for a T_h = 670 K and T_l = 300 K, a rectification of ~0.23 was reported. One benefit of this design is in its potential for optimization depending on the temperature of the emitter and receiver as the spectral characteristics of the selective emitters can be tuned via suitable choice of the materials and dimensions of parameters of the composing layers. Further, rectification based on MIT materials was also investigated.[55,56] In one case,[55] VO_2 and SiO_2 were used. For far-field radiation, a rectification greater than 0.7 was obtained with emitter and receiver temperatures near the critical temperature T_C of VO_2. In another case (Fig. 9(d)), NFRHT between VO_2 and a second MIT material, $La_{0.7}Ca_{0.15}Sr_{0.15}MnO_3$ (LCSMO, T_C = ~301 K), was exploited and a rectification ratio of 7.7 was obtained at a gap of 10 nm, with T_h = 80 K and T_l = 26 K.[56]

Finally, ultrahigh-contrast and large-bandwidth thermal rectification between a large and a small nanosphere was suggested, exploiting the scale invariance properties of the resonance modes of the spheres, which result in a large difference in the coupling constants between relevant modes in the forward and reverse scenarios.[58] Rectification ratios greater than 10 were reported for two 3C-SiC nanospheres (Figs. 9(e)-9(f)).

6. *Thermal transistors and passive amplification of heat flow*

Thermal transistors were also computationally proposed and were suggested to control the flow of heat in a fashion analogous to electronic transistors. Ben-Abdallah and Biehs[63] proposed a three-body system (Fig. 10(a)) that can function as a radiative thermal transistor based on the MIT of VO_2. In their proposal a VO_2 nanofilm is sandwiched by two SiO_2 plates, one SiO_2 plate serves as the source terminal of the transistor and is held at 360 K, which is 20 K above the critical temperature of VO_2, while the other one is held at room temperature (300 K) and serves as the drain terminal. The VO_2 film serves as the gate. Figure 10(b) shows various heat flows in the system as a function of the gate temperature T_G. As can be seen, the heat flux out of the source and into the drain drops dramatically as the temperature of the gate film increases beyond T_C, which leads to an insulator-to-metal phase transition. The reason lies in the reduced coupling between a metal (metallic phase) and dielectrics (SiO_2), as compared to between two dielectrics (insulating phase and SiO_2). By varying T_G such that it crosses the critical temperature, it was suggested that one can effectively switch the heat flow on or off between the source and drain. Further, by modulating the external heat supply (say using Joule heating) to the gate by a small amplitude, one can modulate the source and drain heat flow by an order of magnitude if operated around T_C. An amplification factor of ~4, as defined by the relative change of drain current to gate current, was obtained using an effective medium theory to account for the effective dielectric function of the gate film around the transition temperature, when both metallic and insulating phases are present.[230]

Apart from active amplification of heat flow, passive measures by insertion of a third film in a parallel-plate system has also been discussed.[62] It was shown that the insertion of a thin film in the middle can induce an effective heat flow between two plates separated by a gap of $2d$ higher than the heat flow between the same two plates separated by d without the film.

7. Thermal memory devices

Thermal memory devices are essential for the construction of the thermal analog of an electronic computer.[228] The two states in a thermal memory device operating between a hot and a cold thermal reservoir (as compared to a high and low electric potential) are defined by two distinct equilibrium temperatures corresponding to vanishing heat fluxes within the device.[228] Although phononic thermal memory designs were introduced a few years ago, photonic memory devices based on thermal radiation have only recently been proposed.[64,65] In all cases negative differential thermal conductance (NDTC)[231] was found to be a necessary mechanism for creating thermal memory devices. While the second necessary component is the existence of bistability, which is only present in many-body systems.

The design proposed by Kubytskyi *et al.*[65] for thermal memory takes advantage of the MIT of VO_2 and can be created by just utilizing far-field radiative effects, although taking advantage of near-field effects can improve the time constants. Specifically, the proposed design (Fig. 11(a)) consists of a SiO_2 film (blue color) radiatively coupled to a low temperature (T_L) thermal bath, located to the left of the SiO_2 film, and a VO_2 film coupled to a high temperature (T_R) reservoir located to the right of the VO_2 film, while the two films are separated by a vacuum gap. Given a set of (T_L, T_R), the "equilibrium state" of the system is represented by a set of film temperatures (T_1, T_2) at which the net heat currents into each film vanish (Fig. 11(b)). Here, NDTC is enabled by the VO_2 film, which behaves like a mirror to infrared radiation in its high temperature metallic state, while offering high transmission in its low temperature dielectric state. The trajectory of temperatures shown in Fig. 11(b) illustrates how (T_1, T_2) evolve from random initial states and finally settle down in one of the two equilibrium states represented by the green dots. The blue dashed line represents the condition for the heat flow into SiO_2 to be 0, while the solid red line nulls heat flow into the VO_2 film. When the state with lower T_2 is defined as 0, the action of writing 1 is performed by inputting heat into the VO_2 membrane so it transits into the metallic state, lowering T_1 by reducing the effect of T_R on the SiO_2 film. Information will be stored as long as the thermal reservoirs remain active. To go from state 1 to state 0, the VO_2 film needs to be cooled down to its insulating phase using Peltier cooling, which subsequently increases coupling between the SiO_2 film and the hot reservoir, making T_1 higher. To read the information, proper thermometers should be used to measure the temperatures (T_1, T_2). The time constant of the writing operations is predicted to be on the order of a few seconds (Fig. 11(c)). It is expected that the operation speed can be greatly increased if the device is operated with a small gap permitting NFRHT. The operation temperance is ~60 K above room temperature.

The design of Elzouka *et al.*[64] exploits the effect of thermal expansion and the nonlinearity of NFRHT. The thermal expansion/contraction of a part is used to increase/decrease the near-field heat current from the hot reservoir to the head (Fig. 11(d)). The origin of NDTC lies in two competing factors affecting the near-field heat flow from the hot reservoir to the head (Fig. 11(e)). A higher T_{head} lowers the radiative heat flow by reducing temperature difference, however, the distance to the

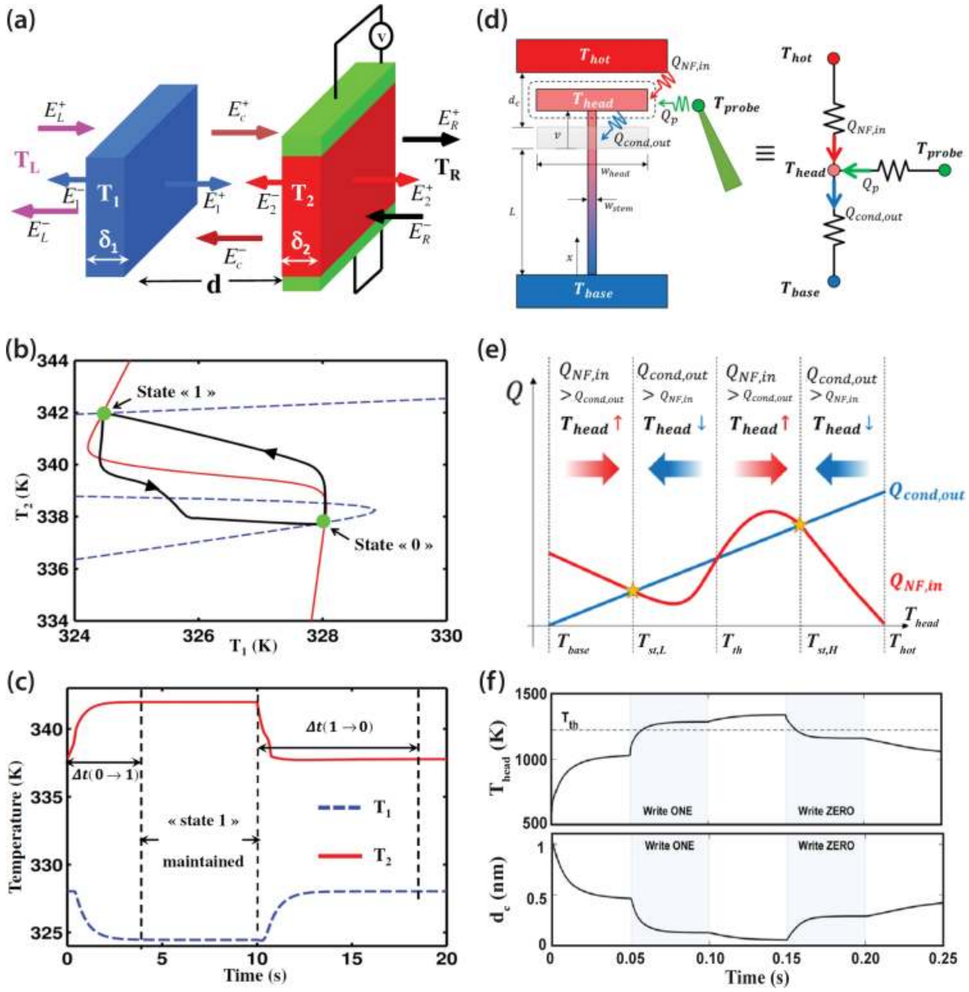

FIG. 11. Radiative thermal memory devices. (a)-(c) A design based on MIT materials.[65] (a) Schematic of the device. (b) Illustration of the bistability of the device as a function of T_1 and T_2, and transitions from one stable state to the other. (c) Evolution of T_1 and T_2 with time during the writing process of the proposed thermal memory device. (d)-(f) A design based on thermal expansion.[64] (d) Schematic of the proposed device along with its thermal circuit analogue. (e) Plot of the near-field radiative heat flow into the head $Q_{NF,in}$ and the conduction loss from the head $Q_{cond,out}$ during operation. The bistability and the two stable states are shown. (e) Plot of head temperature and head-terminal separation with time during the writing process of the device.

hot reservoir is simultaneously reduced. As a result, with proper choice of material parameters, it was suggested that two equilibrium states can be achieved with the reducing radiative heat flow cancelling out the increasing conduction heat flow. The action of writing is performed by heating or cooling a probe, which is thermally coupled to the head. This is conceptually similar to the previous design. All the terminals involved are chosen to be Si and the temperature of the hot reservoir was assumed to be 1440 K, while the time constant was estimated to be ~0.1 s for the chosen dimensions (Fig. 11(f)).

8. Potential of near-field thermal radiation in energy conversion and other applications

A variety of near-field thermal radiation based devices for energy conversion have been proposed by many researchers.[66–82] For example, Park *et al.*[69] have suggested that near-field radiation could be employed to enhance the power output of thermophotovoltaic (TPV) devices. Recent computational studies have also discussed the possibility of using graphene based near-field thermophotovoltaic (NTPV) devices to achieve extremely large efficiencies. We note that while advances[75] in TPV devices (Fig. 12(a)) have demonstrated the feasibility of using nanostructured surfaces for improved

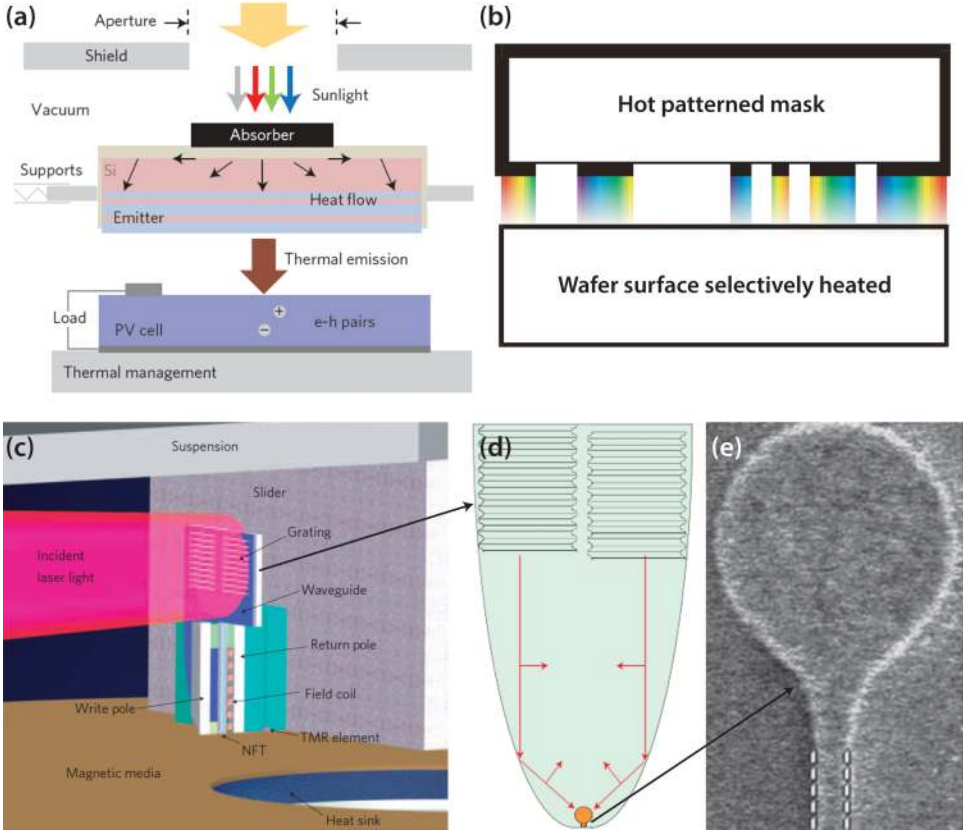

FIG. 12. Selected examples of potential applications for NFRHT. (a) Schematic of a far-field TPV device using solar energy as heat input and multilayer photonic crystal emitter for energy conversion.[75] (b) Schematic of a proposed lithography process based on near-field radiation.[18] (c) Schematic depicting heat-assisted magnetic recording using a parabolic grating coupler to direct laser energy onto a "lollipop" plasmonic near-field transducer.[41] (d) Detailed view of the parabolic grating coupler. (e) SEM image of the near-field transducer. The width between the white dashed lines is 50 nm.

thermophotovoltaic energy conversion, to date there has not been any experimental demonstration of a highly-efficient NTPV device despite the many appealing computational proposals. Apart from thermophotovoltaic energy conversion, Yang *et al.*[79] have computationally explored the potential of a thermoelectric device where the hot side of the device is coupled to a hot thermal reservoir across a vacuum gap via near-field thermal radiation. The authors suggested that in such a device it is possible to establish a higher non-equilibrium temperature for the electrons than for the phonons thus effectively attenuating the deleterious contributions of phonons to thermoelectric performance. The effect of NFRHT on thermionic energy conversion devices was also discussed.[81,82] In addition to the possibility of creating novel energy conversion devices, Pendry[18] has suggested that near-field radiation could potentially be employed for achieving high-resolution thermal lithography (Fig. 12(b)). Finally, it also seems that understanding NFRHT, especially in the 1-10 nm gap regime, may be important for optimizing the performance of heat-assisted magnetic recording (HAMR) technologies[40–42] where a plasmonic antenna (which localizes the electric fields) is used to heat a magnetic recording medium (Fig. 12(c)-12(e))[41] so as to lower the magnetic coercivities in localized regions. In these devices, it is expected that NFRHT can play an important role in the steady-state temperature achieved in the magnetic medium and hence understanding NFRHT could help optimize the performance of HAMR technologies.

IV. EXPERIMENTS

In comparison to the considerable number of theoretical and computational studies, experimental studies on near-field thermal radiation are rather limited in number due to a variety of challenges.

Here, we review the experimental techniques currently available for NFRHT studies and describe their strengths and limitations. We first note that almost all the theoretical calculations available for near-field radiative transport focus on the parallel-plate configuration, and in almost all cases dramatic effects arise only at nanoscale gaps. However, this is one of the most difficult geometries to experimentally realize because it is extremely hard to achieve and maintain good parallelism between macroscopic plates at nanometer separations. Therefore, to date all the quantitative measurements[97,98,232–235] of near-field heat transfer between parallel plates have been limited to micrometer-sized gaps, including recent measurements of NFRHT between sapphire plates published within the last few years.[232] Some of the challenges in performing near-field measurements can be circumvented by use of the tip-plate and sphere-plate configurations. The latter configuration has in particular been extensively leveraged lately for performing a variety of quantitative NFRHT studies. Below, we provide a brief summary of these experimental efforts.

A. Plate-plate

The first plate-plate measurements were, to our knowledge, reported by Cravalho, Domoto and Tien in an AIAA conference[96] and in a subsequent paper.[98] Their apparatus consisted of two parallel copper disks with a diameter of 85 mm that were located in an ultra-high vacuum chamber (10^{-12} torr), which was cooled to ~4.2 K by complete immersion in a bath of liquid helium (see Fig. 13(a)). The top disk serves as a radiative emitter with its temperature raised by a few Kelvin via Joule heating by attached carbon resistors. The radiative heat currents received by the bottom disk (receiver) were estimated by measuring the increase of the receiver's temperature. The spatial separation between the disks was changed from as large as 2 mm to as small as 10 µm by displacing the emitter disk using an external micrometer adjuster. Mechanical contact between the disks was detected by monitoring the electrical conductance between the disks. However, a controlled approach for tuning the parallelism or quantitatively estimating it seems to be lacking. Their experimental data (Fig. 13(b)) showed "definite gap-size dependence of radiative transfer" with as large as a factor of five increase in radiative heat flow at small gaps (~10 µm). The overall enhancement in the measured heat flow was an order of magnitude larger than what they computationally predicted by accounting for wave interference and tunneling.[87] They attributed this discrepancy to the deviation from parallelism and to uncertainties in both the surface conditions of the copper disks in the experiments and in the optical properties used in their calculations.

A similar experiment with copper disks (107 mm diameter) was also carried out later by Kutateladze, Rubtsov and Baltsevich[100] where the spatial separation between the disks was varied from ~250 µm to ~10 µm and a range of temperature differentials and absolute temperatures were investigated at about 2×10^{-7} torr. These measurements confirmed the strong distance dependence of NFRHT in all cases, demonstrating a five-fold enhancement at small gaps, although no comparison with theory was provided. Their results also showed that the threshold gap size beyond which heat transfer enhancements are observed is $\sim 3\lambda_{BB,\max}$, where the peak wavelength was estimated from Wien's displacement law and the known temperature of the emitter.

The first plate-plate NFRHT studies at room temperature were reported by Hargreaves in 1969.[97] The experimental setup as reported in his thesis[99] features a chamber, which is pumped to about 10^{-5} torr (see Fig. 13(c)), and can be immersed in liquid baths of different temperatures. In this setup both the macroscopic emitter and receiver plates (25 mm diameter) were each supported by three independent piezoelectric ceramic tubes, enabling precise tuning of the gap size as well as the parallelism between the plates. The parallelism of the plates was evaluated using both optical interferometry and by measuring the electrical capacitance of three individual capacitors created by three pairs of metallic plates integrated into the emitter and receiver disks (see Fig. 13(d) inset). Specifically, the differences in the three capacitances indicated the level of parallelism, whereas the sum signal served as a measure of the absolute gap size. Mechanical contact between the plates could also be detected by monitoring the electrical conductance between the plates. Chromium was selected as the surface coating (100 nm thick) for both plates as it features a relatively low reflectivity and high hardness, with the former property contributing to higher heat currents and the latter providing robustness against surface damage during the parallelization of the plates, for which inadvertent

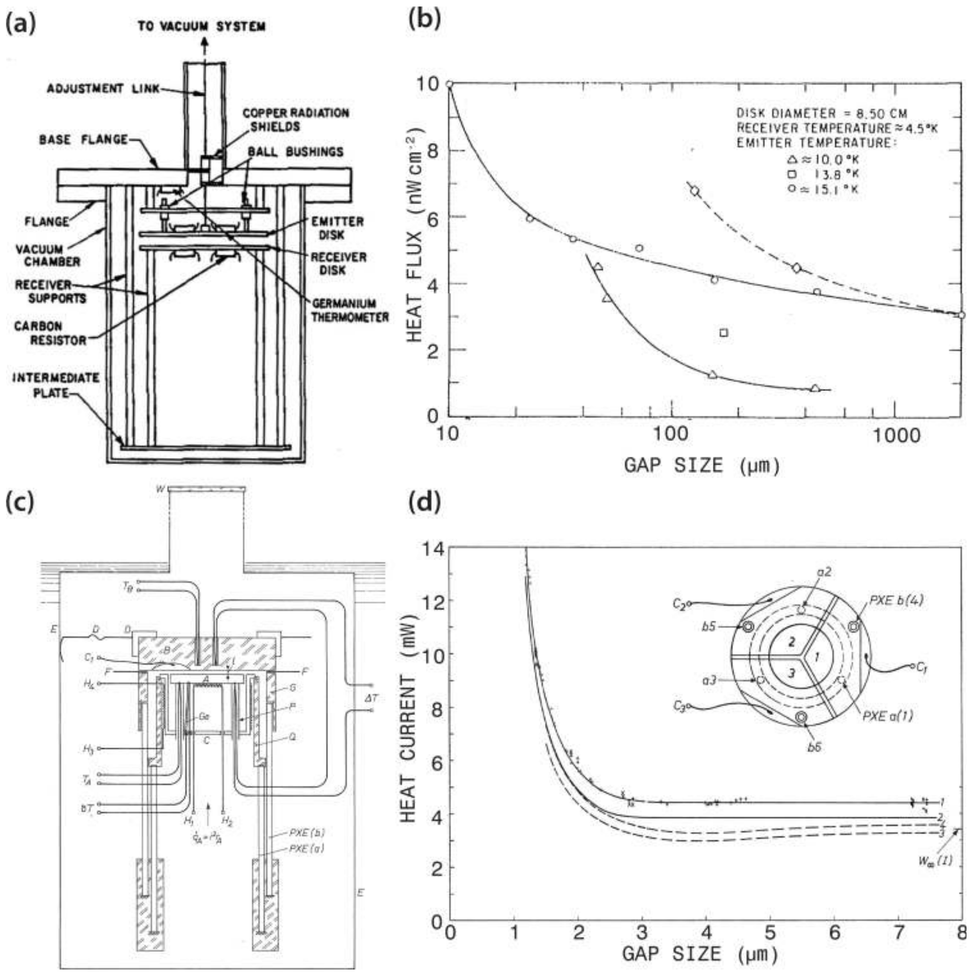

FIG. 13. Early experimental investigations of NFRHT between parallel planes. (a) Schematic of the plate-plate setup used by Cravalho *et al.*[96] (b) Results[98] for radiative heat flux versus the spacing between copper disks using the setup in (a) for temperature differences ΔT of 10.0 K, 13.8 K and 15.1 K. (c) Schematic of the plate-plate setup used by Hargreaves.[99] (d) Results[99] for heat current versus gap size between Cr-coated surfaces near room temperature. Curves (solid lines) have been fit to the experimental data before (1) and after (2) accounting for heat losses. Theoretical curves calculated using Drude model values from the literature[90] (3) and empirically fitted values (4) are also shown. Inset: Schematic top view of the pyrex disk with its three sectors of evaporated Cr. The entire surface serves as the receiver, while the three sectors form three independent capacitors with the Cr coating on the emitter. Panels (c) and (d) were adapted form the Ph.D. thesis of Hargreaves.[99]

contacts occur. Individual plate temperatures were measured with embedded thermistors, while their difference was measured using copper-constantan thermocouples. With the emitter heated resistively, the radiative heat flow to the receiver was estimated as the additional heat input required to maintain the temperature of the emitter at a constant value as the gap size was varied from ~8 μm - 1 μm.

Preliminary results reported[97] by Hargreaves in 1969 clearly showed a strong distance dependence of radiative heat transfer at room temperature (emitter temperature 323 K and receiver temperature 306 K), with a noticeable increase starting at a gap size of ~2.5 μm (the figure in the original paper mislabeled the range in the x-axis[99]). However, computational results permitting a comparison were only obtained later in 1971 by Polder and van Hove.[90] And despite the broad agreement, the measured heat currents at bigger gaps were a factor of three larger than the predicted value. This discrepancy was attributed to errors in the optical properties of Cr used in the computational analysis, and challenges in making accurate thermal measurements.[99] Hargreaves reported refined measurements (emitter at 313 K and receiver at 295 K) later in his thesis,[99] which showed much better agreement with theory as well as a large enhancement in heat transfer (~4 fold) at the smallest gaps (see Fig. 13(d)). In addition to the room temperature measurements, studies were also performed at low temperatures, for example with the emitter at 160 K and the receiver at 132 K, and larger enhancements were observed. Temperature dependence of the threshold gap size, as well as that of radiative heat transfer at various gap sizes was also discussed. A quantitative comparison of these improved measurements[99] with Polder and van Hove's theory showed that the predicted results were consistently smaller than the measured ones (Fig. 13(d)); nevertheless, the overall agreement was improved. The discrepancy was again largely attributed to the optical properties of the Cr layers.

Following these pioneering measurements no new experimental results on heat flow between closely-spaced parallel planes were published until the early 2000s when the growing field of micro- and nanotechnology necessitated that heat transfer between closely-spaced bodies be better understood. In 2008, Hu *et al.*[233] revisited the topic by measuring NFRHT between parallel glass optical flats (127 mm diameter) which support SPhPs in the mid-infrared as discussed in previous sections. They observed much larger enhancements in radiative heat flow than had been measured between metal surfaces in the past. Hu's experimental platform consisted of a hot glass emitter separated from a room temperature glass receiver located underneath by means of dispersed polystyrene microspheres as spacers. The emitter temperature was elevated to tens of Kelvin above room temperature and controlled to within 1 K using a heating pad attached atop it, while a 1×1 in^2 heat flux meter was placed beneath the receiver so that the radiative heat current could be measured. The vacuum gap ($\sim 6 \times 10^{-5}$ torr) paired with the low thermal conductivity of the polystyrene spacers was expected to ensure that radiative heat transport dominated the total heat flux. Using spheres with a nominal diameter of 1 µm, Hu *et al.* were able to measure heat flow consistent with theoretical predictions for glass plates separated by a 1.6 µm gap. They observed that the heat flow across the micrometer gap is about twice as large as the far-field data recorded at 2 mm separation, and is about 50% larger than the blackbody limit. However, measurement with systematically varied gap size was not possible with this platform.

Subsequently, two different studies[232,235] sought to investigate NFRHT for varying gap size. The first study[232] reported NFRHT between two 50×50 mm^2 sapphire plates near room temperature as a function of vacuum ($\sim 2 \times 10^{-7}$ torr) gap size and temperature difference. The experimental apparatus used in this study is illustrated schematically in Fig. 14(a). In this experiment the gap size and parallelism were measured by monitoring the capacitance of four pairs of copper plates located in the corners of the sapphire plates. The orientation of the emitter as well as the spacing between the plates were controlled via three stepper motors. The temperature of the hot sapphire plate was controlled by a feedback loop, and the cold plate was attached to a thermal bath. The heat flow was estimated by monitoring the electric current and voltage across the heater and computing the power input required to maintain the desired temperature difference. Heat transfer data for temperature differences ranging from 6.8 K to 19 K were reported as a function of gap size (~2 µm - 100 µm), as shown in Fig. 14(b). The threshold gap size beyond which appreciable heat transfer enhancements are observed was ~10 µm. And the total heat transfer coefficients monotonically increased with decreasing gap size, reaching a maximum relative enhancement of about two fold. A fairly good agreement was found between the measured and the theoretically predicted heat transfer coefficients. The measured values were found to be slightly higher than the predictions at smaller gaps while having good agreement at larger gaps. This was attributed to the slight curvature (convexity) of the macroscopic sapphire plates, which were measured using Newton rings to have a deviation from flatness of 170 ± 30 nm across the square sapphire plate. Once this curvature was considered in theoretical predictions (dashed lines in Fig. 14(b)), the agreement with experiments improved.

Another study[235] reported NFRHT between parallel W layers at cryogenic temperatures (receiver temperature at 5 K) as the vacuum ($\sim 10^{-10}$ torr) gap size varies from 1 µm to 500 µm for several temperature differences ($\Delta T = 5$ K – 35 K). Their setup[234] is illustrated in Fig. 14(c). In these experiments, a 35 mm-diameter W emitter was placed in close proximity to a W receiver via a differential screw (resolution 100 µm/rev). Parallelization between the emitter and receiver plate was achieved by bringing the two into contact with each other and then maintained after they were separated using a so-called parallelism equalizer which mechanically locks the orientation of the emitter plate by friction.[234] The receiver was mounted on a heat flux meter, which consists of two temperature sensors separated by a calibrated thermal resistance, so that the heat flow could be

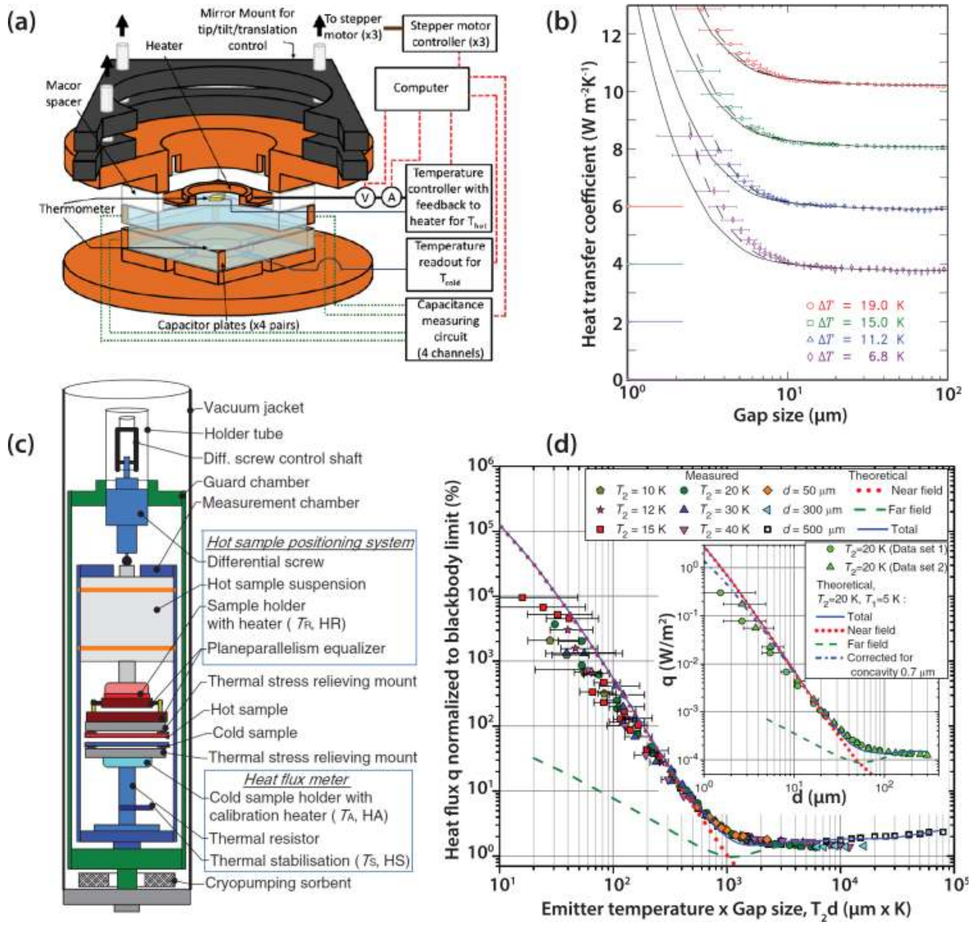

FIG. 14. Recent experimental investigations of NFRHT between parallel planes. (a) Schematic of the experimental apparatus used by Ottens *et al.*[232] to measure NFRHT between sapphire plates. (b) Results[232] for heat transfer coefficient versus vacuum gap size between the sapphire plates for four temperature differences. Each curve is offset by $2\mathrm{W m^{-2} K^{-1}}$ from the last for clarity. Experimental data (points) is plotted alongside theory for planar (solid lines) and slightly curved (dashed lines) surfaces. (c) Schematic of the experimental setup used by Kralik *et al.*[234] (d) Their[235] measured heat flux normalized to the blackbody limit. Theoretical curves were calculated for receiver temperature $T_1 = 5$ K and emitter temperature $T_2 = 20$ K. Open squares represent far field data taken at higher temperatures with a nominally black surface. Inset: Heat flux versus gap size for the experimental conditions indicated in the legend.

estimated. The results from this work[235] are shown in Fig. 14(d), where the measured heat flow is normalized to that expected from blackbodies and is plotted with respect to the product of the emitter temperature and gap size. A threshold gap size of ~50 μm was observed when the emitter temperature was 20 K. The data is seen to agree well with the theoretical prediction except at the smallest gaps for which the measured values are noticeably lower than the theoretical lines. Similar to the sapphire-plate work discussed above, this discrepancy was attributed to the reported concavity of 700 nm across the W plates (see inset of Fig. 14(d) for corrected theoretical prediction). Remarkably, the measured heat flow at a gap size of 2 μm still exceeded that of a blackbody by two orders of magnitude despite the concavity. This factor of 100 represents the largest near-field enhancement observed to date in parallel-plane geometry. As to relative heat flow increase from large to small gaps, about three to four orders of magnitude enhancement was demonstrated.

In addition to experimental schemes featuring independent, macroscopic emitter and receiver plates, several recent studies[236–238] have reported MEMS-based approaches to studying NFRHT between suspended microstructures that are part of a monolithic device. In one group of studies,[236,237] a small gap of fixed size (550 nm[236] and 1 μm[237]) was formed between two nominally parallel SiO_2 membranes (say 200 nm and 400 nm thick, size is ~$80 \times 80\ \mu m^2$)[237] via etching of a sacrificial Al layer in between. The thermal measurement was performed in high vacuum ($\sim 10^{-6}$ torr) by resistively (poly-Si[236] or Pt[237] resistor) heating and monitoring the temperature of the emitter SiO_2 surface, both in the presence of the receiver SiO_2 surface and when it is removed with a microprobe. For the same known electric heating current, the emitter reaches different steady-state temperatures with or without the receiver; and this temperature difference is then used to evaluate the near-field thermal conductance between the two membranes. It was concluded[237] that for a gap size of 1 μm the near-field conductance was ~10 times larger than the blackbody limit when the emitter temperature was within 300 - 400 K. Although no comparison with any near-field calculation was given, the observed enhancement seems to be much higher than available theoretical predictions for bulk materials.[154] Another recent MEMS-enabled experiment[238] explored NFRHT between parallel nanobeams (1.1 μm wide, 500 nm thick, 200 μm long) coated with 100 nm-thick SiO_2. With one beam fixed and the other controlled using electrostatic actuation, they were able to cover nominal vacuum (1.5×10^{-4} torr) gap sizes between 250 nm and 750 nm with a single device. The observed near-field conductance exceeded the blackbody limit as the gap size became smaller than ~600 nm and reached a maximum of ~7 times the limit. This approach could have potential for detailed NFRHT studies if it can be adapted to study NFRHT between parallel planes instead of beams which have relatively small and poorly-defined surfaces. Note that the absolute size of the emitter and receiver could have a large impact on NFRHT considering the dominant role of surface modes and their long wavelength and propagation distance along the surfaces.[116]

As shown above, the experimental investigation of parallel-plane NFRHT boasts a long history of almost half a century and a range of ingenious instrumentation efforts and achievements. Nonetheless, many challenges remain in order to explore and exploit the rich physics in the thermal near-field. All the existing macroscopic approaches have been limited to micrometer gaps due to imperfect parallelism, surface curvature and inevitable particulate contaminations. Taking advantage of the ever maturing microfabrication technology, the MEMS-based studies represent an important experimental advancement especially since they allow the creation of nanoscale gaps and have no need for complex precision positioning and control platform. Nevertheless, the smallest gap size observed still remains in the hundreds of nanometer range; and further improvements are required to evaluate the parallelism, the surface roughness and curvature, as well as to enable measurements between a wider variety of materials/structures and across controllable gap size. At last, we note that the sub- micrometer film thickness could potentially complicate the numerical modeling process especially for larger gaps.

B. Tip-plate

The invention of the scanning tunneling microscope (STM) and atomic force microscope (AFM) by Binnig, Rohrer and colleagues at IBM Zurich in the early 1980s revolutionized the area of nanoscience and nanotechnology. Soon after the first demonstrations of these scanning probe microscopy techniques, Williams and Wickramasinghe,[239] who were also at IBM (T. J. Watson center), presented the scanning thermal profiler (STP) in 1986. Similar to a STM or AFM probe, their scanning probe has a sharp (~100 nm) conical tip which features a tiny thermocouple formed by the junction of two (inner and outer) dissimilar metals. Operated in air, their probe allowed high-resolution (100 nm lateral and 3 nm vertical) surface profiling based on heat currents between the heated tip and the cold sample as compared to electric currents in a STM, eliminating the need for a conductive layer. An increased signal-to-noise ratio was observed as the tip approaches the sample.[239] Dransfeld and Xu[240] noticed that the high vertical resolution of STP implied that the heat currents must be very sensitive to the tip-sample distance. They then offered an alternative explanation for the heat flow between the tip and sample via near-field radiation,[240] as compared to conduction/convection through air. Subsequently, Xu *et al.*,[241,242] developed a platform similar to that used by Williams *et al*.[239] to measure the NFRHT between a scanning probe and a sample in high vacuum ($<10^{-5}$ torr). Specifically, Xu *et al*.[241,242] devised an approach to probe NFRHT between an indium (In) needle and a planar Ag(90%)Cu(10%)-Cr thermocouple ($\sim 160 \times 160$ μm^2). The tip of the relatively soft In needle was made flat and parallel to the planar thermocouple by simply squeezing the tip onto the thermocouple. Despite their creative and careful experimental efforts, their results were inconclusive as the thermocouple lacked the sensitivity to resolve any temperature changes until the tip physically contacted the plate. However, their work inspired the study of NFRHT in the early days by providing a new direction. The configuration of a sharp scanning tip and a planar sample makes it possible to achieve tip-sample spacing of ∼1 nm without having to perform technically challenging alignment procedures, and thus allows researchers to delve orders-of-magnitude deeper into the thermal near-field than has ever been possible in the parallel-plane configuration. Conversely, the very small heat transfer areas associated with sharp tips also result in extremely small heat flows, so very high-resolution calorimetry techniques are required to measure NFRHT in this configuration.

A few years later, Müller-Hirsch *et al.*[243] reported two tip-plate experiments performed in ultra-high vacuum (UHV, ∼10^{-10} torr). The first one (called the STM setup) is schematically similar to that of Xu *et al.*,[242] which involved a metallic probe and a planar thermocouple. While the second experiment (called the SThM setup) involved a SThM (scanning thermal microscope) probe and a planar metallic surface. Both setups used sharp tips as compared to the flat ones used by previous researchers.[241,242] In the STM setup, a planar nickel-gold (Ni-Au, Ni on top) thermocouple with two 200×200 μm^2 junctions was fabricated on a glass substrate. The substrate was cooled to 100 K and a W probe tip at 300 K was brought in close proximity to one of the thermocouple junctions with the other serving as a reference. Tunneling current and thermovoltage were measured simultaneously to monitor gap size and heat flow, respectively. A noticeable temperature increase in the thermocouple was found as the gap size decreased below about 10 nm, indicating increased heat transfer from the room temperature tip to the cold sample. For the SThM setup, the authors fabricated a scanning probe with an integrated thermocouple tip (radius of curvature ∼1 - 2 μm) similar to the one first presented by Williams and Wickramasinghe.[239] To prepare the tip a Ni wire was sharpened, coated with photoresist (PR), exposed to light at the tip to remove the PR, and coated again with Au, resulting in a sharp probe with a Au (30 nm thick) -Ni thermocouple formed at the tip. A sample consisting of 100 nm-thick Au deposited on freshly cleaved mica was cooled to 100 K while the probe remained at about 300 K. The probe was positioned in the near-field of the sample by establishing a tunneling current. The large temperature difference ($\Delta T = 200$ K) between the tip and the sample yielded a detectable tip temperature drop as the gap size was reduced below 10 nm before saturating near 1 nm. However, uncertainty in the thermal resistances of the different components within the experimental apparatuses (in both the STM and SThM setups) prevented these researchers from quantifying the heat flow for a direct comparison with theory.[243]

In 2005, NFRHT between a SThM probe tip and planar surfaces of Au and gallium nitride (GaN) was investigated by the same research group.[244] The experimental setup in this work was functionally similar to that employed by Müller-Hirsch *et al.*,[243] but the design of the probe was somewhat different. The redesigned probe, an illustration of which appears in Fig. 15(a),[245] was fabricated by inserting a Pt/Ir (iridium) wire into a glass micropipette and drawing the pipette until it fractured.[244] The protruding wire was electrochemically etched into a sharp (unspecified size) tip, after which the entire probe was coated with a 25 nm Au film to form a thermocouple at the junction with the Pt/Ir wire. NFRHT was studied by positioning the room temperature tip near a cold substrate (100 K) and measuring the thermovoltage that developed across the thermocouple. The tip temperature change was related to the radiative heat current between the tip and the sample via the thermal resistance (probe resistance R_{th}) between the probe tip and its thermal reservoir. The probe resistance was estimated to be 54000 K/W using independent experiments involving heating of the tip with a laser beam.[244] The authors reported ∼3 orders of magnitude enhancement in heat flow as the gap size between the Au tip and a Au surface was reduced from ∼200 nm to 1 nm, although the measured heat flow was less than the theoretically expected value (estimated by modeling the tip as a point-like dipole) for gap sizes less than 10 nm, as can be seen in Fig. 15(b) (dotted line). The heat flow measurements performed using a GaN substrate were also reported to be qualitatively similar. The authors proposed that non-local effects become important at extremely small gap-sizes for the geometries explored by them. By modelling the spatial dispersion of the material dielectric functions, they reported a better agreement in the trend between experiment and their dipole calculation (Fig. 15(b), solid line).

Further, researchers were able to use the SThM probe to perform non-contact thermal microscopy in UHV.[38,39] Specifically, operating in the constant current STM mode, Kittel *et al.*[38] scanned a room temperature SThM probe (tip radius ∼50 nm, Fig. 15(c)[245]) over a cooled (100 K) Au substrate while simultaneously recording the tip thermovoltage. A comparison between the STM topography

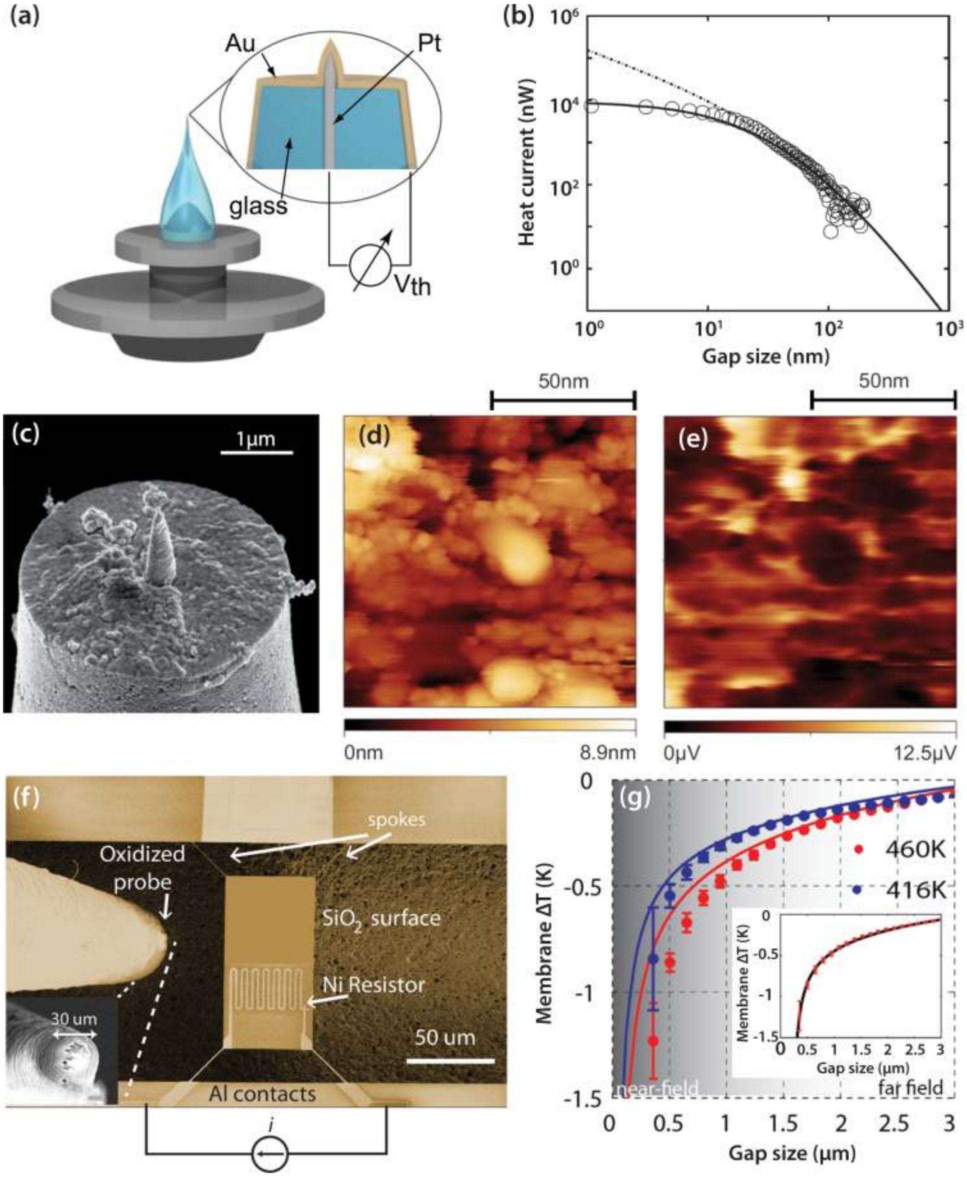

FIG. 15. Measurement of NFRHT between a tip and a planar sample. (a) Illustration of the SThM probe used by Worbes *et al*.[245] (b) Heat current versus gap size for Au tip and sample,[244] including measured data (open circles), modelling result with local (dashed line) and non-local (solid line) dielectric response. (c) SEM image of the tip.[245] (d) Image of a Au surface obtained via STM.[38] (e) Thermal image of the same Au surface.[38] (f) SEM images of the suspended SiO_2 membrane and the SiO_2-coated probe used by Guha *et al*.[246] (g) Membrane temperature drop versus tip-plane distance for two initial temperatures: experimental data (dots) and theoretical curves (lines). Inset: Shifting the data by 160 nm improves agreement between theory and experiment.

(Fig. 15(d)) and the thermovoltage (Fig. 15(e)) images reveal that this thermal microscopy technique does indeed give information about the topography of the surface. Moreover, by modeling the tip as a spherical dipole they were able to show that the thermovoltage map (Fig. 15(d)) agrees qualitatively well with the calculated electromagnetic LDOS above the Au sample using a perturbative approach. However, the authors expressed some concerns including the use of a dipole approximation for calculations across a gap size smaller than the tip dimension.[38]

More recently, the same group performed some experiments[245] in which NFRHT between a tip (Fig. 15(c)) and a dielectric monolayer of salt (NaCl) deposited on an atomically flat Au substrate was investigated. Significant near-field heat transfer enhancement was observed only when the gap size was smaller than ~6 nm. No probe resistance was explicitly reported so no heat flow was quantified. In terms of tip temperature change, the NFRHT between the Au tip and the monolayer NaCl was measured to be about twice as large as that between the Au tip and Au sample. By using another Cr-coated probe, they checked the material dependence of the measurement and again observed a larger enhancement when the tip is over the NaCl monolayer. The absolute temperature change for the Cr tip in the presence of the NaCl was about 6 times larger than the Au tip. A theoretical explanation of these results remained elusive and the authors suggested that that current theories based on FE may be inadequate to describe the observed phenomena in extremely small gap sizes (1 nm - 10 nm).

A recent tip-plate NFRHT measurement[246] reported heat flow from a planar heated island to a probe. The experimental setup in this work (Fig. 15(f)) was quite different from previous investigations. The probe had a microscale tip made by coating a 30 µm diameter W probe with 2 µm-thick SiO_2 and was maintained at room temperature during the experiment. While the sample was a MEMS device featuring a 840 nm-thick SiO_2 membrane ($100 \times 50\ \mu m^2$) suspended over a cavity by 600 nm wide, 30 µm long beams. A 2 kΩ Ni resistor was deposited onto the membrane to serve both as a resistive thermometer and a heater capable of heating the membrane to 460 K. When the probe was brought into close proximity to the heated membrane, the membrane temperature decreased as quantified by measuring the resistance change of the thermometer. Measured data of the membrane temperature (Fig. 15(g)) agreed fairly well with the theoretical expectation. A horizontal offset of 160 nm in the data could bring the experiment and theory into better agreement (Fig. 15(g), inset) and was attributed to the gap size uncertainty. The minimum gap size in this experiment was limited to ~300 nm due to the probe's large radius of curvature, leaving the sub-100 nm range unexplored.

From the above descriptions it is clear that the tip-plate experimental setup, as compared to the plate-plate configuration, offers significant potential in the study and utilization of NFRHT, especially in the extreme near-field with gap sizes around or below 10 nm. However, further work is required to achieve a better understanding of the reported experimental observations and to validate/invalidate the current theories in modeling NFRHT in gap sizes as small as a few nanometers. At last, the NFRHT between dielectric materials in the extreme near-field remains unexplored as the SThM-based technique is inevitably limited to electrically conductive materials.

C. Thermal near-field spectroscopy

Near-field heat transfer measurements provide insight into the integral effect of the near-field on radiative heat flow. However, heat flow measurements alone cannot lead to direct characterization of the surface modes or the spectral properties of the evanescent field in general. The ability to experimentally probe the spectral nature of thermal radiation in the near-field is critical to understanding and tuning the near-field radiative properties. Such investigations require different experimental techniques than those described previously.

One of the first techniques that enabled probing the thermal near-field was reported by De Wilde *et al.*[37] In this work, the authors described a "thermal radiation scanning tunneling microscope" (TRSTM) that enabled high-resolution imaging of surfaces by using the near-field thermal radiation as an intrinsic source of illumination. The name of the setup emphasizes its analogy to a STM: while a STM measures the electronic LDOS, a TRSTM characterizes the electromagnetic LDOS. The authors placed a sharp W tip in close proximity to the sample of interest (Fig. 16(a)[247]). When the tip was lowered to within several hundred nanometers from the sample (Au patterned on SiC), the evanescent electromagnetic field normally confined near the sample surface was scattered into the far-field. The scattered radiation was then collected using a Cassegrain-type objective and focused onto a low-bandgap mercury-cadmium-telluride (HgCdTe, or MCT) detector with a spectral range of 6.5 µm - 11.5 µm. A heater positioned beneath the sample enabled raising its temperature by up to ~440 K, resulting in increased intensity of the LDOS which is then encoded in the TRSTM signal. In order to increase the signal-to-noise ratio, the tip was modulated vertically at a frequency of Ω_{tip} (unspecified) around an average distance and the collected signal was later demodulated at Ω_{tip} or $2\Omega_{tip}$. The authors noted a key difference between these two demodulation frequencies, with the Ω_{tip} signal characterizing the averaged LDOS over a larger vertical distance while the $2\Omega_{tip}$ signal capturing the LDOS at a smaller gap. A series of images obtained by TRSTM are shown in Figs.

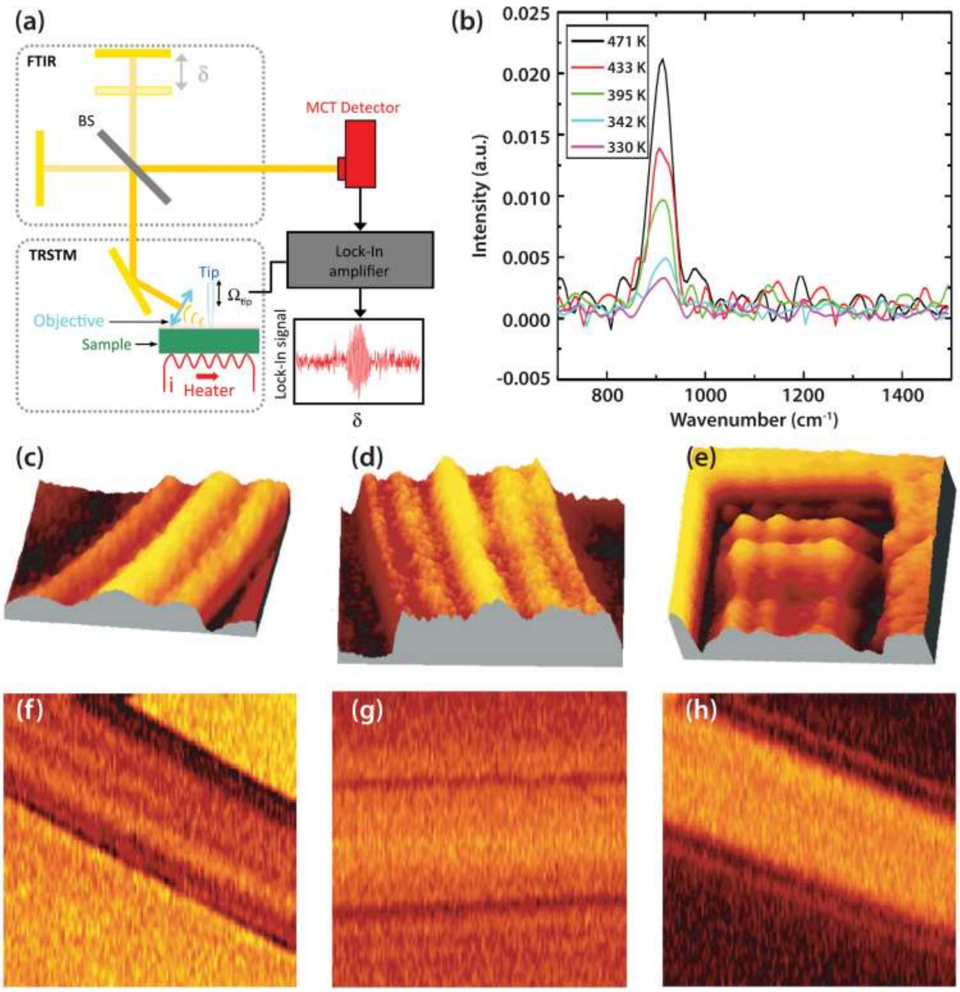

FIG. 16. Experimental demonstration of temporal and spatial coherence of thermal near-field based on TRSTM. (a) Schematic of the TRSTM and FTIR-based near-field spectroscopy setup[247] with heated sample. (b) Measured near-field thermal emission spectra above SiC at various temperatures.[247] (c)-(h) TRSTM images.[37] (c-e) Images of a Au stripe on SiC substrate obtained at an estimated effective tip-sample distance of 3 μm by scanning over a (c) 16 μm wide segment, (d) 25 μm wide segment, and (e) 30 μm wide end of the stripe. (f)-(h) Images of a Au stripe on a SiC substrate measured with an effective distance of 200 nm. (f) Image for which the signal was band-pass filtered at 10.9 μm (1 μm bandwidth). (g) Image filtered at 8 μm. (h) Image differs from (f) only in the use of SiO_2 as substrate.

16(c)-16(h). The first three (Fig. 16(c)-16(e)) were acquired by scanning the tip over a Au stripe (deposited either on a SiC or SiO_2 substrate) and filtering the signal at 10.9 μm (1 μm bandwidth) in order to improve its temporal coherence.[37] With a demodulation frequency of Ω_{tip}, fringe patterns were observed along the direction of the stripe (Fig. 16(c)-16(d)), with the number of fringes being dependent on the stripe width (10 - 30 μm). A more complicated interference pattern was observed at the end of the stripe (Fig. 16(e)) due to the altered boundary condition. These cavity fringes were in good agreement with calculations of the LDOS 3 μm above the Au stripe. Attributed to the SPPs on Au, they were considered to be the first direct evidence of long decay length, spatially coherent thermal radiation in the near-field.[37] Further, the bright and dark portions of Figs. 16(f)-16(h) (demodulated at $2\Omega_{tip}$ to detect the LDOS at ∼200 nm distance to the sample) demonstrate the temporal coherence of the thermal emission over the SiC substrate. When an 18 μm wide Au stripe patterned on a SiC substrate was imaged with a 10.9 μm band-pass filter (band size 1 μm), the SiC substrate appeared bright and the stripe appeared dark (Fig. 16(f)). This is expected because theory predicts that SiC supports SPhPs with a wavelength of 10.6 μm (∼117 meV, Fig. 16(b)). Changing the band-pass filter to 8 μm (Fig. 16(g)) or imaging the Au stripe on a SiO_2 substrate with the same 10.9 μm filter

(Fig. 16(h)) both attenuated the bright signal originally observed from the SiC substrate, suggesting that the contribution to the signal is primarily from the signature SPhPs of SiC. These images thus appear to demonstrate a direct observation of SPhPs on the surface of SiC.

The technique described above represents a pioneering first step in the characterization of thermal near-field and the use of it for nanoscale imaging. However, a complete spectroscopic study of near-field thermal radiation was not possible. In order to enable such characterization, Babuty *et al.*[247] recently combined a Fourier transform infrared spectrometer (FTIR) with the previously mentioned TRSTM setup (Fig. 16(a)). A modulated W tip which hits the sample intermittently is used to scatter the thermal near-field into the far field. With a modulation frequency of Ω_{tip} = ∼32 Hz and an amplitude of ∼100 nm, the near-field spectra of SiC (Fig. 16(b), demodulation at Ω_{tip}) and SiO_2 were measured with a resolution of 6 cm^{-1} and resonant peaks were observed near 913 cm^{-1} and 1110 cm^{-1}, respectively. No peaks were found when the tip was retracted to ∼1 µm above the sample. This is again direct experimental demonstration of the temporal coherence due to surface electromagnetic modes (see also Fig. 7(c)). Comparing to the theoretically predicted values of 948 cm^{-1} and 1156 cm^{-1}, there is a redshift of ∼40 cm^{-1}. Both resonances were also observed to be broader than expected.

However, we note that a similar spectroscopic technique referred to as the thermal infrared near-field spectroscopy (TINS, Fig. 17(a)) was presented by Jones, Raschke and coworkers[248,249] before the work of Babuty *et al.*[247] In TINS, the thermal near-field is also coupled into the far-field by the sharp tip (Si, tip radius measured to be ∼50 nm, see Fig. 17(c)-17(f)[249]) of a scanning (AFM) probe, which is then collected by an off-axis parabolic mirror and subsequently analyzed with a FTIR spectrometer (see Fig. 17(b) for the raw and filtered interferograms). However, an important difference from the TRSTM setup is that in TINS the probe tip is heated (resistively, Fig. 17(c)) instead of using a heated sample. Consequently, the tip serves not just as a scatter of the sample near-field, but also a heater (with a temperature up to ∼700 K) to locally heat the sample to ∼550 K via ballistic conduction through air molecules. In order to improve the sensitivity of this technique, the authors oscillated the AFM probe close to its resonance frequency, enabling the use of a lock-in detection scheme. The near-field of various substrate materials (SiC, SiO_2, and PTFE) were investigated. With a spectral resolution of 25 - 11 cm^{-1}, the TINS spectrum for the SiC sample (Fig. 17(g)) exhibits a strong but broadened resonance near 950 cm^{-1}, the region in which SiC is expected to support SPhPs.[249] Further, redshifts of 5 - 50 cm^{-1} were observed using different probes.

The consistent observations of redshifts[247–251] of the resonant peaks in the measured near-field spectra as compared to the calculated spectral energy density represent a recent topic of concern. Various models have been proposed by the aforementioned research groups. It was suggested that multiple reflections between the sample and tip leads to an effective tip (dipole model) polarizability which can be accounted for with an effective tip radius.[247,250] The disturbance of the sample near-field by the tip was also considered, which was modelled by surrounding the sample with an effective medium whose dielectric function differs from that in air.[249] Further, the contribution of phonon softening in the sample was discussed.[248,249]

Apart from TRSTM and TINS which uses heated samples or tips as intrinsic illumination sources, the scattering scanning near-field optical microscopy (s-SNOM) was also used to study the near-field. In order to do so, Zhang *et al.*[252] used an external infrared source to illuminate the system. The authors studied the sample thickness-dependence of the LDOS by measuring with a Si tip over a set of amorphous SiO_2 thin films (thickness 2 - 300 nm) thermally grown on Si. They observed a clear maximum in the spectroscopic signal at 1130 cm^{-1}, which is red shifted by about 20 cm^{-1} from the expected resonance for SiO_2. Further, the amplitude of the maximum noticeably decreased for thinner films. A theoretical calculation modeling the tip as a spherical dipole failed to describe the experimental results accurately. A more robust spheroid model capable of describing the antenna effect better described the data, capturing both the red shifted resonance and the amplitude changes for different film thicknesses.

D. Sphere-plate

Studying NFRHT between a sphere and a plane represents a compromise between the parallel-plane and tip-plane geometries. The sphere-plane geometry permits relatively larger heat flows

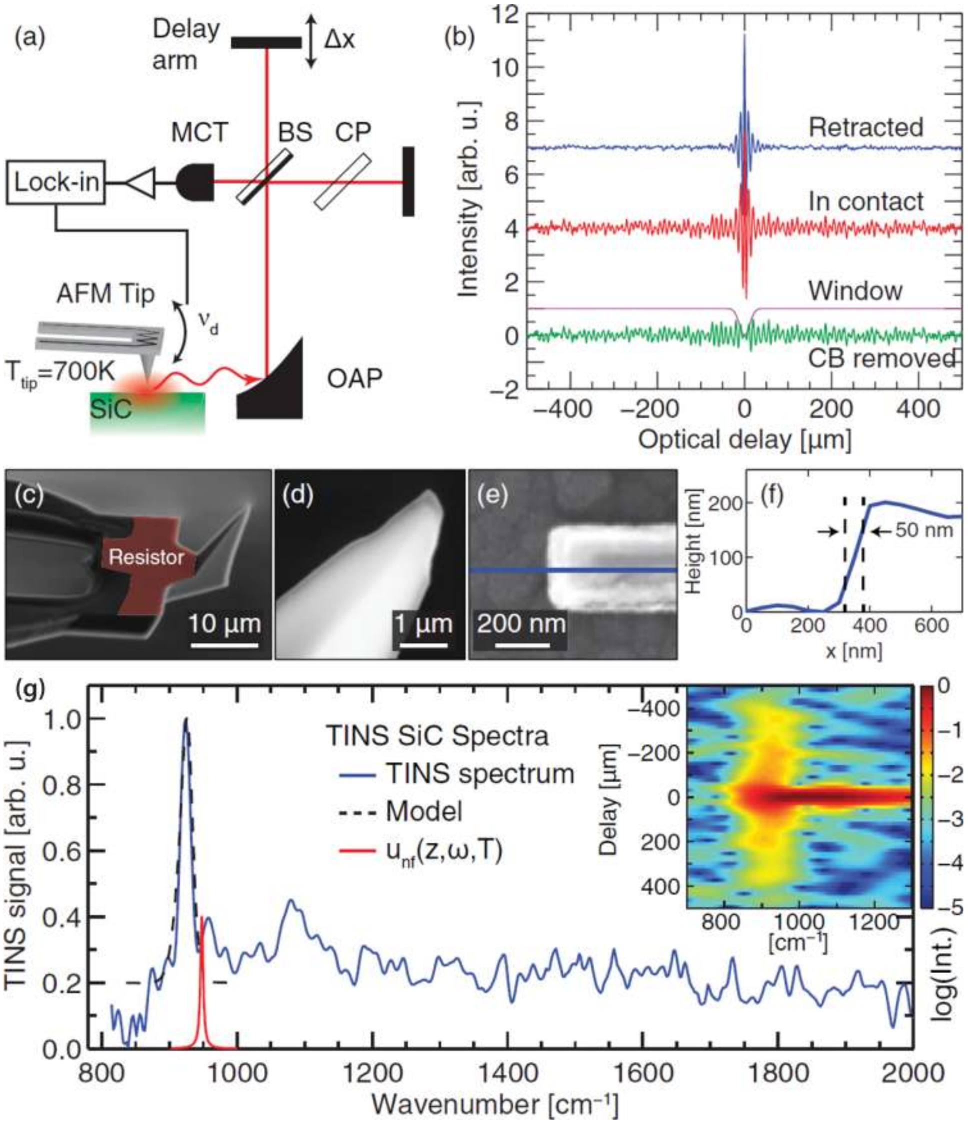

FIG. 17. Characterization of temporal coherence of thermal near-field using TINS.[249] (a) Schematic of TINS setup featuring heated tip. (b) Interferograms with tip retracted and tip in contact with SiC, and with the center burst removed by a window function. Long-range interference in contact indicates coherent contribution due to the SPhP resonance. (c)-(d) SEM images of the Si cantilever and tip. (e) AFM image of a test structure and a line profile (blue) shown in (f) indicating the tip radius is ∼50 nm. (g) Fourier transformed TINS spectra of SiC (solid blue). Fits (dashed black) using finite dipole model. Calculated spectral energy density (solid red, arbitrary unit). Inset:Spectrogram of the in-contact interferogram in (b).

than those associated with the tip-plane configuration because of the increased heat transfer area. Further, the use of even modestly large spheres (diameter ∼1 µm) enables the use of macroscopic material properties (e.g., dielectric function) when making predictions about NFRHT. Unlike the parallel-plane geometry, measurements using the sphere-plane geometry do not require technically challenging alignment and parallelization of the heat transfer surfaces, so smaller gaps (∼10 nm) can be achieved with relative ease. For these reasons, recent experimental work[217,218,223,253–258] exploring some of the more striking predictions of NFRHT theory has focused on the sphere-plane geometry.

1. Bimaterial cantilever-based approaches

An experimental technique for measuring NFRHT between a sphere and a plane was developed in 2008 by Narayanaswamy *et al*.[253] and is illustrated schematically in Fig. 18(a).[218] In this AFM-based

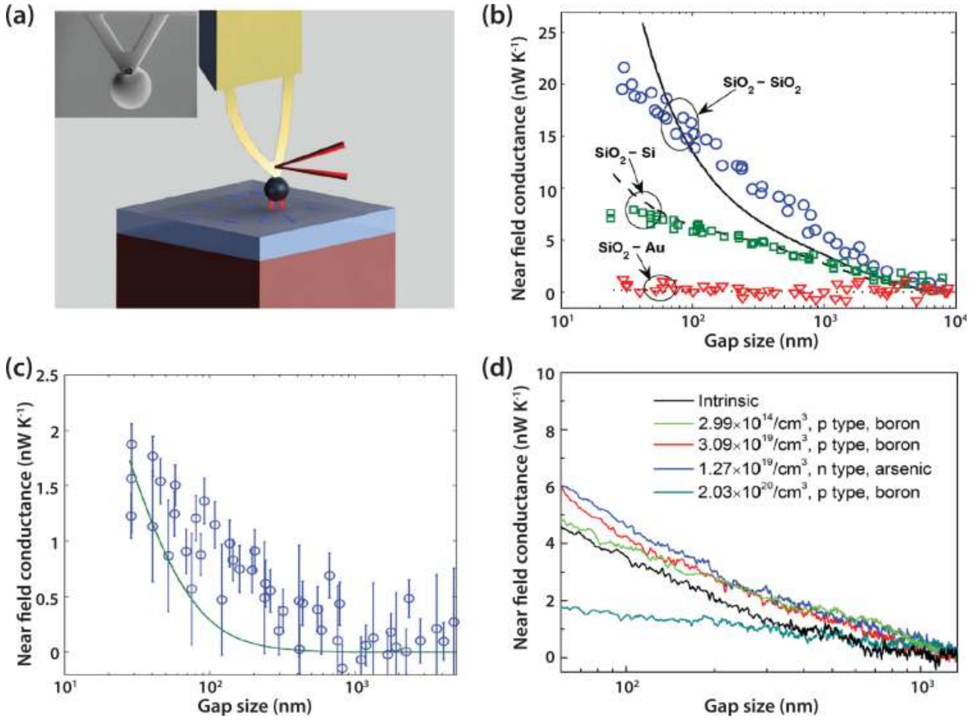

FIG. 18. Measurements of NFRHT between a sphere and a plane using the bimaterial cantilever-based approach. (a) Schematic of the experimental setup.[218] The same principle was used in other works.[253,254,257] (b) Experimental results[218] for near-field vacuum gap thermal conductance versus gap size measured between a 100 μm diameter silica sphere and a glass slide (blue circles), doped Si surface (green squares), and Au surface (red triangles). Theoretical curves produced using DA are represented for SiO_2-SiO_2 (solid line), SiO_2-Si (dashed line), and SiO_2-Au (dotted line). (c) Experimental results[254] for near-field conductance measured between a 50 μm Au-coated silica sphere and a 100 nm-thick Au film. Experimental data (circles) are plotted alongside a theoretical curve (solid line) obtained using DA. (d) Experimental results[257] for near-field conductance measured between a 100 μm glass sphere and Si substrates of various doping types and concentrations.

technique, a SiO_2 microsphere (~50 μm diameter) is glued to the tip of a silicon nitride (SiN_x) -Au bimaterial cantilever, which deflects as its temperature changes because of mismatched coefficients of thermal expansion for the SiN_x and Au layers. A low power laser (few mW) was focused on the cantilever to optically heat the cantilever-sphere assembly so a temperature difference can be established between the sphere and a sample (glass microscope slide). Simultaneously, the reflected laser beam from the cantilever surface was monitored using photo-sensitive diodes (PSD) to measure the deflection of the cantilever arising due to temperature changes and/or mechanical forces. When the warm sphere is brought into close proximity to a planar sample at ambient temperature in a vacuum environment ($\sim 5 \times 10^{-5}$ torr), there is a net radiative transfer of heat from the sphere to the sample, resulting in a temperature drop of the cantilever which in turn reduces the bimaterial deflection. This cantilever deflection as a result of the temperature change is then measured using the PSD. The deflection of the cantilever in response to heat flows was independently calibrated.[253] The near-field thermal conductance was reported for gap sizes from 10 μm down to 100 nm, with all the measured values exceeding predictions by the Derjaguin approximation (DA). The authors proposed that for DA to be valid, the near-field contribution has to dominate over that of the far-field which they estimated was true only when the diameter of the sphere is less than ~2 μm, while the sphere they used was much larger in size.[253] In these experiments the gap size was reduced by bringing the substrate towards the sphere in a stepwise fashion with a smallest step size of 100 nm, which represents a limit for the smallest gap size and the gap size uncertainty. The gap size was measured by referencing the displacement of the substrate to the location where the sphere and the substrate make contact, which was indicated by a sudden change in the PSD signal.[253]

Later Shen, Narayanaswamy, and Chen[218] leveraged the same approach to systematically explore the role of SPhPs in mediating the enhanced heat transfer in dielectrics. In these experiments they report a high-resolution (~5 nm) piezoelectric control of the sample position (thus the gap) and presented near-field heat transfer data in a sphere-plane configuration for gap sizes as small as 30 nm. From these NFRHT experiments they inferred (in terms of equivalent heat transfer coefficient based on the DA approach) enhancements as large as three orders of magnitude as compared to estimates using far-field radiation theory for blackbodies. Specifically, they reported NFRHT measurements between a SiO_2 sphere (50 or 100 μm diameter) and planar surfaces. The planar samples include a glass (nominally SiO_2) slide, a Si (2.6×10^{19} cm^{-3} arsenic-doped) wafer, and Au (1 μm-thick gold on glass slide). The roughness of all three samples was reported to be ~3 – 4 nm. Their results for a 100 μm diameter sphere are shown in Fig. 18(b). As expected from previous discussions, the near-field conductance between the SiO_2 spheres and the planar SiO_2 substrate is the larger than for all other configurations due to the presence of SPhPs supported by SiO_2. Similar to their previous work, the measured gap-dependence of the near-field conductance does not agree with the DA prediction, which is smaller for gaps over 100 nm but exceeds the measured values for the smallest (tens of nanometers) gaps. The authors again noted that DA may not be always valid. Some near-field enhancement was also observed between the SiO_2 sphere and the Si sample, and the data appears to agree well with the proximity approximation except for gap sizes smaller than ~50 nm. No measurable enhancements in heat transfer between the SiO_2 sphere and the Au plane were observed, which is consistent with theory due to the large mismatch in the near-field spectra of these materials. The gap size was again measured as described above. At last we note that the authors performed a control experiment with very weak laser beam (<1 K temperature difference between the sphere and sample) to determine the effect of proximity forces on the cantilever deflection. More recently, Shen *et al.*[254] explored NFRHT between gold-coated sphere and substrates and the measured results (Fig. 18(c)) compared well with the modified Derjaguin approximation proposed by Sasihithlu and Narayanaswamy.[180] Also, Shi *et al.*[257] demonstrated that the near-field conductance between a SiO_2 sphere and doped Si substrates of different doping types (boron and arsenic) and levels (10^{14} to 10^{20} cm^{-3}) can vary from 2 nW/K to 6 nW/K at a gap of ~60 nm (Fig. 18(d)).

Apart from the above sphere-plate experiments performed in the USA, similar work were conducted in France. In 2009, Rousseau *et al.*[217] performed an experiment between a SiO_2 microsphere (sodalime glass) and a heated SiO_2 (borosilicate) substrate. Their technique is outlined schematically in Fig. 19(a) and differed from that of Shen *et al.*[218] in two important ways. First, the cantilever deflection was measured interferometrically as opposed to using the deflection of a laser beam. Secondly, the substrate was heated to serve as the emitter instead of using a heated sphere. They attached 40 and 22 μm diameter SiO_2 spheres to SiN_x-Au bimaterial cantilevers and measured the total gap thermal conductance as the distance between the spheres and the planar sample was varied via piezoelectric control of the sample. Their results for the 40 μm sphere are shown in Fig. 19(b) and demonstrate near-field enhancements similar to the results by Shen *et al.*[218] Distinct from the previous work is the observation that their experimental data agree remarkably well with theoretical expectations based on the Derjaguin approximation. In performing this comparison, a data fitting process was used based on a model with the far-field thermal conductance, the cantilever sensitivity and a gap size shift (which indicates the uncertainty in gap size due to surface roughness) as the parameters. Specifically, the far-field conductance between the glass sphere and sample was estimated via the Stefan-Boltzmann law, with the emissivity of glass taken to be 0.354. The gap size shift was used to account for the large roughness of the spheres (inset of Fig. 19(b)) and was fitted to be ~32 nm, close to the SEM measured roughness of 40 nm for the 40 μm diameter sphere. For the 22 μm diameter sphere, the roughness was as large as 150 nm.

Successive papers from Chevrier's group[255,256] demonstrated tunability of NFRHT. In the first publication,[255] NFRHT between a 40 μm diameter sodalime glass sphere and a heated VO_2 substrate was investigated. In this study VO_2 was selected for its MIT transition at a critical temperature of ~340 K. In low temperature insulating phase VO_2 substrate supports SPhPs and is expected to enhance heat transfer to the SiO_2 sphere. Indeed, the experiment data confirmed the prediction for gap sizes smaller than 150 nm. Further experiments[256] by the same group investigated additional tuning mechanisms by measuring NFRHT between a SiO_2 sphere and SiC substrates with or without a graphene top layer. They observed an increase in NFRHT in the presence of graphene (Fig. 19(d)) and attributed the enhancement to thermally-excited SPPs on graphene. In both work the proper

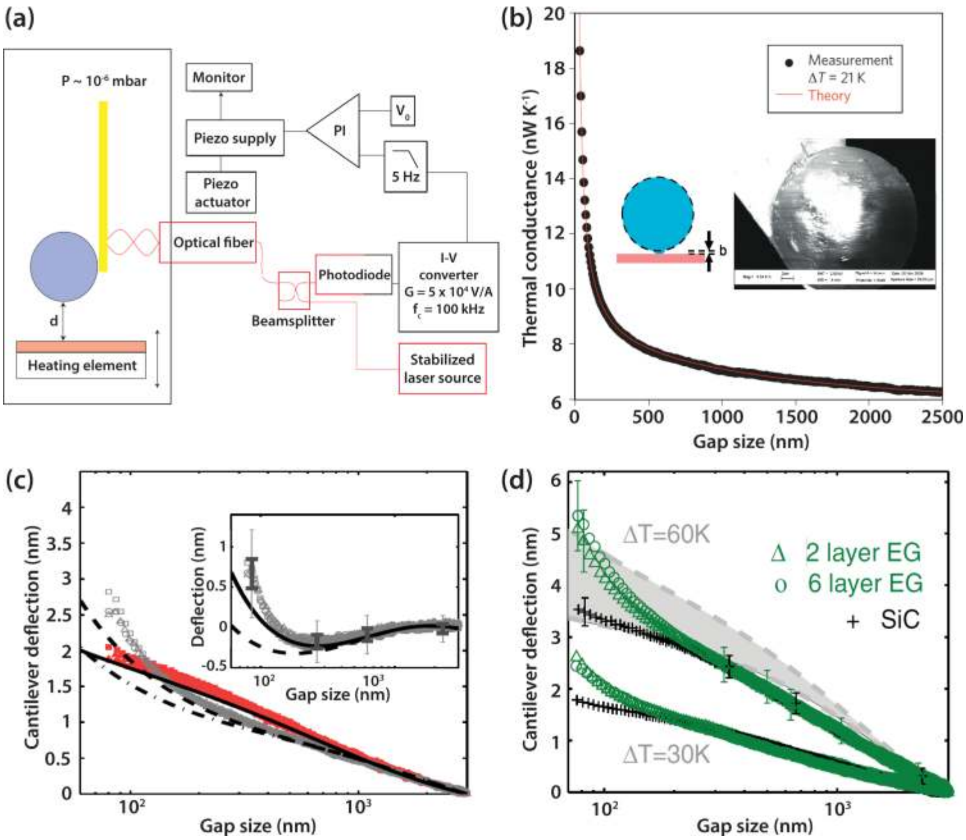

FIG. 19. Bimaterial cantilever-based measurements of sphere-plane NFRHT using interferometric detection of deflection. (a) Schematic of the setup.[217] The same principle was used in other works.[255,256] (b) Results[217] for vacuum gap thermal conductance versus gap size between a 40 μm diameter sodalime glass sphere and a borosilicate glass substrate. Experimental data (dots) compared to theory (red line). (c) Results[255] for measured cantilever deflection versus gap size for a 40 μm diameter sodalime glass sphere and a VO_2 substrate. Open gray (closed red) symbols correspond to experimental data for VO_2 in the insulating (metallic) phase, obtained as the difference between raw data for $\Delta T = 30$ K and $\Delta T = 0$ K ($\Delta T = 75$ K and $\Delta T = 50$ K). Calculations for the metallic (insulating) phases are plotted as a solid (dashed) black line. Inset: Shows the difference between the insulating and metallic phases. (d) Results[256] for measured beam deflection between a SiO_2 sphere and 2-layer or 6-layer graphene on SiC, and bare SiC. Theory is shown (gray area) for NFRHT between a SiO_2 sphere and a SiC substrate.

characterization and subtraction of the gap-dependent force effect from the total cantilever deflection is critical.

The bimaterial cantilever-based approach described above represents a major experimental breakthrough for NFRHT studies. However, it may suffer from two drawbacks: 1) The detection of contact between the sphere and the plane relies on the deflection of the cantilever which is also used to monitor temperature changes via its deflections, and 2) bending of the cantilever due to electrostatic forces between the sphere and planar surface could also result in deflections that can be convolved with the signal arising from temperature variations. Cahill *et al.*[25] recently identified these challenges and called for experimental solutions. Recent work by Song *et al.*[223] aimed to develop a novel experimental platform that can overcome some of these challenges and is described next.

2. Suspended resistance-based calorimeters

Song *et al.*[223] recently reported a platform for studying NFRHT in the sphere-plane configuration. Their experimental setup consists of two microfabricated devices, an emitter (Fig. 20(c)) and a receiver (Fig. 20(d)), which were placed in close proximity to each other in a vacuum environment (10^{-6} torr) as is shown schematically in Fig. 20(a). The emitter device consisted of a suspended Si

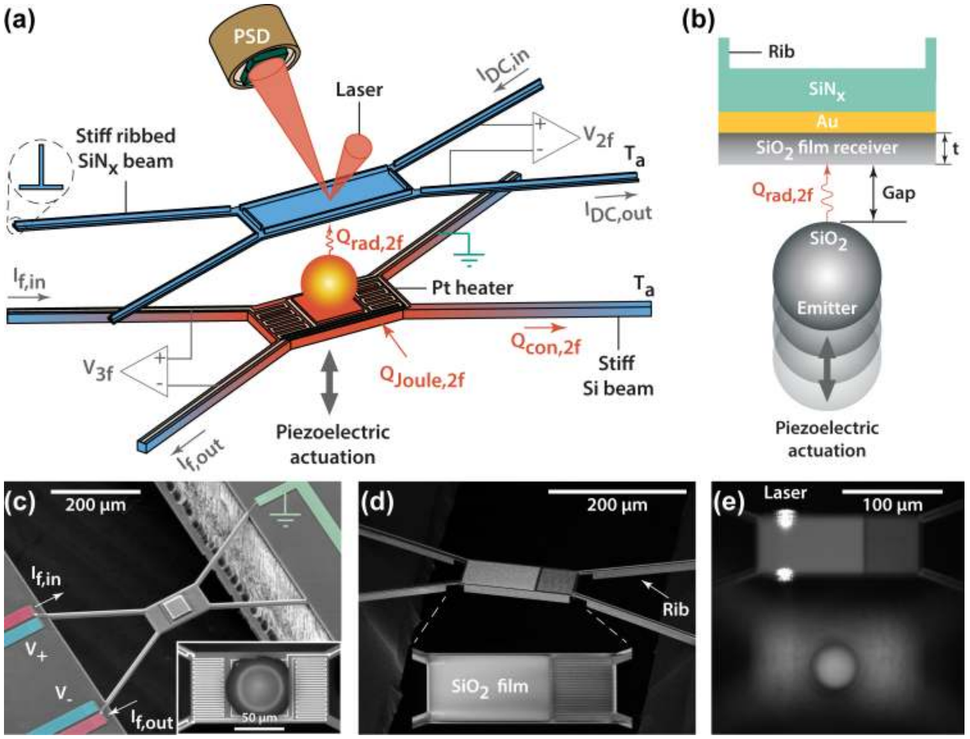

FIG. 20. Suspended resistance calorimeter-based sphere-plane approach: setup and devices[223] (a) Schematic of the setup. The emitter consists of a suspended Si platform, with an attached SiO_2 microsphere and an integrated electrical heater-thermometer. The receiver is a stiff SiN_x platform coated with Au and a SiO_2 film. A laser and a PSD enable emitter-receiver contact detection with nanometer resolution. (b) Schematic cross section of the planar receiver region and the spherical SiO_2 emitter. The Au layer is ~100 nm thick, the thickness t of the SiO_2 film varies from 50 nm to 3 μm for different receiver devices. (c) SEM image of the suspended platform. Inset: Optical image of the spherical emitter. (d) SEM images of the receiver. (e) An optical image of the emitter and receiver during alignment.

region onto which a 53 μm diameter SiO_2 sphere was attached. The suspended region was connected to the surrounding substrate via stiff beams (~500 N/m) with a thermal conductance of ~180 μW/K. The emitter also featured a platinum resistance heater-thermometer through which a sinusoidal electric current ($f = 1$ Hz) was supplied to modulate the temperature of the suspended region and the sphere at $2f$. The SiN_x receiver device was suspended via thin, long beams to achieve a thermal conductance of ~2 μW/K. Further, the beams and the suspended regions of all receivers incorporated ribs that led to very stiff devices (stiffness ~70 N/m) with extremely flat suspended regions. The receiver devices also featured an integrated platinum resistance thermometer[259,260] which could resolve small temperature changes (~50 μK, when modulated at 2 Hz), enabling detection of heat currents as small as ~100 pW. Finally, the experimental platform also included an optical detection scheme for monitoring the deflections of the receiver device (Fig. 20(a)). Using these devices Song *et al*. systematically studied NFRHT between a silica sphere and a group of SiO_2 films to understand the effect of film thickness on NFRHT.

In their study, they employed receiver devices that were coated with SiO_2 layers of varying thicknesses (50 nm – 3 μm) deposited on a 100 nm-thick gold film (Fig. 20(b)). The roughness and cleanliness of the spheres and films were examined using a range of microscopy techniques including AFM and SEM. In their experiments, the receiver device was initially placed ~10 μm from the spherical emitter. When the emitter temperature was modulated sinusoidally at 2 Hz and 10 K amplitude, the resultant radiative heat currents between the emitter and receiver could be quantified by measuring the temperature oscillations of the receiver using its integrated resistance thermometer. The gap dependence of NFRHT could be studied by displacing the emitter towards the receiver with a piezoelectric actuator under closed-loop feedback control.[261] Contact

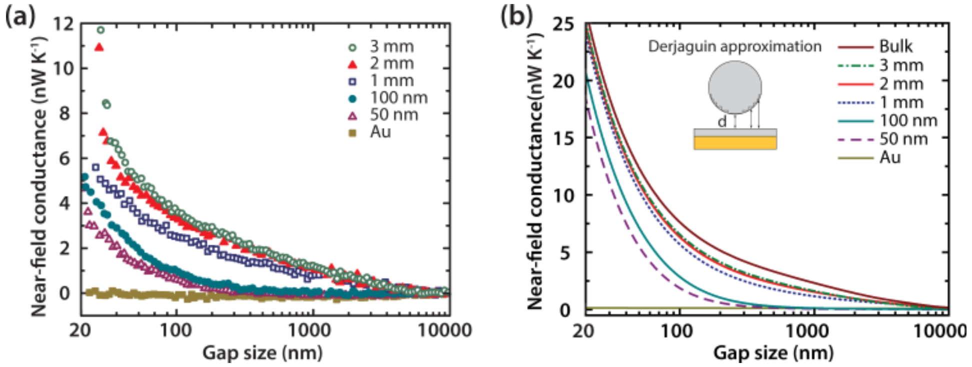

FIG. 21. Near-field thermal conductance as a function of gap size and film thickness.[223] (a) Measured near-field versus gap size between a SiO_2 sphere and different SiO_2 films of varying thicknesses deposited on Au. (b) Calculated near-field thermal conductance versus gap size for the sphere-plane system using the Derjaguin approximation.

between the emitter and receiver was detected via the optical deflection scheme used for monitoring the displacement of the receiver (Fig. 20(a), 20(e)). This is in strong contrast to the bimaterial-based NFRHT measurement technique described above because, in the technique described here, mechanical motion is detected optically whereas temperature changes are sensed using a resistance thermometer. Therefore, mechanical and thermal effects are effectively decoupled in the suspended resistance-based calorimeter scheme.

The measured near-field conductance obtained for films of various thicknesses is shown in Fig. 21(a). Intriguingly, the near-field conductance is found to increase only when the gap size approaches the film thickness. Control experiments for which the receiver had only a 100 nm-thick Au film and no SiO_2 coating (solid squares in Fig. 21(a)) showed that there was no measurable increase in conductance as the gap size was decreased. The gap and film-thickness dependence of the near-field conductance were explained by performing numerical simulations. Employing the formalism of fluctuational electrodynamics[15,16] within a scattering matrix approach,[200] they calculated the heat transfer coefficient between a semi-infinite SiO_2 surface and SiO_2 thin films coated on a semi-infinite Au surface. To establish a direct comparison with experimental results, they computed the near-field conductance between a 53 μm diameter silica sphere and thin film-coated surfaces (Fig. 21(b)) via the Derjaguin approximation. The computed conductances were found to be in good overall agreement with measurements, although the calculated conductances consistently overestimated their experimentally measured counterparts. The authors attributed the discrepancy between theory and experiment to uncertainties associated with the microstructure and optical properties of the integrated thin-films. Further, they also performed "exact" numerical studies using the fluctuating surface current formulation described in Sec. III B 3 to rule out the possibility that the disagreement between theory and experiment is due to the use of Derjaguin approximation.

To obtain insight into the film thickness dependence of the near field conductance, they calculated spectral heat transfer coefficients and concluded that TM modes dominate the radiative heat transfer at small gap sizes with major contributions from two narrow energy ranges centered around ∼60 meV and ∼140 meV. Further, by computing the transmission function at various frequencies they concluded that NFRHT enhancements are primarily due to cavity surface phonon polaritons (CSPhPs) supported in the gap between the SiO_2 layers. Finally, they related the observed film-thickness and gap size-dependent NFRHT properties to the shape of the cavity modes. This was accomplished by computing the normalized electric field intensity of representative CSPhP modes, corresponding to an energy of ∼61.2 meV for two coating thicknesses (100 nm and 3 μm) at a gap of 20 nm (Fig. 22(a)). The two mode shapes were almost identical due to small penetration depths, indicating that NFRHT in small gaps occurs through identical modes for both thin and thick films and is hence unaffected[116] by film thickness. On the contrary, they showed that when the gap becomes comparable to or larger than the film thickness, the intensity of these modes decays slowly in SiO_2, but drops sharply at the SiO_2-Au interface (lower panel Fig. 22(b)), reducing their ability to contribute to heat transport and

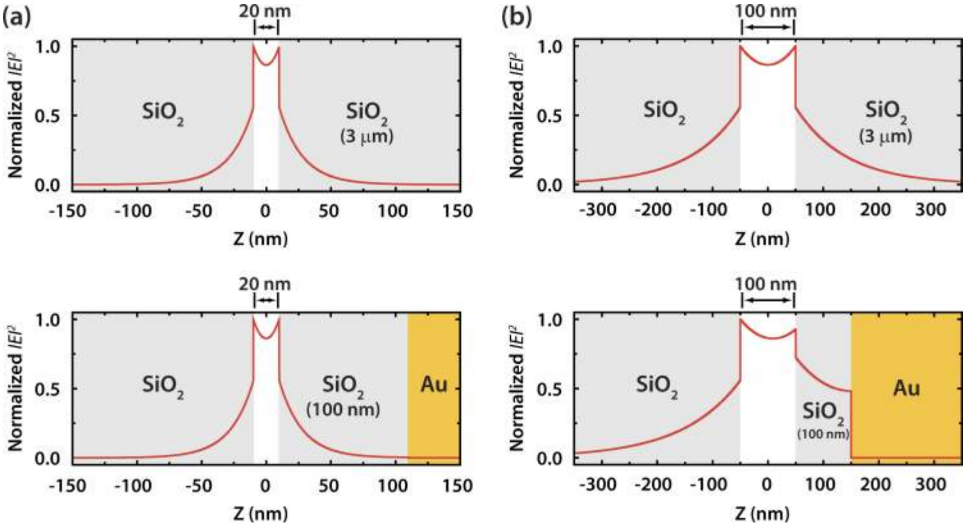

FIG. 22. Mode shape analysis.[223] (a) Normalized electric field intensity versus position for a representative cavity CSPhP mode ($\hbar\omega = 61.2$ meV) calculated for a gap of 20 nm and film thicknesses of $t = 3$ μm (upper) and $t = 100$ nm (lower), normalized to peak intensity. (b) Same as (a) except for a 100 nm gap. Grey regions correspond to SiO_2 and the yellow regions represent Au.

leading to a diminished transmission probability. Thus, they concluded that the NFRHT enhancement for thin films, at gaps larger than the film thickness, is significantly smaller than that of thicker films at the same gap size due to dramatic changes to the mode shapes at larger gaps.

V. CONCLUDING REMARKS

The past two decades have been marked by an enormous surge in the interest in nanoscale heat conduction (via phonons) which resulted in important insights now enabling the development of nanostructured thermoelectric materials as well as interfacial engineering for thermal management in electronic and photonic devices. Although nanoscale radiative heat transfer (NFRHT) offers a broad range of unique opportunities for both intricate control of heat flow and for the creation of novel energy conversion and information storage devices, research in NFRHT has received considerably less attention. In our opinion, this is primarily due to a lack of suitable experimental tools for systematically probing NFRHT. As described in this article this situation is now beginning to change primarily due to the emergence of a new suite of experimental tools that have enabled both the measurement of NFRHT at the nanoscale and the characterization of the electromagnetic states that lead to enhancement of near-field heat transfer. Further, recent years have also witnessed great improvements in the computational tools required to model NFRHT in arbitrary geometries and gap sizes. These advances have led to a variety of predictions of nanoscale radiative heat transfer that hold significant technological promise if systematically understood and leveraged for future applications in thermal management, instrumentation, and energy conversion.

One of the major impediments to experimental progress is the current inability to characterize NFRHT between planar surfaces at gaps as small as a few nanometers or even tens of nanometers in the parallel-plane configuration. If the experimental techniques to probe NFRHT between surfaces can be combined with precisely micro- and nanofabricated planar dielectric, metallic and heterostructured surfaces with nanometer control of gap size, the study of NFRHT could potentially be revolutionized. In fact, such breakthroughs combined with recent advancements in instrumentation and fabrication techniques provide a unique opportunity for realizing the much-desired goal of a detailed understanding of NFRHT. In addition to the above described need for breakthroughs in instrumentation, rapid progress in understanding NFRHT also critically hinges on successfully leveraging recent advances in computational techniques and novel materials. Specifically, it is absolutely critical to create both novel materials and surfaces that are appropriately nanostructured or integrated with suitably chosen 2D materials such as graphene to understand the efficacy of near-field effects for heat transfer, spectral control and energy conversion. If successful, this multi-disciplinary research area could significantly impact future technologies much as far-field radiation is now central to a range of technologies.

ACKNOWLEDGMENTS

P.R. and E.M. gratefully acknowledge support from the Army Research Office (W911NF-12-1-0612) and the National Science Foundation (CBET 1235691).

[1] E. S. Barr, American Journal of Physics **28**, 42–54 (1960).
[2] W. Herschel, Philosophical Transactions of Royal Society of London **90**, 284–292 (1800).
[3] W. Herschel, Philosophical Transactions of Royal Society of London **90**, 293–326 (1800).
[4] W. Herschel, Philosophical Transactions of Royal Society of London **90**, 437–538 (1800).
[5] M. Planck, Verhandlungen der Deutschen Physikalischen Gesellschaft **2**, 202–204 (1900).
[6] M. Planck, Verhandlungen der Deutschen Physikalischen Gesellschaft **2**, 237–245 (1900).
[7] M. Planck, *The theory of heat radiation*, 2nd ed. (P. Blakiston's Son & Co., Philadelphia, PA, 1914).
[8] D. ter Haar, *The old quantum theory*, 1st ed. (Pergamon Press, Oxford, New York, 1967).
[9] D. Bohm, *Quantum theory* (Dover Publications, New York, 1989).
[10] H. Kragh, Physics World **13**(12), 31–35 (2000).
[11] H. B. Callen and T. A. Welton, Physical Review **83**(1), 34–40 (1951).
[12] R. Kubo, Reports on Progress in Physics **29**, 255–284 (1966).
[13] L. D. Landau, E. M. Lifshitz, and L. P. Pitaevskii, *Statistical physics*, 3rd, rev. and enl. ed. (Pergamon Press, Oxford, 1980).
[14] W. Eckhardt, Physical Review A **29**(4), 1991–2003 (1984).
[15] S. M. Rytov, *Theory of electric fluctuations and thermal radiation* (Air Force Cambrige Research Center, Bedford, MA, 1953).
[16] S. M. Rytov, Y. A. Kravtsov, and V. I. Tatarskii, *Principles of statistical radiophysics* (Springer-Verlag, Berlin Heidelberg, 1989).
[17] A. G. Emslie, in *Aerodynamically Heated Structures*, edited by P. E. Glaser (Prentice-Hall, Englewood Cliffs, NJ, 1962).
[18] J. B. Pendry, Journal of Physics-Condensed Matter **11**(35), 6621–6633 (1999).
[19] Z. M. Zhang, *Nano/microscale heat transfer* (McGraw-Hill, New York, NY, 2007).
[20] K. Joulain, J. P. Mulet, F. Marquier, R. Carminati, and J. J. Greffet, Surface Science Reports **57**(3-4), 59–112 (2005).
[21] A. I. Volokitin and B. N. J. Persson, Reviews of Modern Physics **79**(4), 1291–1329 (2007).
[22] S. Basu, Z. M. Zhang, and C. J. Fu, International Journal of Energy Research **33**(13), 1203–1232 (2009).
[23] I. A. Dorofeyev and E. A. Vinogradov, Physics Reports-Review Section of Physics Letters **504**(2-4), 75–143 (2011).
[24] A. C. Jones, B. T. O'Callahan, H. U. Yang, and M. B. Raschke, Progress in Surface Science **88**(4), 349–392 (2013).
[25] D. G. Cahill, P. V. Braun, G. Chen, D. R. Clarke, S. H. Fan, K. E. Goodson, P. Keblinski, W. P. King, G. D. Mahan, A. Majumdar, H. J. Maris, S. R. Phillpot, E. Pop, and L. Shi, Applied Physics Reviews **1**(1) (2014).
[26] Y. M. Xuan, Photonics and Nanostructures-Fundamentals and Applications **12**(2), 93–113 (2014).
[27] A. I. Volokitin and B. N. J. Persson, Physics-Uspekhi **50**(9), 879–906 (2007).
[28] C. Girard, C. Joachim, and S. Gauthier, Reports on Progress in Physics **63**(6), 893–938 (2000).
[29] R. Carminati and J. J. Greffet, Physical Review Letters **82**(8), 1660–1663 (1999).
[30] J. J. Greffet, R. Carminati, K. Joulain, J. P. Mulet, S. P. Mainguy, and Y. Chen, Nature **416**(6876), 61–64 (2002).
[31] F. Marquier, K. Joulain, J. P. Mulet, R. Carminati, J. J. Greffet, and Y. Chen, Physical Review B **69**(15) (2004).
[32] M. Laroche, C. Arnold, F. Marquier, R. Carminati, J. J. Greffet, S. Collin, N. Bardou, and J. L. Pelouard, Optics Letters **30**(19), 2623–2625 (2005).
[33] M. Laroche, R. Carminati, and J. J. Greffet, Physical Review Letters **96**(12) (2006).
[34] J. J. Greffet and C. Henkel, Contemporary Physics **48**(4), 183–194 (2007).
[35] C. Henkel, K. Joulain, R. Carminati, and J. J. Greffet, Optics Communications **186**(1-3), 57–67 (2000).
[36] A. V. Shchegrov, K. Joulain, R. Carminati, and J. J. Greffet, Physical Review Letters **85**(7), 1548–1551 (2000).
[37] Y. De Wilde, F. Formanek, R. Carminati, B. Gralak, P. A. Lemoine, K. Joulain, J. P. Mulet, Y. Chen, and J. J. Greffet, Nature **444**(7120), 740–743 (2006).
[38] A. Kittel, U. F. Wischnath, J. Welker, O. Huth, F. Ruting, and S. A. Biehs, Applied Physics Letters **93**(19) (2008).
[39] U. F. Wischnath, J. Welker, M. Munzel, and A. Kittel, Review of Scientific Instruments **79**(7) (2008).
[40] M. H. Kryder, E. C. Gage, T. W. Mcdaniel, W. A. Challener, R. E. Rottmayer, G. P. Ju, Y. T. Hsia, and M. F. Erden, Proceedings of the IEEE **96**(11), 1810–1835 (2008).
[41] W. A. Challener, C. B. Peng, A. V. Itagi, D. Karns, W. Peng, Y. Y. Peng, X. M. Yang, X. B. Zhu, N. J. Gokemeijer, Y. T. Hsia, G. Ju, R. E. Rottmayer, M. A. Seigler, and E. C. Gage, Nature Photonics **3**(4), 220–224 (2009).
[42] B. C. Stipe, T. C. Strand, C. C. Poon, H. Balamane, T. D. Boone, J. A. Katine, J. L. Li, V. Rawat, H. Nemoto, A. Hirotsune, O. Hellwig, R. Ruiz, E. Dobisz, D. S. Kercher, N. Robertson, T. R. Albrecht, and B. D. Terris, Nature Photonics **4**(7), 484–488 (2010).
[43] P. J. van Zwol, K. Joulain, P. Ben-Abdallah, and J. Chevrier, Physical Review B **84**(16) (2011).
[44] P. J. van Zwol, K. Joulain, P. Ben-Abdallah, J. J. Greffet, and J. Chevrier, Physical Review B **83**(20) (2011).
[45] V. B. Svetovoy, P. J. van Zwol, and J. Chevrier, Physical Review B **85**(15) (2012).
[46] L. J. Cui, Y. Huang, J. Wang, and K. Y. Zhu, Applied Physics Letters **102**(5) (2013).

[47] S. Vassant, I. M. Doyen, F. Marquier, F. Pardo, U. Gennser, A. Cavanna, J. L. Pelouard, and J. J. Greffet, Applied Physics Letters **102**(8) (2013).
[48] Y. Huang, S. V. Boriskina, and G. Chen, Applied Physics Letters **105**(24) (2014).
[49] R. Incardone, T. Emig, and M. Kruger, Europhysics Letter **106**(4) (2014).
[50] T. Inoue, M. De Zoysa, T. Asano, and S. Noda, Nature Materials **13**(10), 928–931 (2014).
[51] M. Nikbakht, Journal of Applied Physics **116**(9) (2014).
[52] C. R. Otey, W. T. Lau, and S. H. Fan, Physical Review Letters **104**(15), 154301 (2010).
[53] S. Basu and M. Francoeur, Applied Physics Letters **98**(11) (2011).
[54] H. Iizuka and S. H. Fan, Journal of Applied Physics **112**(2) (2012).
[55] P. Ben-Abdallah and S. A. Biehs, Applied Physics Letters **103**(19) (2013).
[56] J. G. Huang, Q. Li, Z. H. Zheng, and Y. M. Xuan, International Journal of Heat and Mass Transfer **67**, 575–580 (2013).
[57] L. P. Wang and Z. M. Zhang, Nanoscale and Microscale Thermophysical Engineering **17**(4), 337–348 (2013).
[58] L. X. Zhu, C. R. Otey, and S. H. Fan, Physical Review B **88**(18) (2013).
[59] Z. Chen, C. Wong, S. Lubner, S. Yee, J. Miller, W. Jang, C. Hardin, A. Fong, J. E. Garay, and C. Dames, Nature Communications **5** (2014).
[60] H. Iizuka and S. H. Fan, Journal of Quantitative Spectroscopy & Radiative Transfer **148**, 156–164 (2014).
[61] E. Nefzaoui, J. Drevillon, Y. Ezzahri, and K. Joulain, Applied Optics **53**(16), 3479–3485 (2014).
[62] R. Messina, M. Antezza, and P. Ben-Abdallah, Physical Review Letters **109**(24) (2012).
[63] P. Ben-Abdallah and S. A. Biehs, Physical Review Letters **112**(4), 044301 (2014).
[64] M. Elzouka and S. Ndao, Applied Physics Letters **105**(24) (2014).
[65] V. Kubytskyi, S. A. Biehs, and P. Ben-Abdallah, Physical Review Letters **113**(7) (2014).
[66] R. S. DiMatteo, P. Greiff, S. L. Finberg, K. A. Young-Waithe, H. K. H. Choy, M. M. Masaki, and C. G. Fonstad, Applied Physics Letters **79**(12), 1894–1896 (2001).
[67] A. Narayanaswamy and G. Chen, Applied Physics Letters **82**(20), 3544–3546 (2003).
[68] M. Laroche, R. Carminati, and J. J. Greffet, Journal of Applied Physics **100**(6) (2006).
[69] K. Park, S. Basu, W. P. King, and Z. M. Zhang, Journal of Quantitative Spectroscopy & Radiative Transfer **109**(2), 305–316 (2008).
[70] U. Dillner, Journal of Electronic Materials **39**(9), 1645–1649 (2010).
[71] M. Francoeur, R. Vaillon, and M. P. Mengüç, IEE Transactions on Energy Conversion **26**(2), 686–698 (2011).
[72] R. Messina and P. Ben-Abdallah, Scientific Reports **3** (2013).
[73] B. Zhao, L. P. Wang, Y. Shuai, and Z. M. Zhang, International Journal of Heat and Mass Transfer **67**, 637–645 (2013).
[74] Y. Guo, S. Molesky, H. Hu, C. L. Cortes, and Z. Jacob, Applied Physics Letters **105**(7) (2014).
[75] A. Lenert, D. M. Bierman, Y. Nam, W. R. Chan, I. Celanovic, M. Soljacic, and E. N. Wang, Nature Nanotechnology **9**(2), 126–130 (2014).
[76] V. B. Svetovoy and G. Palasantzas, Physical Review Applied **2**(3) (2014).
[77] M. D. Whale and E. G. Cravalho, IEEE Transactions on Energy Conversion **17**(1), 130–142 (2002).
[78] S. Basu, Y. B. Chen, and Z. M. Zhang, International Journal of Energy Research **31**(6-7), 689–716 (2007).
[79] R. G. Yang, A. Narayanaswamy, and G. Chen, Journal of Computational and Theoretical Nanoscience **2**(1), 75–87 (2005).
[80] J. Fang, H. Frederich, and L. Pilon, Journal of Heat Transfer-Transactions of the ASME **132**(9) (2010).
[81] J. W. Schwede, I. Bargatin, D. C. Riley, B. E. Hardin, S. J. Rosenthal, Y. Sun, F. Schmitt, P. Pianetta, R. T. Howe, Z. X. Shen, and N. A. Melosh, Nature Materials **9**(9), 762–767 (2010).
[82] J. H. Lee, I. Bargatin, N. A. Melosh, and R. T. Howe, Applied Physics Letters **100**(17) (2012).
[83] M. F. Modest, *Radiative heat transfer*, 3rd ed. (Academic Press, Oxford, UK, 2013).
[84] R. Siegel and J. R. Howell, *Thermal radiation heat transfer*, 4th ed. (Taylor & Francis, New York, 2002).
[85] D. Bijl, Philosophical Magazine **43**(347), 1342–1344 (1952).
[86] D. Dalvit, P. Milonni, D. Roberts, and F. da Rosa, *Casimir Physics* (Springer-Verlag, Berlin, Heidelberg, 2011).
[87] E. G. Cravalho, C. L. Tien, and R. P. Caren, Journal of Heat Transfer **89**(4), 351–358 (1967).
[88] A. Olivei, Revue de Physique Appliquee **3**(3), 225–230 (1968).
[89] R. F. Boehm and C. L. Tien, Mechanical Engineering **92**(4), 405–411 (1970).
[90] D. Polder and M. A. van Hove, Physical Review B **4**(10), 3303–3314 (1971).
[91] R. P. Caren, Journal of Heat Transfer **94**(3), 289–294 (1972).
[92] R. P. Caren, Journal of Heat Transfer **94**(3), 295–299 (1972).
[93] R. P. Caren, International Journal of Heat and Mass Transfer **17**(7), 755–765 (1974).
[94] M. L. Levin, V. G. Polevoi, and S. M. Rytov, Soviet Physics, JETP **52**(6), 1054–1063 (1980).
[95] J. J. Loomis and H. J. Maris, Physical Review B **50**(24), 18517–18524 (1994).
[96] E. G. Cravalho, G. A. Domoto, and C. L. Tien, in *AIAA 3rd Thermophysics Conference* (Los Angeles, CA, 1968).
[97] C. M. Hargreaves, Physics Letters A **30**(9), 491–492 (1969).
[98] G. A. Domoto, R. F. Boehm, and C. L. Tien, Journal of Heat Transfer **92**(3), 412–416 (1970).
[99] C. M. Hargreaves, Philips Research Reports **5**, 1–80 (1973).
[100] S. S. Kutateladze, N. A. Rubtsov, and Y. A. Baltsevich, Soviet Physics Doklady **23**(8), 577–578 (1978).
[101] Y. A. Baltsevich and N. A. Rubtsov, Heat Transfer-Soviet Research **12**, 117–133 (1980).
[102] R. Messina and M. Antezza, Physical Review A **84**(4) (2011).
[103] M. Kruger, G. Bimonte, T. Emig, and M. Kardar, Physical Review B **86**(11) (2012).
[104] A. W. Rodriguez, M. T. H. Reid, and S. G. Johnson, Physical Review B **88**(5) (2013).
[105] A. Narayanaswamy and Y. Zheng, Journal of Quantitative Spectroscopy & Radiative Transfer **132**, 12–21 (2014).
[106] C. R. Otey, L. X. Zhu, S. Sandhu, and S. H. Fan, Journal of Quantitative Spectroscopy & Radiative Transfer **132**, 3–11 (2014).
[107] B. V. Budaev and D. B. Bogy, Zeitschrift Fur Angewandte Mathematik Und Physik **62**(6), 1143–1158 (2011).

[108] B. V. Budaev and D. B. Bogy, Applied Physics a-Materials Science & Processing **103**(4), 971–975 (2011).
[109] B. V. Budaev and D. B. Bogy, Applied Physics Letters **104**(6) (2014).
[110] J. D. Jackson, *Classical electrodynamics*, 3rd ed. (Wiley, New York, 1999).
[111] J. A. Kong, *Electromagnetic wave theory* (EMW Publishing, Cambridge, MA, 2008).
[112] K. Joulain, J. Drevillon, and P. Ben-Abdallah, Physical Review B **81**(16) (2010).
[113] Z. H. Zheng and Y. M. Xuan, International Journal of Heat and Mass Transfer **54**(5-6), 1101–1110 (2011).
[114] C. T. Tai, *Dyadic green functions in electromagnetic theory*, 2nd ed. (IEEE Press, Piscataway, NJ, 1994).
[115] J. E. Sipe, Journal of the Optical Society of America B-Optical Physics **4**(4), 481–489 (1987).
[116] S. A. Biehs, E. Rousseau, and J. J. Greffet, Physical Review Letters **105**(23) (2010).
[117] P. Ben-Abdallah, K. Joulain, and A. Pryamikov, Applied Physics Letters **96**(14) (2010).
[118] A. Narayanaswamy and G. Chen, Physical Review B **70**(12) (2004).
[119] A. Narayanaswamy and G. Chen, Journal of Quantitative Spectroscopy & Radiative Transfer **93**(1-3), 175–183 (2005).
[120] A. Pryamikov, K. Joulain, P. Ben-Abdallah, and J. Drevillon, Journal of Quantitative Spectroscopy & Radiative Transfer **112**(8), 1314–1322 (2011).
[121] S. A. Biehs, P. Ben-Abdallah, F. da Rosa, K. Joulain, and J. J. Greffet, Optics Express **19**(19), A1088–A1103 (2011).
[122] I. S. Nefedov and C. R. Simovski, Physical Review B **84**(19) (2011).
[123] Y. Bai, Y. Y. Jiang, and L. H. Liu, Journal of Physics D-Applied Physics **47**(44) (2014).
[124] X. L. Liu, R. Z. Zhang, and Z. M. Zhang, International Journal of Heat and Mass Transfer **73**, 389–398 (2014).
[125] L. J. Cui, Y. Huang, and J. Wang, Journal of Applied Physics **112**(8) (2012).
[126] M. Francoeur, S. Basu, and S. J. Petersen, Optics Express **19**(20), 18774–18788 (2011).
[127] A. I. Volokitin and B. N. J. Persson, Physical Review B **63**(20) (2001).
[128] M. Francoeur and M. P. Menguc, Journal of Quantitative Spectroscopy & Radiative Transfer **109**(2), 280–293 (2008).
[129] S. Basu and L. P. Wang, Applied Physics Letters **102**(5) (2013).
[130] S. A. Dyakov, J. Dai, M. Yan, and M. Qiu, Physical Review B **90**(4) (2014).
[131] A. I. Volokitin and B. N. J. Persson, Physical Review B **83**(24) (2011).
[132] O. Ilic, M. Jablan, J. D. Joannopoulos, I. Celanovic, H. Buljan, and M. Soljacic, Physical Review B **85**(15) (2012).
[133] M. Lim, S. S. Lee, and B. J. Lee, Optics Express **21**(19), 22173–22185 (2013).
[134] D. Drosdoff, A. D. Phan, and L. M. Woods, Advanced Optical Materials **2**(11), 1038–1042 (2014).
[135] S. A. Biehs, F. S. S. Rosa, and P. Ben-Abdallah, Applied Physics Letters **98**(24) (2011).
[136] S. A. Biehs, M. Tschikin, and P. Ben-Abdallah, Physical Review Letters **109**(10) (2012).
[137] Y. Guo, C. L. Cortes, S. Molesky, and Z. Jacob, Applied Physics Letters **101**(13) (2012).
[138] S. A. Biehs, M. Tschikin, R. Messina, and P. Ben-Abdallah, Applied Physics Letters **102**(13) (2013).
[139] Y. Guo and Z. B. Jacob, Optics Express **21**(12), 15014–15019 (2013).
[140] X. L. Liu, R. Z. Zhang, and Z. M. Zhang, Applied Physics Letters **103**(21) (2013).
[141] Y. Guo and Z. Jacob, Journal of Applied Physics **115**(23) (2014).
[142] O. D. Miller, S. G. Johnson, and A. W. Rodriguez, Physical Review Letters **112**(15) (2014).
[143] I. S. Nefedov and L. A. Melnikov, Applied Physics Letters **105**(16) (2014).
[144] S. Basu and Z. M. Zhang, Journal of Applied Physics **105**(9) (2009).
[145] X. J. Wang, S. Basu, and Z. M. Zhang, Journal of Physics D-Applied Physics **42**(24) (2009).
[146] P. Ben-Abdallah and K. Joulain, Physical Review B **82**(12) (2010).
[147] S. Basu and M. Francoeur, Applied Physics Letters **98**(24) (2011).
[148] Y. Zhao, G. H. Tang, and Z. Y. Li, International Communications in Heat and Mass Transfer **39**(7), 918–922 (2012).
[149] E. Nefzaoui, Y. Ezzahri, J. Drevillon, and K. Joulain, Eur. Phys. J. Appl. Phys. **63**, 30902 (2013).
[150] C. Simovski, S. Maslovski, I. Nefedov, and S. Tretyakov, Optics Express **21**(12), 14988–15013 (2013).
[151] M. Francoeur, M. P. Menguc, and R. Vaillon, Journal of Quantitative Spectroscopy & Radiative Transfer **110**(18), 2002–2018 (2009).
[152] M. Francoeur, M. P. Mengüç, and R. Vaillon, Physical Review B **84**(7) (2011).
[153] Z. H. Zheng and Y. M. Xuan, Chinese Science Bulletin **56**(22), 2312–2319 (2011).
[154] J. P. Mulet, K. Joulain, R. Carminati, and J. J. Greffet, Microscale Thermophysical Engineering **6**(3), 209–222 (2002).
[155] S. A. Biehs and J. J. Greffet, Physical Review B **82**(24) (2010).
[156] C. J. Fu and Z. M. Zhang, International Journal of Heat and Mass Transfer **49**(9-10), 1703–1718 (2006).
[157] E. Rousseau, M. Laroche, and J. J. Greffet, Applied Physics Letters **95**(23) (2009).
[158] E. Rousseau, M. Laroche, and J. J. Greffet, Journal of Quantitative Spectroscopy & Radiative Transfer **111**(7-8), 1005–1014 (2010).
[159] B. A. Liu, J. W. Shi, K. Liew, and S. Shen, Optics Communications **314**, 57–65 (2014).
[160] P. O. Chapuis, S. Volz, C. Henkel, K. Joulain, and J. J. Greffet, Physical Review B **77**(3), 9 (2008).
[161] Y. Zheng and A. Narayanaswamy, Physical Review A **89**(2) (2014).
[162] S. A. Biehs, European Physical Journal B **58**(4), 423–431 (2007).
[163] S. A. Biehs, D. Reddig, and M. Holthaus, European Physical Journal B **55**(3), 237–251 (2007).
[164] M. Francoeur, M. P. Menguc, and R. Vaillon, Applied Physics Letters **93**(8), 089901 (2008).
[165] P. Ben-Abdallah, K. Joulain, J. Drevillon, and G. Domingues, Journal of Applied Physics **106**(4) (2009).
[166] C. J. Fu and W. C. Tan, Journal of Quantitative Spectroscopy & Radiative Transfer **110**(12), 1027–1036 (2009).
[167] M. Francoeur, M. P. Menguc, and R. Vaillon, Journal of Physics D-Applied Physics **43**(7) (2010).
[168] M. Francoeur, M. P. Menguc, and R. Vaillon, Applied Physics a-Materials Science & Processing **103**(3), 547–550 (2011).
[169] L. P. Wang, S. Basu, and Z. M. Zhang, Journal of Heat Transfer-Transactions of the ASME **133**(7) (2011).
[170] L. Y. Carrillo and Y. Bayazitoglu, Journal of Quantitative Spectroscopy & Radiative Transfer **112**(3), 412–419 (2011).
[171] L. Y. Carrillo and Y. Bayazitoglu, Nanoscale and Microscale Thermophysical Engineering **15**(3), 195–208 (2011).
[172] J. P. Mulet, K. Joulain, R. Carminati, and J. J. Greffet, Applied Physics Letters **78**(19), 2931–2933 (2001).

[173] P. O. Chapuis, J. J. Greffet, K. Joulain, and S. Volz, Nanotechnology **17**(12), 2978–2981 (2006).
[174] S. A. Biehs, O. Huth, and F. Ruting, Physical Review B **78**(8) (2008).
[175] P. O. Chapuis, M. Laroche, S. Volz, and J. J. Greffet, Physical Review B **77**(12) (2008).
[176] S. A. Biehs and J. J. Greffet, Physical Review B **81**(24) (2010).
[177] A. Narayanaswamy and G. Chen, Physical Review B **77**(7) (2008).
[178] L. Y. Carrillo and Y. Bayazitoglu, Journal of Thermophysics and Heat Transfer **24**(2), 309–315 (2010).
[179] K. Sasihithlu and A. Narayanaswamy, Optics Express **19**(14), A772–A785 (2011).
[180] K. Sasihithlu and A. Narayanaswamy, Physical Review B **83**(16) (2011).
[181] Z. M. Zhang and B. J. Lee, Optics Express **14**(21), 9963–9970 (2006).
[182] B. J. Lee, K. Park, and Z. M. Zhang, Applied Physics Letters **91**(15) (2007).
[183] S. Basu, L. P. Wang, and Z. M. Zhang, Journal of Quantitative Spectroscopy & Radiative Transfer **112**(7), 1149–1155 (2011).
[184] S. Basu and Z. M. Zhang, Applied Physics Letters **95**(13), 133104 (2009).
[185] S. Basu and M. Francoeur, Applied Physics Letters **99**(14) (2011).
[186] S. Lang, M. Tschikin, S. A. Biehs, A. Y. Petrov, and M. Eich, Applied Physics Letters **104**(12) (2014).
[187] K. Joulain, R. Carminati, J. P. Mulet, and J. J. Greffet, Physical Review B **68**(24) (2003).
[188] P. Ben-Abdallah, K. Joulain, J. Drevillon, and G. Domingues, Applied Physics Letters **94**(15) (2009).
[189] M. Francoeur, M. P. Menguc, and R. Vaillon, Journal of Applied Physics **107**(3) (2010).
[190] A. Narayanaswamy and G. Chen, Journal of Quantitative Spectroscopy & Radiative Transfer **111**(12-13), 1877–1884 (2010).
[191] F. Ruting, S. A. Biehs, O. Huth, and M. Holthaus, Physical Review B **82**(11) (2010).
[192] Z. M. Zhang and S. Basu, International Journal of Heat and Mass Transfer **50**(3-4), 702–712 (2007).
[193] I. Dorofeyev, Physica Scripta **84**(5) (2011).
[194] A. Narayanaswamy and Y. Zheng, Physical Review B **88**(7) (2013).
[195] I. Latella, A. Perez-Madrid, L. C. Lapas, and J. M. Rubi, Journal of Applied Physics **115**(12) (2014).
[196] B. V. Derjaguin, I. I. Abrikosova, and E. M. Lifshitz, Q. Rev. Chem. Soc. **10**(3), 295–329 (1956).
[197] C. Otey and S. H. Fan, Physical Review B **84**(24) (2011).
[198] B. Zhao and Z. M. Zhang, Journal of Quantitative Spectroscopy & Radiative Transfer **135**, 81–89 (2014).
[199] S. G. Johnson, in *Casimir Physics*, edited by D. Dalvit, P. Milonni, D. Roberts, and F. da Rosa (Springer-Verlag, Berlin Heidelberg, 2011).
[200] D. M. Whittaker and I. S. Culshaw, Physical Review B **60**(4), 2610–2618 (1999).
[201] G. Bimonte, Physical Review A **80**(4) (2009).
[202] S. J. Rahi, T. Emig, N. Graham, R. L. Jaffe, and M. Kardar, Physical Review D **80**(8) (2009).
[203] M. Kruger, T. Emig, and M. Kardar, Physical Review Letters **106**(21) (2011).
[204] R. Messina and M. Antezza, Epl **95**(6) (2011).
[205] A. P. McCauley, M. T. H. Reid, M. Kruger, and S. G. Johnson, Physical Review B **85**(16) (2012).
[206] R. Guerout, J. Lussange, F. S. S. Rosa, J. P. Hugonin, D. A. R. Dalvit, J. J. Greffet, A. Lambrecht, and S. Reynaud, Physical Review B **85**(18) (2012).
[207] J. Lussange, R. Guerout, F. S. S. Rosa, J. J. Greffet, A. Lambrecht, and S. Reynaud, Physical Review B **86**(8) (2012).
[208] A. W. Rodriguez, M. T. H. Reid, and S. G. Johnson, Physical Review B **86**(22) (2012).
[209] A. W. Rodriguez, M. T. H. Reid, J. Varela, J. D. Joannopoulos, F. Capasso, and S. G. Johnson, Physical Review Letters **110**(1), 014301 (2013).
[210] C. Luo, A. Narayanaswamy, G. Chen, and J. D. Joannopoulos, Physical Review Letters **93**(21) (2004).
[211] A. W. Rodriguez, O. Ilic, P. Bermel, I. Celanovic, J. D. Joannopoulos, M. Soljacic, and S. G. Johnson, Physical Review Letters **107**(11), 114302 (2011).
[212] A. Datas, D. Hirashima, and K. Hanamura, Journal of Thermal Science and Technology **8**(1), 91–105 (2013).
[213] A. Didari and M. P. Menguc, Journal of Quantitative Spectroscopy & Radiative Transfer **146**, 214–226 (2014).
[214] S. B. Wen, Journal of Heat Transfer-Transactions of the ASME **132**(7) (2010).
[215] B. A. Liu and S. Shen, Physical Review B **87**(11) (2013).
[216] S. Edalatpour and M. Francoeur, Journal of Quantitative Spectroscopy & Radiative Transfer **133**, 364–373 (2014).
[217] E. Rousseau, A. Siria, G. Jourdan, S. Volz, F. Comin, J. Chevrier, and J. J. Greffet, Nature Photonics **3**(9), 514–517 (2009).
[218] S. Shen, A. Narayanaswamy, and G. Chen, Nano Letters **9**(8), 2909–2913 (2009).
[219] R. F. Harrington, Journal of Electromagnetic Waves and Applications **3**(1), 1–15 (1989).
[220] S. R. Rengarajan and Y. Rahmat-Samii, IEEE Antennas and Propagation Magazine **42**(4), 122–128 (2000).
[221] S. M. Rao, D. R. Wilton, and A. W. Glisson, IEEE Transactions on Antennas and Propagation **30**(3), 409–418 (1982).
[222] M. T. Homer Reid, http://homerreid.dyndns.org/scuff-EM/.
[223] B. Song, Y. Ganjeh, S. Sadat, D. Thompson, A. Fiorino, V. Fernández-Hurtado, J. Feist, F. J. Garcia-Vidal, J. C. Cuevas, P. Reddy, and E. Meyhofer, Nature Nanotechnology **10**(3), 253–258 (2015).
[224] A. Taflove and S. C. Hagness, *Computational electrodynamics : the finite-difference time-domain method*, 3rd ed. (Artech House, Boston, 2005).
[225] T. Y. Hou, W. Luo, B. Rozovskii, and H. M. Zhou, Journal of Computational Physics **216**(2), 687–706 (2006).
[226] B. T. Draine and P. J. Flatau, Journal of the Optical Society of America a-Optics Image Science and Vision **11**(4), 1491–1499 (1994).
[227] N. A. Roberts and D. G. Walker, International Journal of Thermal Sciences **50**(5), 648–662 (2011).
[228] N. B. Li, J. Ren, L. Wang, G. Zhang, P. Hanggi, and B. W. Li, Reviews of Modern Physics **84**(3), 1045–1066 (2012).
[229] C. W. Chang, D. Okawa, A. Majumdar, and A. Zettl, Science **314**(5802), 1121–1124 (2006).
[230] M. M. Qazilbash, M. Brehm, B. G. Chae, P. C. Ho, G. O. Andreev, B. J. Kim, S. J. Yun, A. V. Balatsky, M. B. Maple, F. Keilmann, H. T. Kim, and D. N. Basov, Science **318**(5857), 1750–1753 (2007).

[231] L. X. Zhu, C. R. Otey, and S. H. Fan, Applied Physics Letters **100**(4) (2012).

[232] R. S. Ottens, V. Quetschke, S. Wise, A. A. Alemi, R. Lundock, G. Mueller, D. H. Reitze, D. B. Tanner, and B. F. Whiting, Physical Review Letters **107**(1) (2011).

[233] L. Hu, A. Narayanaswamy, X. Y. Chen, and G. Chen, Applied Physics Letters **92**(13) (2008).

[234] T. Kralik, P. Hanzelka, V. Musilova, A. Srnka, and M. Zobac, Review of Scientific Instruments **82**(5) (2011).

[235] T. Kralik, P. Hanzelka, M. Zobac, V. Musilova, T. Fort, and M. Horak, Physical Review Letters **109**(22) (2012).

[236] C. Feng, Z. A. Tang, and J. Yu, Chinese Physics Letters **29**(3) (2012).

[237] C. Feng, Z. A. Tang, J. Yu, and C. Y. Sun, Sensors **13**(2), 1998–2010 (2013).

[238] R. St-Gelais, B. Guha, L. X. Zhu, S. H. Fan, and M. Lipson, Nano Letters **14**(12), 6971–6975 (2014).

[239] C. C. Williams and H. K. Wickramasinghe, Applied Physics Letters **49**(23), 1587–1589 (1986).

[240] K. Dransfeld and J. B. Xu, Journal of Microscopy-Oxford **152**, 35–42 (1988).

[241] J. B. Xu, K. Lauger, K. Dransfeld, and I. H. Wilson, Review of Scientific Instruments **65**(7), 2262–2266 (1994).

[242] J. B. Xu, K. Lauger, R. Moller, K. Dransfeld, and I. H. Wilson, Journal of Applied Physics **76**(11), 7209–7216 (1994).

[243] W. Muller-Hirsch, A. Kraft, M. T. Hirsch, J. Parisi, and A. Kittel, Journal of Vacuum Science & Technology a-Vacuum Surfaces and Films **17**(4), 1205–1210 (1999).

[244] A. Kittel, W. Muller-Hirsch, J. Parisi, S. A. Biehs, D. Reddig, and M. Holthaus, Physical Review Letters **95**(22), 224301 (2005).

[245] L. Worbes, D. Hellmann, and A. Kittel, Physical Review Letters **110**(13) (2013).

[246] B. Guha, C. Otey, C. B. Poitras, S. H. Fan, and M. Lipson, Nano Letters **12**(9), 4546–4550 (2012).

[247] A. Babuty, K. Joulain, P. O. Chapuis, J. J. Greffet, and Y. De Wilde, Physical Review Letters **110**(14) (2013).

[248] A. C. Jones and M. B. Raschke, Nano Letters **12**(3), 1475–1481 (2012).

[249] B. T. O'Callahan, W. E. Lewis, A. C. Jones, and M. B. Raschke, Physical Review B **89**(24) (2014).

[250] K. Joulain, P. Ben-Abdallah, P. O. Chapuis, Y. De Wilde, A. Babuty, and C. Henkel, Journal of Quantitative Spectroscopy & Radiative Transfer **136**, 1–15 (2014).

[251] F. Peragut, J. B. Brubach, P. Roy, and Y. De Wilde, Applied Physics Letters **104**(25) (2014).

[252] L. M. Zhang, G. O. Andreev, Z. Fei, A. S. McLeod, G. Dominguez, M. Thiemens, A. H. Castro-Neto, D. N. Basov, and M. M. Fogler, Physical Review B **85**(7) (2012).

[253] A. Narayanaswamy, S. Shen, and G. Chen, Physical Review B **78**(11), 115303 (2008).

[254] S. Shen, A. Mavrokefalos, P. Sambegoro, and G. Chen, Applied Physics Letters **100**(23) (2012).

[255] P. J. van Zwol, L. Ranno, and J. Chevrier, Physical Review Letters **108**(23), 234301 (2012).

[256] P. J. van Zwol, S. Thiele, C. Berger, W. A. de Heer, and J. Chevrier, Physical Review Letters **109**(26) (2012).

[257] J. W. Shi, P. F. Li, B. A. Liu, and S. Shen, Applied Physics Letters **102**(18) (2013).

[258] M. Francoeur, Nature Nanotechnology **10**(3), 206–208 (2015).

[259] S. Sadat, E. Meyhofer, and P. Reddy, Review of Scientific Instruments **83**(8), 084902 (2012).

[260] S. Sadat, E. Meyhofer, and P. Reddy, Applied Physics Letters **102**(16), 163110 (2013).

[261] Y. Ganjeh, B. Song, K. Pagadala, K. Kim, S. Sadat, W. Jeong, K. Kurabayashi, E. Meyhofer, and P. Reddy, Review of Scientific Instruments **83**(10), 105101 (2012).